Quantifying brain microstructure with diffusion MRI: Theory and parameter estimation

Dmitry S. Novikov,[1,*] Sune N. Jespersen,[2,†] Valerij G. Kiselev,[3,‡] and Els Fieremans[1,§]

[1] *Center for Biomedical Imaging, Department of Radiology, NYU School of Medicine, New York, NY, USA*
[2] *CFIN/MINDLab, Department of Clinical Medicine and Department of Physics and Astronomy, Aarhus University, Aarhus, Denmark*
[3] *Department of Diagnostic Radiology, Medical Physics, University Medical Center Freiburg, Germany*

(Dated: April 1, 2022)

We review, systematize and discuss models of diffusion in neuronal tissue, by putting them into an overarching physical context of coarse-graining over an increasing diffusion length scale. From this perspective, we view research on quantifying brain microstructure as occurring along the three major avenues. The first avenue focusses on the transient, or time-dependent, effects in diffusion. These effects signify the gradual coarse-graining of tissue structure, which occurs qualitatively differently in different brain tissue compartments. We show that studying the transient effects has the potential to quantify the relevant length scales for neuronal tissue, such as the packing correlation length for neuronal fibers, the degree of neuronal beading, and compartment sizes. The second avenue corresponds to the long-time limit, when the observed signal can be approximated as a sum of multiple non-exchanging anisotropic Gaussian components. Here the challenge lies in parameter estimation and in resolving its hidden degeneracies. The third avenue employs multiple diffusion encoding techniques, able to access information not contained in the conventional diffusion propagator. We conclude with our outlook on the future research directions which can open exciting possibilities for developing markers of pathology and development based on methods of studying mesoscopic transport in disordered systems.

CONTENTS

* dima@alum.mit.edu
† sune@cfin.au.dk
‡ kiselev@ukl.uni-freiburg.de
§ els.fieremans@nyumc.org

I. DIFFUSION MRI THROUGH A BIRD'S EYE

> One of the most astonishing things about the world in which we live is that there seems to be interesting physics at all scales. ⟨...⟩ To do physics amid this remarkable richness, it is convenient to be able to isolate a set of phenomena from all the rest, so that we can describe it without having to understand everything. Fortunately, this is often possible. We can divide the parameter space of the world into different regions, in each of which there is a different appropriate description of the important physics. Such an appropriate description of the important physics is an "effective theory"
>
> H. Georgi, *Effective Field Theory* [1]

Diffusion MRI (dMRI) is a macroscopic physical measurement of the voxel-averaged Brownian motion of nuclear-spin-carrying molecules (typically water). This measurement occurs in a structurally complex tissue microenvironment such as the brain. Diffusion in complex media has been studied for about a century in a variety of fields, and is part of a broad class of transport phenomena in disordered systems.

Our goal in this review article is to place biophysical dMRI modeling into a broader physical context. Our overarching theme will be that of coarse-graining and effective theory, which will allow us to present and discuss neuronal tissue models of diffusion from a unifying perspective.

A. Mesoscopic Bloch-Torrey equation as an effective theory

One of the key 20$^{\rm th}$ century advances in understanding the physics of complex systems was achieved by the development of *effective theory*, a paradigm to describe dynamics that involves only a handful of the so-called *relevant degrees of freedom*, or *relevant parameters*, thereby ignoring myriads of other, "irrelevant" ones [2–4]. This way of thinking was spurred by attempts to describe systems with an ever greater number of degrees of freedom, and a subsequent realization that it is plain impossible to keep track of all of them at once.

The more complex the system, the more the challenge of building an adequate theory shifts towards identifying which (few) parameters to keep, and which ones (almost all!) to ignore. Over time, selecting relevant parameters and formulating an adequate effective theory has become synonymous with the notion of understanding the system's behavior.

Having NMR as an example, the quantum-mechanical couplings of a very complex multi-spin Hamiltonian, together with all molecular degrees of freedom describing rotations, vibrations and translations, relevant at the nm and ps level, average out to produce effective parameters such as the relaxation rates R_1 and R_2, and the diffusion coefficient D, at least for the most common NMR measurements. The parameters R_1 and R_2 emerge in Bloembergen–Purcell–Pound theory and enter the Bloch equations describing the semiclassical evolution of macroscopic magnetization [5, 6]. Reducing a myriad of variables describing molecular microenvironment to just a few relevant parameters has been a major scientific achievement of the 1940s–1960s NMR, and has formed the basis of effective theory of nuclear magnetization in liquids.

The step from NMR in uniform liquids to biological tissues has brought along a new challenge, which our community is only beginning to fully embrace. This challenge is associated with the above effective parameters $R_1(\mathbf{r})$, $R_2(\mathbf{r})$ and $D(\mathbf{r})$ acquiring *spatial dependence* in tissues — albeit at the much coarser scale $\sim 0.1-10\,\mu$m set by the cellular architecture. These spatial variations become relevant at the corresponding $\sim 1-1000$ ms time scales of dMRI, — much slower than the ps time scales on which the local relaxation rates and the diffusion coefficient emerge.

From the physics standpoint, the spatial variations of $R_1(\mathbf{r})$, $R_2(\mathbf{r})$ and $D(\mathbf{r})$ (with the latter including boundary conditions associated with cell membranes), occur at the *mesoscopic scale*, Fig. 1. The term "mesoscopic" originated in condensed matter physics some decades ago [7], signifying focussing on the intermediate scales ("meso"), in-between elementary (say, atomic or molecular), and macroscopic (associated with the sample size or the measurement resolution). By design, this term is relative, depending on which spatio-temporal scales are deemed small and large.

For dMRI, the mesoscopic scale corresponds to tissue heterogeneities at the scale defined by the MRI-controlled diffusion length, $L(t)\sim\sqrt{tD(t)}\sim 1-50\,\mu$m, which is the rms molecular displacement for times $t\sim 1-1000$ ms, and is therefore commonly referred to as the microstructural scale. This scale is commensurate with immense structural complexity of tissue microarchitecture.

At the mesoscale, quantum degrees of freedom become irrelevant (at least for the dMRI purposes), and the dynamics of transverse magnetization $m(t,\mathbf{r})$ (a two dimensional vector = complex number) can be captured by the *mesoscopic Bloch-Torrey equation*

$$\partial_t m(t,\mathbf{r}) = \partial_{\mathbf{r}}\left[D(\mathbf{r})\partial_{\mathbf{r}} m(t,\mathbf{r})\right] - \left[R_2(\mathbf{r}) + i\Omega(t,\mathbf{r})\right] m(t,\mathbf{r}). \tag{1.1}$$

Here $\Omega(t,\mathbf{r})$ is the Larmor frequency offset that may include externally applied diffusion-sensitizing gradients $\mathbf{g}(t)$, $\Omega(t,\mathbf{r}) = \Omega(\mathbf{r}) + \mathbf{g}(t)\mathbf{r}$, and the static $\Omega(\mathbf{r})$ arises from the intrinsic mesoscopic magnetic structure of tissues due to paramagnetic ions such as iron, or due to added contrast.

The Bloch-Torrey equation (1.1) is an adequate effective description at the μm level, commensurate with typical diffusion length scales probed with dMRI. It is a mesoscopic equation in the sense that it involves scales in-between the

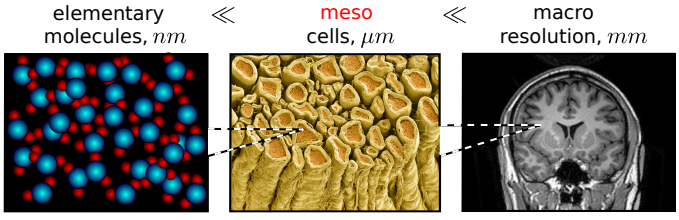

FIG. 1. The mesoscopic scale in brain dMRI, as an intermediate scale between the elementary (molecular) and the macroscopic (resolution).

quantum-mechanical molecular dynamics on the nm scale and the measurable signal in mm-sized MRI voxels. While the averaging up to the mesoscopic scale is already performed in its $\mathbf{r}$-dependent parameters, it is our task to perform the remaining averaging over a macroscopic voxel V inherent to the observed (complex-valued) signal $S[t, \mathbf{g}(t)] \propto \int_V \mathbf{dr}\, m(t, \mathbf{r})$, for which the μm-level spatially varying relaxation rates and diffusive properties produce the observable deviations from mono-exponential relaxation and Gaussian diffusion. It is because of this averaging, that in contrast to the quantum-mechanical description at the molecular level [5, 6] and classical electrodynamics-based considerations used in designing the MR hardware, addressing the mesoscopic tissue complexity requires bringing the tools and intuition from condensed matter and statistical physics.

The overarching goals of "microstructural", or "mesoscopic" MRI modeling are

(i). To identify the relevant tissue-specific parameters, which originate from $R_1(\mathbf{r})$, $R_2(\mathbf{r})$, $D(\mathbf{r})$, $\Omega(\mathbf{r})$, and survive in the voxel-averaged signal (i.e. to build an appropriate effective theory for the macroscopic signal);

(ii). To suggest optimal ways to probe them (i.e. to solve the corresponding parameter estimation problem).

Notice that to keep our terminology reasonably rigorous, we separated *modeling* into *theory* and *parameter estimation* (sometimes called "fitting"); hence our title. These two facets of modeling require very different tools and ways of thinking, as we will see below in Sections II and III, respectively.

B. Coarse-graining and emergent phenomena

Equation (1.1) is an example of an *effective theory* — i.e. an approximate description that emerges by averaging out the dynamics at the smaller spatial and temporal scales. It illustrates a general principle: pretty much every dynamical equation in physics is an effective theory (governed by an effective Hamiltonian or an effective action), i.e. it has *emerged* by identifying "collective" phenomena involving many-particle interactions at a more elementary level [1–4].

Over the past century, physicists have come to realize that, at each level of complexity, the effective theory and its relevant parameters can look very different [2], giving rise to the hierarchy of scales and of the corresponding emergent phenomena, from the most microscopic to the most macroscopic. Interactions between quarks and gluons give rise to protons and neutrons, so that their charge and mass can be viewed as effective parameters emerging by averaging over the quark/gluon degrees of freedom. Interactions between protons, neutrons and electrons give rise to all of chemistry, whereby the details of interactions between protons and neutrons inside nuclei become irrelevant. Interactions between molecules, coarse-grained over nm scale, give rise to classical hydrodynamics, statistical mechanics and eventually, to biology, and so on.

It is remarkable that, for instance, there is not a hint of classical hydrodynamics at the level of Schrödinger or Dirac equation describing the atomic structure; the large-scale hydrodynamic description *emerges* after a highly nontrivial averaging over the corresponding quantum degrees of freedom of many molecules. Refined methods such as renormalization [3, 4] have been crafted specifically to single out relevant parameters from the rest upon coarse-graining, proceeding from the shortest to the longest length scales and gradually averaging out the short-scale degrees of freedom, producing a fascinating hierarchy of all natural phenomena [2].

For quantifying tissue microstructure by measuring diffusion or transverse relaxation with MRI, the mesoscopic Bloch-Torrey equation (1.1) contains all relevant physical processes. This effective theory is as fundamental for the mesoscopic MRI, as the Schrödinger equation is for the nonrelativistic quantum mechanics, or the Navier-Stokes equation is for the classical hydrodynamics. It is always the starting point for developing biophysical models relating the NMR signal to the mesoscopic tissue architecture.

C. Diffusion as coarse-graining

Diffusion in heterogeneous media is a beautiful and simple example of coarse-graining. It can be thought of as a gradual "forgetting", or homogenizing over the increasing diffusion length. To illustrate this concept, consider a two-dimensional model example of a two-scale mesoscopic structure, represented by randomly placed impermeable disks of two different radii, embedded into an NMR-visible space with diffusion coefficient D_0, Fig. 2. To be specific, let us assign sizes, typical to cell dimensions: the small disks have radius $r_{\rm small} = 1\,\mu$m and the large ones are 20 times larger. In a (hypothetical) tissue, this could describe diffusion in the extra-axonal space transverse to a fiber tract, hindered by two types of axons. Here we consider diffusion as a physical phenomenon; its relation to NMR measurement is discussed below in Sec. I D.

At time $t \to 0$, each water molecule only senses its own immediate environment; all molecules see the same diffusion coefficient $D(0) = D_0$ assumed to be $\sim 1\,\mu{\rm m}^2/{\rm ms}$.

As time increases (top row of Fig. 2), molecules get restricted by the walls of both small and large disks. As small disks have much higher net surface area than the large ones, the hindrance occurs mostly due to the small ones. Hence, the decrease of the resulting voxel-averaged diffusion coefficient would happen on the scale of a few ms, mostly dominated by the geometry of the small disks at the scale $\sim 1\,\mu$m.

At $t \gtrsim 100\,$ms (bottom row), when the diffusion length $L(t)$ strongly exceeds the small disk size, the effect of the small disks has become coarse-grained (while the effect of the large disks is not). Now, we can view the medium in-between the large disks as a homogeneous "effective medium", with some effective diffusion coefficient $D_{\rm small} < D_0$ given by the macroscopic ("tortuosity") limit of a medium with the small disks only. It is important to note that if we did not have access to shorter times and could only resolve the diffusion times corresponding to the lower row of panels, there would be no way to identify the presence of the small disks

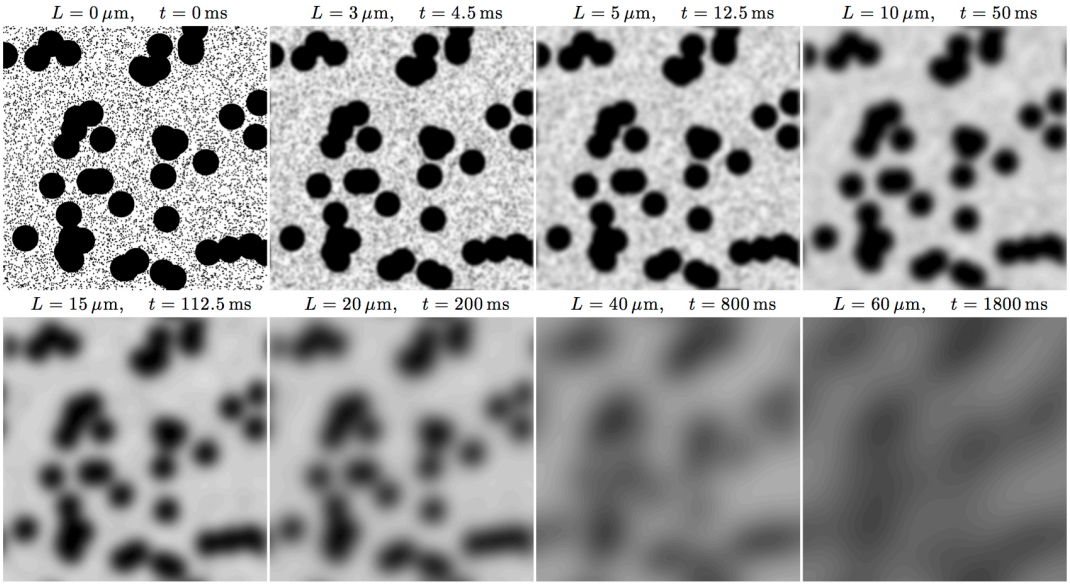

FIG. 2. **Diffusion as coarse-graining.** An example of a medium where the mesoscopic structure is created by randomly placing black disks of two different radii, $r_{\rm small} = 1\ \mu$m and $r_{\rm large} = 20\ \mu$m, top left panel. To obtain snapshots of the medium as effectively seen by the diffusing molecules at different time scales, we used a Gaussian filter with width $L/2$, where $L(t) = \sqrt{2Dt}$, and ignored the time dependence of $D(t)$ in the definition of diffusion length, using a typical value $D = 1\ \mu{\rm m}^2$/ms for illustration purposes (cf. Sec. II D below).

— their effect has been homogenized,[1] and their numerous parameters (e.g. size, coordinates) have become "irrelevant", with their only role in *renormalizing* D_0 down to $D_{\rm small}$.

Hence, from time $t \gtrsim 100$ ms on, we can adopt the coarse-grained description which only involves the large disks, immersed in a uniform medium with diffusion constant $D_{\rm small}$. The corresponding Eq. (1.1) would have the effective $D(\mathbf{r})$ varying at the scale associated with large disks, with $D(\mathbf{r}) \simeq D_{\rm small}$ outside them, and the short-distance spatial harmonics of $D(\mathbf{r})$ filtered out as it is obvious from Fig. 2; in Section II, we will rigorously justify and use this intuitive picture. The measured diffusion coefficient would further decrease with t at the scale of a few hundred ms, corresponding to being hindered by the large disks — the remaining restrictions.

Eventually, at even longer $t \gtrsim 1000$ ms, the effect of the large disks also becomes coarse-grained, and the whole sample looks as if it were homogeneous with some macroscopic diffusion coefficient D_∞, such that $0 < D_\infty < D_{\rm small} < D_0$. From this t onwards, one cannot distinguish this sample from a uniform medium with diffusion constant D_∞.

Our example shows that the hallmark of coarse-graining over larger- and larger-scale mesoscopic structure is the time-dependence of the overall diffusion coefficient. In view of this time dependence, it will be convenient to work with the *instantaneous* diffusion coefficient,

$$D_{\rm inst}(t) \equiv \frac{\partial}{\partial t}\frac{\langle \delta x^2(t)\rangle}{2}\,, \quad \delta x(t) = x(t) - x(0)\,, \qquad (1.2)$$

defined as the rate of change of the mean squared molecular displacement $\langle \delta x^2(t)\rangle$ in a particular direction $\hat{\mathbf{x}}$. (For simplicity, we assumed that our sample in Fig. 2 is statistically isotropic. For anisotropic samples, the diffusion tensor eigenvalues will acquire the time dependence.)

The average $\langle \dots \rangle$ in the definition (1.2) is actually a *double average*: (i) over the Brownian *paths* in the vicinity (of size $\sim L(t)$) of any given initial point $\mathbf{r}_0 \equiv \mathbf{r}(t)|_{t=0}$, yielding the local coarse-grained diffusivity value $D(\mathbf{r}_0)$; and (ii) over the *ensemble* of random walkers (spins) originating from all possible initial points $\mathbf{r}_0$. Because of the ensemble average, the measured diffusion characteristics, such as Eq. (1.2), describe a macroscopic sample *as a whole*. They do not belong to any given Brownian path, but rather emerge as a result of averaging (i) over all possible Brownian paths that could be taken by a given molecule, and (ii) over the initial positions of all molecules in a sample.

Upon taking into account increasing length scales, the effective voxel-averaged $D_{\rm inst}(t)$ *flows* towards the tortuosity limit D_∞, starting, as in our example, from the "microscopic" $D_0 > D_\infty$. We used the term "to flow" because the above picture mimics the *renormalization group flow* [3, 4] according to which the gradual evolution of a physically important parameter, such an elementary particle charge or an effective mass, occurs as a function of the coarse-graining length scale, from the high-energy = short distance scale, down to the low-energy parameters relevant for the more macroscopic description.

Looking back, there was nothing special about requiring the disks to be impermeable (the black regions could have corresponded to some medium with diffusion coefficient $D_1 \neq D_0$); we could have used objects of a non-disk shape,

[1] An experienced reader can recall the possibility to apply strong gradients $q \sim 1/r_{\rm small}$ to detect the small disks. This, however, practically necessitates using respetively short $t \sim 1/(D_{\rm small}\, q^2)$, cf. Sec. I F below.

and/or with non-sharp boundaries. Generally, as long as the random walkers can, in the limit $t \to \infty$, reach any point in a given "compartment", the above coarse-graining picture applies to this compartment. If a voxel contains multiple non-exchanging compartments, it applies to them separately, with the net signal given by a sum of their contributions.

A similar physical picture qualitatively applies to the effects of spatially varying $R_2(\mathbf{r})$ — e.g. if the black and white regions in Fig. 2 instead represented different local molecular-level R_2 values, and spins were able to diffuse everywhere. The above argument would then lead to an effective $R_2(\mathbf{r})$ entering Eq. (1.1) for times t exceeding the corresponding coarse-graining time scale. For instance, for $t \gtrsim 100$ ms, the effect of small disks would homogenize to produce a uniform $R_{2,\mathrm{small}}$ rate in-between the large disks, and so on, leading to the time-dependent overall observed $R_2(t)$ with an asymptotic macroscopic rate $R_2|_{t\to\infty}$ observable at very long t. Likewise, if mesoscopic structure in Fig. 2 represented spatially varying susceptibility $\chi(\mathbf{r})$, inducing the corresponding $\Omega(\mathbf{r})$, the resulting $R_2^*(t)$ rate would change — in this case, *increase* with t, approaching the $R_2^*(t)|_{t\to\infty}$ macroscopic value as a result of gradual coarse-graining.

We note that all the above mentioned quantities — D_{small} and $R_{2,\mathrm{small}}$; D_∞ and $R_2|_{t\to\infty}$; $R_2^*(t)|_{t\to\infty}$ — are *nonuniversal*, i.e. they depend on the numerous structural details, such as packing geometry (e.g., periodic versus random arrangement); they would change if the disks were instead squares, etc. Certainly, these quantities are not given by a simple averaging of the microscopic $D(\mathbf{r})$ or $R_2(\mathbf{r})$ over the sample. However, the *initial* values $D_{\mathrm{inst}}(0)$ and $R_2(0)$ are given by the sample-averaged $\langle D(\mathbf{r})\rangle$ and $\langle R_2(\mathbf{r})\rangle$, correspondingly, since at $t \to 0$ (practically, at times just exceeding the ps time scale necessary for the local $D(\mathbf{r})$ and $R_2(\mathbf{r})$ to emerge), each spin observes only its immediate molecular environment.

The picture of gradual coarse-graining over an increasing diffusion length has a number of important consequences:

1. The mesoscopic Bloch-Torrey equation (1.1) can be fully determined only after the relevant spatio-temporal scales are specified, since its parameters $R_2(\mathbf{r})$, $\Omega(\mathbf{r})$ and $D(\mathbf{r})$ are effective and, hence, scale-dependent.

2. Generally, the observed voxel-averaged diffusion coefficient and the effective relaxation rate would depend on time t because of the presence of the mesoscopic structure (such as $D_{\mathrm{inst}}(t)$ decaying from $D(0)$ down to D_∞ in our example of Fig. 2). This time t can be set by the measurement sequence, and varying it provides a unique window into the tissue architecture at the scale of the corresponding diffusion length $L(t)$.

3. This brings us to the fundamental challenge of interpreting such time dependencies in terms of the mesoscopic structural complexity. Practically, we must figure out which features in the effective $R_2(\mathbf{r})$, $\Omega(\mathbf{r})$ and $D(\mathbf{r})$ remain observable after the voxel-wise averaging as a result of a macroscopic acquisition (cf. Section II). This is the overarching task — and justification — for the theoretical efforts in our community.

4. If a measurement is too slow to track the transient processes, we are left (in each non-exchanging tissue compartment) with the $t \to \infty$ *macroscopic* Bloch-Torrey equation, i.e. Eq. (1.1) with *uniform* effective parameters $D(\mathbf{r}) \to D_\infty$, $R_2(\mathbf{r}) \to R_2(t)|_{t\to\infty}$, $\Omega(\mathbf{r}) \to \langle\Omega(\mathbf{r})\rangle$. Its solution becomes trivial — monoexponential relaxation and Gaussian diffusion (cf. Section III). However, the mesoscopic information is lost, since the signal is indistinguishable from that in a uniform compartment. The effective macroscopic parameters are in general quite different from the intrinsic mesoscopic ones; for instance, D_∞ can be notably lower than the intrinsic water or axoplasmic diffusion coefficient.

D. dMRI signal as the diffusion propagator; qt Imaging

So far we managed to get away with looking at a single equation (1.1) and wave hands based on drawing parallels with concepts developed in physics. It is now time to introduce basic notations; the content of this subsection should be familiar to anyone actively working in dMRI.

In what follows, for simplicity we will confine ourselves only to the mesoscopic structure as related to diffusion, and will assume the relaxation effects to be trivial (at least in each tissue compartment), setting $R_2(\mathbf{r}) \to R_2$, and a uniform susceptibility, such that $\Omega(\mathbf{r}) \to \langle\Omega\rangle$. (The nontrivial $R_2(\mathbf{r})$ and $\Omega(\mathbf{r})$ modify apparent diffusion metrics [8, 9]; this is beyond the scope of our review.) We can think of a situation when the relaxation physics has already become "macroscopic", while $D(\mathbf{r})$ is not fully coarse-grained. This allows us to factorize the magnetization $m(t,\mathbf{r}) \equiv e^{-R_2 t - i\langle\Omega\rangle t}\,\psi(t,\mathbf{r})$, where $\psi(t,\mathbf{r})$ is not subjected to the relaxation and frequency shift and obeys the following equation

$$\partial_t \psi(t,\mathbf{r}) = \partial_{\mathbf{r}}\left[D(\mathbf{r})\partial_{\mathbf{r}}\psi(t,\mathbf{r})\right] - i\mathbf{g}(t)\mathbf{r}\,\psi(t,\mathbf{r}). \qquad (1.3)$$

We focus here on the most easily interpretable measurement with very narrow gradient pulses.[2] As we now discuss, serendipitously, this measurement accesses the propagator of the mesoscopic diffusion equation, which (cf. Sec. I C) describes evolution of particle density $\rho(t,\mathbf{r})$

$$\partial_t \rho(t,\mathbf{r}) = \partial_{\mathbf{r}}\left[D(\mathbf{r})\partial_{\mathbf{r}}\rho(t,\mathbf{r})\right]. \qquad (1.4)$$

Unless otherwise stated, we apply Eqs. (1.3) and (1.4) to each non-exchanging tissue compartment.

The *fundamental solution* of equation (1.4), or *diffusion propagator* $\mathcal{G}_{t;\mathbf{r},\mathbf{r}_0}$, satisfies equation (1.4)

$$\partial_t \mathcal{G}_{t;\mathbf{r},\mathbf{r}_0} = \partial_{\mathbf{r}}\left[D(\mathbf{r})\partial_{\mathbf{r}}\mathcal{G}_{t;\mathbf{r},\mathbf{r}_0}\right] + \delta(t)\delta(\mathbf{r}-\mathbf{r}_0) \qquad (1.5)$$

[2] The case of long gradient pulses brings additional complications, which are relatively straightforward as compared to the overall understanding of diffusion in biological tissues. The relation of such measurements to the ideal pulsed diffusion gradients is analyzed theoretically in refs. [10–12] and concrete examples are given in refs. [13–17].

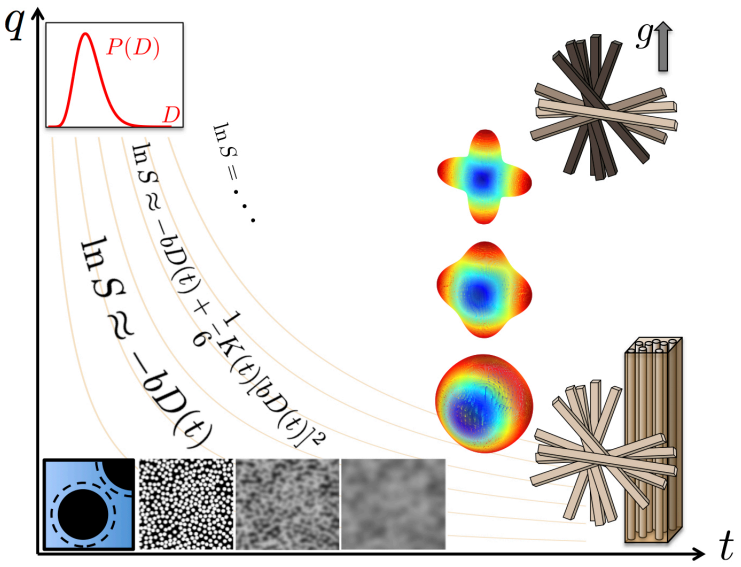

FIG. 3. The parameter space of dMRI is at least two-dimensional: By increasing q one accesses the progressively higher-order diffusion cumulants, Sec. I H, whereas the dependence along the t-axis reflects their evolution over an increasing diffusion length scale $\sim \sqrt{tD(t)}$, cf. Eq. (1.12). The b-value alone does not uniquely describe the measurement, unless diffusion in all tissue compartments is Gaussian; contour lines of $b = q^2 t$ are schematically drawn in beige. The hierarchy of dMRI models (pictures), cf. Fig. 4, as well as the subsequent terms in the cumulant representation, cf. Fig. 5, are superimposed. The decrease of the signal from axonal bundles parallel to the increasing gradient is shown by their darkening (top right corner). In Section II we focus on moving along the t-axis, and in Section III we consider moving along the q-axis at asymptotically long t. Section IV will be devoted to effects beyond this diagram, contained in voxel-averaged products of diffusion propagators at different t and q.

with the point and instant source at $\mathbf{r} = \mathbf{r}_0$. The source term corresponds to the solution with zero particle density for $t < 0$ and with the initial condition $\delta(\mathbf{r} - \mathbf{r}_0)$ instantly appearing at $t = 0$. The solution is thus proportional to the unit step function, $\theta|_{t>0} = 1$ and $\theta|_{t<0} = 0$, such that $\partial_t \theta(t) = \delta(t)$.

The propagator $\mathcal{G}_{t;\mathbf{r},\mathbf{r}_0}$ is a fundamental quantity describing the diffusion process around the point $\mathbf{r}_0$, with a meaning of the probability distribution function (PDF) of molecular displacements $\mathbf{r} - \mathbf{r}_0$ over time t. (This PDF can be sampled using Monte Carlo simulations by releasing random walkers all at once from the point $\mathbf{r}_0$.) Of course, since the local tissue structure is different around each initial point $\mathbf{r}_0$, the propagator $\mathcal{G}_{t;\mathbf{r},\mathbf{r}_0}$ depends on the points $\mathbf{r}_0$ and $\mathbf{r}$ separately.

The fundamental connection between the diffusion process (1.4) and the NMR measurement stems from the gradient-dependent phase of $\psi(t,\mathbf{r})$ as described by Eq. (1.3). In the limit of narrow pulses $\mathbf{g}(\tau) = \mathbf{q} \cdot [\delta(\tau - t) - \delta(\tau)]$ and the initial condition as in Eq. (1.5), the magnetization $\psi(t,\mathbf{r})$ differs from $\mathcal{G}_{t;\mathbf{r},\mathbf{r}_0}$ by the position-dependent phase $e^{-i\mathbf{q}(\mathbf{r}_t - \mathbf{r}_0)}$ acquired during the gradient application. The *diffusion-weighted signal*, which is a net magnetization $\int d\mathbf{r}\, m(t,\mathbf{r})$ in a voxel,

$$\frac{S(t,\mathbf{q})}{S(t,\mathbf{q})|_{\mathbf{q}=0}} = \int \frac{d\mathbf{r}_0 d\mathbf{r}_t}{V}\, e^{-i\mathbf{q}(\mathbf{r}_t - \mathbf{r}_0)}\, \mathcal{G}_{t;\mathbf{r}_t,\mathbf{r}_0} \equiv G_{t,\mathbf{q}} \quad (1.6)$$

becomes equivalent to a spatial Fourier transform of the *voxel-averaged propagator*

$$G_{t,\mathbf{r}} \equiv \langle \mathcal{G}_{t;\mathbf{r}_0+\mathbf{r},\mathbf{r}_0} \rangle_{\mathbf{r}_0} = \int \frac{d\mathbf{r}_0}{V}\, \mathcal{G}_{t;\mathbf{r}_0+\mathbf{r},\mathbf{r}_0}\,. \quad (1.7)$$

In Eq. (1.6) we divided by the voxel volume V, such that the unweighted signal (the right-hand side) is normalized to unity. A thorough discussion can be found e.g. in ref. [18].

Note that exact "local" propagator $\mathcal{G}_{t;\mathbf{r}_t,\mathbf{r}_0}$ is not translation invariant, i.e. it depends on the absolute coordinates $\mathbf{r}_t$, $\mathbf{r}_0$ (and time t). The voxel-averaging in Eq. (1.6) automatically restores translation invariance, which means that the measured propagator G is parameterized by the two variables: the spatial displacement $\mathbf{r} \equiv \mathbf{r}_t - \mathbf{r}_0$ and the diffusion time interval t (equivalently, by $\mathbf{q}$ and t).

Hence, the parameter space of dMRI fundamentally consists of $\mathbf{q}$ and t, Fig. 3 (here we dropped the directionality in $\mathbf{q}$ in order to not overload the picture). Literally speaking, mapping the diffusion propagator in the space of $\mathbf{q}$ and t can be referred to as qt Imaging.[3] For multiple diffusion encoding, which maps a more complex object than the diffusion propagator (Section IV), the parameter space in principle depends on the multiple $\mathbf{q}$ and t intervals.

The so-called b-value [21] has historically become the often single-quoted measurement parameter. However, it only defines the measurement *if diffusion is Gaussian in every compartment*, in which case the diffusion propagator

$$G^{(0)}_{t,\mathbf{q}} = \theta(t)\, e^{-Dq^2 t} \equiv \theta(t)\, e^{-bD}\,, \quad b \equiv q^2 t \quad (1.8)$$

in each compartment is determined solely by the parameter combination $q^2 t$. Schematically, the contour lines of constant b are outlined in Fig. 3. In general, for anisotropic tissues such as brain white matter, Gaussian diffusion in each compartment is described by the diffusion tensor, $bD \to b_{ij} D_{ij}$, where the b-matrix [22] $b_{ij} = q_i q_j\, t$.

The Gaussian limit (1.8), and its more general anisotropic Gaussian limit, are hallmarks of "full" coarse-graining, which occurs in the $t \to \infty$ limit, cf. Fig. 2. In this case, no matter how structurally complex the tissue, it can be modeled as a sum of (anisotropic) Gaussian signals. Section III will be devoted to the picture of multiple Gaussian compartments (the Standard Model), cf. the column of pictures at long t in Fig. 3.

[3] `cu-tie imaging, or qtI` *(noun)*: A noninvasive medical imaging technique for spatio-temporal mapping of the diffusion propagator in soft tissues in order to quantify tissue structure below the nominal MRI resolution. Of course, it is nothing but the familiar q-space imaging [10, 19, 20] sampled at various t, but don't we all need a new acronym once in a while?

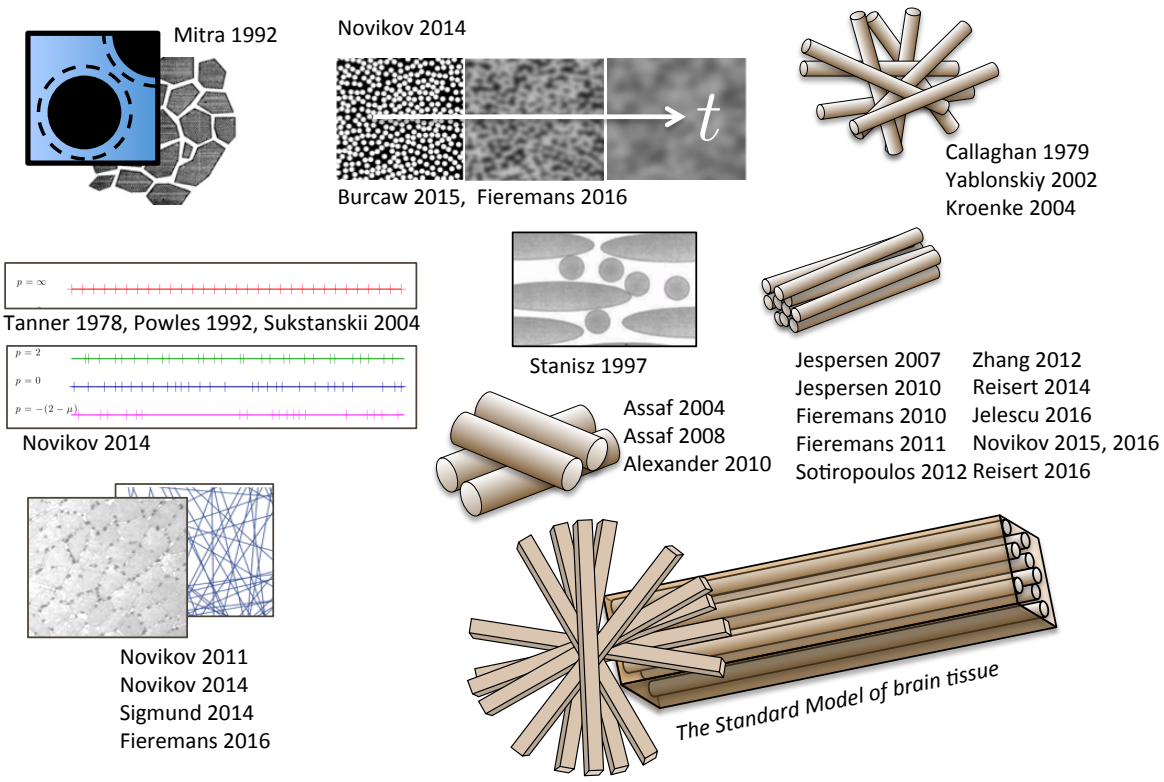

FIG. 4. **Models are pictures...** Here they are drawn with coarse-graining occurring, roughly, from left to right. References: Mitra 1992 [23], universal short-t limit; Novikov 2014 [24], universal long-t behavior; Burcaw 2015 [14] and Fieremans 2016 [25], long-t behavior transverse and along WM fibers; Tanner 1978 [26], Powles 1992 [27], Sukstanskii 2004 [28], periodic 1-dimensional lattice; Novikov 2011 [29], random permeable barriers in any dimension, and its application to myofibers (Sigmund 2014 [30] and Fieremans 2016 [31]); Callaghan 1979 [32], first model of diffusion inside random narrow cylinders; Yablonskiy 2002 [33], diffusion in finite-diameter cylinders modeling lung alveoli; Stanisz 1997 [34], first model for WM fiber tracts made of ellipsoids; Assaf 2004 [35], CHARMED; Assaf 2008 [36], AxCaliber; Alexander 2010 [37], ActiveAx; Kroenke 2004 [38], NAA diffusion inside neurites. The widely adopted $t \to \infty$ picture of narrow "sticks" for the neurites, embeded in the extra-neurite space (the Standard Model): Jespersen 2007 [39], Jespersen 2010 [40], Fieremans 2010 [41], Fieremans 2011 (WMTI) [42], Sotiropoulos 2012 (Ball and rackets) [43], Zhang 2012 (NODDI) [44], Reisert 2014 (MesoFT) [45], Jelescu 2016 (NODDIDA) [46], Novikov 2015, 2016 (LEMONADE, RotInv) [47, 48], Reisert 2016 (Bayesian RotInv) [49].

$$S = w_1 e^{-bD_1} + w_2 e^{-bD_2}$$
Le Bihan 1991

$$\ln S = -b_{ab} D_{ab}$$
Basser 1994

$$S = \int e^{-bD} P(D) dD$$
Yablonskiy 2003
Wang 2011
White 2013
Scherrer 2016

$$\ln S = -b_{ab} D_{ab} + \frac{1}{6} b^2 n_a n_b n_c n_d W_{abcd}$$
Jensen 2005, Kiselev 2011

$$P(\mathbf{r}) = \sum_{N=0}^{N_{\max}} \sum_{\mathrm{n}_1,\mathrm{n}_2,\mathrm{n}_3} a_{\mathrm{n}_1,\mathrm{n}_2,\mathrm{n}_3} \Psi_{\mathrm{n}_1,\mathrm{n}_2,\mathrm{n}_3}(\mathbf{A}, \mathbf{r})$$
Özarslan 2013

$$S = \frac{1}{-i\omega + R_2 + Dq^2 - \Sigma(\omega, q)}$$
Novikov 2008, Novikov 2010

FIG. 5. **...while representations are formulas.** References: Le Bihan 1991 [50], first biexponential representation of dMRI signal from brain; Basser 1994 [22], diffusion tensor imaging (DTI); Jensen 2005 [51], diffusion kurtosis imaging (DKI); Kiselev 2011 [11], cumulant expansion; Novikov 2008 and 2010 [18, 52], effective medium theory (transverse relaxation and diffusion, correspondingly); Özarslan 2013 [53], expansion in harmonic oscillator basis; Yablonskiy 2003 [54], inverse Laplace transform (multi-exponential representation). Anisotropic multi-exponential representations: Wang 2011 [55], diffusion basis spectrum imaging (DBSI); White 2013 [56], restriction spectrum imaging (RSI); Scherrer 2016 [57], distribution of anisotropic microstructural environments in diffusion-compartment imaging (DIAMOND).

E. Hierarchy of diffusion models based on coarse-graining: The three regimes

From the unifying coarse-graining point of view, we can now categorize biophysical models of diffusion, Fig. 4, into the following three regimes. In either of the regimes, the theoretical treatment simplifies. The regimes can be arranged according to the increasing diffusion length $L(t)$ relative to characteristic mesoscopic tissue length scales:

(i). The Mitra *et al.* [23] universal short-time limit of the diffusion coefficient. The relevant parameter is the net surface-to-volume ratio of all barriers (e.g. cell walls). Here, the coarse-graining over the barriers has not yet occurred; cf. Sec. II C for an example in the brain.

(ii). Coarse-graining over the structural disorder [24] results in the power-law approach $t^{-\vartheta}$ of the instantaneous diffusion coefficient $D_{\rm inst}(t)$ towards the $t \to \infty$ limit D_∞. Here, the power-law exponent ϑ is connected to the large-scale behavior of the density correlation function of the hindrances to diffusion, and to the spatial dimensionality, yielding qualitatively distinct behavior along [24, 25] and transverse [14, 25] to the neurites in the brain. In Section II we argue, following ref. [24], that the more heterogeneous, or "disordered", the sample is, the slower the approach (the smaller the exponent ϑ). Conversely, in ordered media, such as in the model of perfectly ordered membranes [24, 28], the approach of $D_{\rm inst}(t)$ towards D_∞ occurs exponentially fast.

(iii). Finally, when the coarse-graining is complete, diffusion in each permeable tissue compartment has approached its $t \to \infty$ Gaussian (tortuosity) limit, as discussed above (cf. also a more detailed discussion in Sec. I I below). If there is no exchange between compartments, we obtain the most common, "multi-exponential" model. For neuronal tissue, the compartments are anisotropic due to the presence of effectively one-dimensional neurites. In Fig. 4, we introduce the Standard Model of neuronal tissue that accounts for the neurites with associated extra-neurite space, both subjected to orientation dispersion (cf. Section III). While known under a plethora of names and abbreviations [38–49, 58, 59], from the physics standpoint, this is practically the same model, with differences in the parameterization of the neurite orientation distribution function and variations in the descriptions of the extracellular space, as well as in the model parameter estimation procedures and employed parameter constraints.

The cross-over between regimes **(i)** and **(ii)** occurs when the diffusion length, $L(t)$, is commensurate with the characteristic length scale of the structural disorder. The instantaneous diffusion coefficient $D_{\rm inst}(t)$ decreases with time within this cross-over; while no general results are available there, it can be studied using numerical simulations.

F. How to become sensitive to short length scales?

Working in the $t \to \infty$ limit **(iii)** can only give us compartment volume fractions and their diffusion coefficients. Coarse-graining has already occurred and apparently washed out all traces of other microstructural parameters.

Determining characteristic μm-level length scale(s) l_c, such as the correlation length of the arrangement of tissue building blocks (e.g. disk radii in Fig. 2), is in principle possible using deviations from the Gaussian signal shape. In the spirit of Fig. 3, varying either t or q can yield the sensitivity of the diffusion signal (propagator) to the length scale, via the diffusion length $\sqrt{D(t)t}$ [cf. Eq. (1.12) below], and $1/q$, respectively. However, as we now discuss, these theoretically distinct ways are not that different in a sense that varying q implies being able to resolve correspondingly short $t \sim t_c$, where $t_c \sim l_c^2/D(t_c)$.

Varying t amounts to literally observing the diffusive dynamics for short times, when the coarse-graining has not yet fully occurred, such as at the stages **(i)** and **(ii)** above. In our example in Sec. I C, to identify the presence of the small disks, one could try, e.g., detecting time dependence in $D_{\rm inst}(t)$ or in $D(t)$ at $t \sim r_{\rm small}^2/D_0$. The random permeable barrier model [29, 31], a candidate for diffusion transverse to myofibers and for one-dimensional hindrances along the neurites [24], is an example where one can trace the effect of coarse-graining in $D_{\rm inst}(t)$ or in $D(t)$ across the regimes **(i) – (iii)**.

Varying q, by employing strong narrow gradients (with width $\delta \ll t_c$ so that q is well-defined [10–17]), can in principle allow one to "unravel" the coarse-graining, i.e. to observe features in $q \sim 1/l_c$ even when $t \gg t_c$.[4] However, the price to pay for employing times $t \gg t_c$, is the suppression of the signal, typically exponentially as $\sim e^{-D(t)q^2t} \ll e^{-D(t_c)q^2t_c}$. The connection between t and q is technically established within the effective medium theory [18], where the average propagator (1.7) is represented in the Fourier domain as

$$G_{\omega,\mathbf{q}} = \frac{1}{-i\omega + D_\infty q^2 - \Sigma(\omega,\mathbf{q})}\,. \tag{1.9}$$

(The self-energy part $\Sigma(\omega,\mathbf{q})$, a signature of heterogeneous media, vanishes for Gaussian diffusion, for which $G^{(0)}_{\omega,\mathbf{q}}$ is a Lorentzian.) The signal $G_{t,\mathbf{q}}$, measured in $(t,\mathbf{q})$ domain, is largely determined by the *complex pole* of Eq. (1.9), corresponding to the *dispersion relation* $\omega = \omega(\mathbf{q})$ which turns the denominator to zero; this relation self-consistently determines the corresponding time scale $t \sim 1/\omega(\mathbf{q})$ for which the corresponding $G_{t,\mathbf{q}} \sim e^{-D(t)q^2t}$ is not very strongly suppressed. Generally, the deviation from the pole $\omega = \omega(\mathbf{q})$ is possible, but it dramatically reduces the signal.

---

[4] In the language of emergent phenomena, Sec. I B, this would be analogous, e.g., to using neutron scattering (with large wave vectors $q > 1\ \mathrm{nm}^{-1}$) in order to resolve atomic structure of the fluid, for which the coarse-grained (large t and $r \gg 1/q$) continuous description is classical hydrodynamics.

An interesting interplay between coarse-graining scales occurs in tissues consisting of non-exchangeable compartments of different nature. Consider an example of a tissue consisting of a permeable compartment (extra-cellular space), and a fully restricted one (cells of size a). The diffusional coarse-graining in the latter stops at the time $t_a \sim a^2/D$. The whole medium possesses two relevant scales, $L(t)$ and a, which are markedly different for long times when $L(t) \gg a$. An experimentalist working in this limit has a choice of selecting the wave number q of diffusion measurements (the strength of diffusion weighting). The choice $q \sim 1/a$ (diffusion diffraction [60]) enables measuring the size of the restricted compartment, but strongly suppresses the signal from the permeable one. The choice $q \sim 1/L(t)$ enables observation of diffusion dynamics in the permeable compartment. The signal from the restricted compartment remains unsuppressed, such that both the signal attenuation $-\ln S \sim (qa)^2 \ll 1$ and the diffusivity $D(t) \sim a^2/t \ll 1$ become negligible; one can then formally treat such a compartment as Gaussian with its diffusion coefficient $D \to 0$. This leads to the picture of zero-radius "sticks" in the brain (neurites with zero diffusivity in the transverse direction), cf. Sec. III A below.

G. Models versus representations

Models are pictures (Fig. 4), exemplifying a rough sketch of physical reality, specified by their *assumptions* meant to simplify nature's complexity. This simplification relies on averaging over the irrelevant degrees of freedom, and keeping only a handful of relevant parameters describing the corresponding effective theory. Model assumptions are therefore a claim for the relevant parameters. They are more important than mathematical expressions, as they prescribe a parsimonious way to think about the complexity. Model validation is thereby validation of our frame of thinking.

A *representation* could be defined as a model-independent mathematical expression used to store, to compress, or to compare measurements. It can be realized as a function with a few adjustable parameters or a set of coefficients for a decomposition in a basis (cf. Fig. 5 for a few most commonly used representations in dMRI). In contrast to models, representations are as general as possible, and have very little assumptions. As there are infinite ways to represent a continuous function, the choice of representation is often dictated by convenience or tradition. Practically, not all representations are equivalent because one only uses a few basis functions rather than an infinite set; from this standpoint, sparser representations are more favorable. By construction, representations do not carry any particular physical meaning and hence do not immediately invoke any picture of physical reality; one can say that **representations are formulas.**

H. The cumulant expansion as a default representation

If a given compartment is not too heterogeneous (at least beyond a given coarse-graining scale), the corresponding diffusion propagator should not be too different from a Gaussian, Eq. (1.8). It is not surprising that the diffusion propagator admits a widely used regular expansion [11, 61]

$$\ln G(t,\mathbf{q}) \simeq -D_{ij}(t)q_iq_j + \frac{1}{6}(\bar{D}t)^2 W_{ijkl}(t)q_iq_jq_kq_l - \dots \tag{1.10}$$

in powers of $\mathbf{q}$, describing the deviation from the Gaussian form (1.8). (The summation over the repeated coordinate indices $i,j,\dots = 1\dots 3$ is implied throughout.)

The propagator expansion (1.10) stems from the corresponding cumulant expansion in probability theory noticed almost a century ago by Fisher and Wishart [62, 63]. For diffusion, only even orders in this series are nonzero due to the time-translation invariance in the absence of the bulk flow. Typically, the Taylor series (1.10) converges within a finite radius in q which is model-dependent [64, 65] .

A general diffusion propagator will have all even cumulant terms $D_{ij}(t)$, $W_{ijkl}(t)$, ... nonzero and diffusion time-dependent [11, 18]. Experimentally we often only access a few first terms, especially when using low diffusion weighting on clinical systems.

Upon coarse-graining, for a given tissue compartment the higher-order terms $W_{ijkl},\dots$ flow to zero, such that the signal approaches the Gaussian form (1.8) as $t \to \infty$. In this limit, the higher-order cumulant terms of the net diffusion propagator can originate only from the partial contributions from different tissue compartments (since a sum of Gaussians is non-Gaussian).

The series (1.10) *generates* the cumulants $\langle x_j x_j \dots\rangle_c$ (see e.g. refs. [11, 62, 63] for definition) of the PDF of molecular displacements[5] (1.6), via taking derivatives at $\mathbf{q}=0$, such as

$$\langle x_i x_j\rangle \equiv \int \mathbf{dr}\, x_i x_j\, G_{t,\mathbf{r}} = -\left.\frac{\partial^2}{\partial q_i \partial q_j}\right|_{\mathbf{q}=0} \int \mathbf{dr}\, e^{-i\mathbf{qr}} G_{t,\mathbf{r}}\,. \tag{1.11}$$

This procedure defines the *cumulative* diffusion coefficient

$$D(t) = \frac{\langle x^2(t)\rangle}{2t}\,, \tag{1.12}$$

or, more generally, the cumulative diffusion tensor

$$D_{ij}(t) = \frac{\langle x_i(t)x_j(t)\rangle}{2t} \tag{1.13}$$

(a symmetric 3×3 matrix with 6 independent parameters in 3 dimensions). These objects are defined in terms of the *average rate of change* of the mean-squared molecular displacement over the whole interval $[0,\ t]$ (in contrast to the instantaneous rate of change (1.2) above).

The linear estimation problem for $D_{ij}(t)$, referred to as the *diffusion tensor imaging (DTI)*, has been solved by Basser *et*

[5] Since $G_{t,\mathbf{r}}$ is written in terms of the *relative* displacements $\mathbf{r} = \mathbf{r}_t - \mathbf{r}_0$, we re-denote $\delta x_i(t) \to x_i(t)$ in Eq. (1.12) in order to simplify the notation, and drop the dependence on the initial position in the view of the translational invariance property (1.7).

al. [22]. It requires[6] a diffusion measurement along at least 6 non-collinear gradient directions in addition to at least one more, e.g. the $b = 0$ (unweighted) image.

Likewise, the linear estimation problem for both the diffusion and kurtosis tensors, via the expansion up to $\sim q^4 \sim b^2$, called *diffusion kurtosis imaging (DKI)*, has been introduced by Jensen *et al.* [51, 66]. It involves the $4^{\rm th}$ order cumulant $\langle x_i x_j x_k x_l \rangle_c$ related to $W_{ijkl}(t)$, with $\bar{D} \equiv \frac{1}{3}\,{\rm tr}\, D_{ij}(t)$. The number of parameters are now $6 + 15 = 21$, hence one needs at least two $b \neq 0$ shells in the q-space, and at least 15 non-collinear directions. The weights for unbiased estimation of diffusion and kurtosis tensors for non-Gaussian MRI noise were found recently [67].

A general method to calculate the number of parameters for a given order l_c of the cumulant series (1.10) in 3 dimensions is based on the SO(3) representation theory (known in physics as theory of angular momentum in quantum mechanics). A term $\sim q^{l_c}$ of even rank l_c is a fully symmetric tensor, which can be represented as a sum of the so-called symmetric trace-free (STF) tensors of ranks l_c, $l_c - 2$, ..., 2, 0 [68]. Each set of $2l + 1$ STF tensors of rank l realizes an irreducible representation of the SO(3) group of rotations, equivalent to a set of $2l + 1$ spherical harmonics Y_{lm} [68]. Hence, the total number n_c of nonequivalent components in the rank-l_c cumulant tensor is

$$n_c(l_c) = \sum_{l=0,2,\ldots}^{l_c} (2l+1) = \frac{1}{2}(l_c+1)(l_c+2)\,, \qquad (1.14)$$

so that $n_c = 6$ for DTI ($l_c = 2$) and $n_c = 15$ for DKI ($l_c = 4$).

Suppose we truncate the cumulant series (1.10) at an (even) term of rank $l_c = l_{\rm max}$. Hence we determine all the parameters of cumulant tensors (diffusion, kurtosis, ...) of ranks 2, 4, ..., $l_{\rm max}$. The total number of parameters in the truncated series

$$N_c(l_{\rm max}) = \sum_{l=2,4,\ldots}^{l_{\rm max}} n_c(l) = \frac{1}{12}\,l_{\rm max}^3 + \frac{5}{8}\,l_{\rm max}^2 + \frac{17}{12}\,l_{\rm max} \qquad (1.15)$$

corresponding to $N_c = 6,\ 21,\ 49, \ldots$ for $l_{\rm max} = 2,\ 4,\ 6, \ldots$. Hence, DTI yields 6 parameters, DKI yields 21, etc. (Here we did not include the proton density $S|_{b=0}$ in our counting.)

The cumulants D_{ij}, W_{ijkl}, ... of the signal obtained via Taylor-expanding its logarithm in the (even) powers of q_i, or equivalently, in the powers of b, correspond to the cumulants of the genuine PDF of molecular displacements $\mathbf{r} = \mathbf{r}_t - \mathbf{r}_0$ only in the narrow pulse limit, and in the absence of the mesoscopic magnetic structure (uniform R_2 and Ω). When the finite gradient pulse duration δ is comparable to the time scale of the transient processes, the measurement acts as a low-pass filter with a cutoff frequency $\sim 1/\delta$ [10–12, 14–17].

I. Normal or anomalous diffusion?

For finite t, the diffusion propagator in a heterogeneous medium is never Gaussian. The existence of domains with slightly different "local" $D(\mathbf{r})$ at a given coarse-graining scale necessarily yields the time-dependent $D_{\rm inst}(t)$, as well as the higher-order terms in q, such as q^4, in the Taylor expansion of $\ln G^{(0)}(t, \mathbf{q})$ [18, 24]. Upon coarse-graining, these terms gradually flow to zero, and $D_{\rm inst}(t) \to D_\infty$, such that diffusion becomes Gaussian *asymptotically* as $t \to \infty$ in each separate tissue compartment. This was the picture of Sec. I C, cf. Fig. 2. In particular, we implied that the diffusion coefficient decreases, as a result of the coarse-graining, towards its *finite* tortuosity asymptote $D_{\rm inst}(t)|_{t\to\infty} \equiv D_\infty > 0$. How reliable is this picture? What does it take to destroy it?

Existence of finite D_∞ is equivalent to mean squared displacement $\langle x^2(t)\rangle \simeq 2D_\infty \cdot t$ growing linearly with time for sufficiently long t, — this is a direct consequence of the definition (1.2). One says that diffusion asymptotically becomes "normal", i.e. the PDF of molecular displacements over a sufficiently large t approaches normal (Gaussian) distribution, cf. Eq. (1.8) with $D \to D_\infty$. Of course, if there are two or more non-exchanging tissue compartments, the total distribution will be non-Gaussian (as a sum of Gaussians with different D_∞), but this non-Gaussianity is in a sense trivial; the total D_∞ would still exist (given by a weighted average for the corresponding compartment values) [41], and the scaling $\langle x^2(t)\rangle \sim t$ at large t would hold.

There exists a radical alternative, when $\langle x^2(t)\rangle \sim t^\alpha$ for $t \to \infty$, with exponent $\alpha \neq 1$ — the so-called *anomalous diffusion* [69]. According to the definition (1.2), $D_\infty = 0$ for $\alpha < 1$, and $D_\infty = \infty$ for $\alpha > 1$. In other words, *observation of anomalous diffusion is equivalent to stating that the macroscopic diffusion coefficient D_∞ does not exist*. (The trivial case $D(t) \sim a^2/t$ for a fully restricted compartment of size a is not considered anomalous; $\langle x^2\rangle \sim a^2$, $\alpha = 0$.)

The absence of D_∞ would be a drastic claim. In neuronal tissue, one always observes finite D_∞ in non-confining compartments (e.g. in the extra-cellular space), Section II, hence diffusion is empirically never anomalous [14, 24, 25] for brain dMRI.[7]

From the point of coarse-graining, anomalous diffusion means that the sample never quite looks homogeneous —

[6] DTI, contrary to a widespread misconception, does *not* assume Gaussian diffusion, as it merely provides the lowest-order cumulant term D_{ij}, and tells nothing about the higher-order terms in the series (1.10). DTI applicability is thus dictated by the kurtosis term W to have negligible bias on the estimated D_{ij}, and the employed b-range is practically set by balancing the bias when b is too large and precision loss when b is too small.

[7] We are not reviewing the MRI literature on anomalous diffusion, since our goal here is to discuss models which are relevant to observable diffusion effects in neuronal tissue. A curious reader can find occasional claims of anomalous diffusion, or dMRI signal as a stretched-exponential. We are not aware of examples of a constructive derivation of the non-Gaussian fixed point [3, 4] starting from the stationary mesoscopic disorder with properties relevant to the brain. Hence, these claims can merely be viewed as postulates "proven" by fitting in a finite range of t or q.

for example, a fractal has self-similar structure, which implies similar statistics of static structural fluctuations at every length scale. In other words, when the coarse-graining over some scale has taken place, a larger scale looks statistically similar, so that the already averaged structural features are never forgotten, since they are reproduced again and again. In contrast, the structure in Fig. 2 implies that this memory is forgotten as $t \to \infty$ because there are only two dominant spatial scales.

Tissues empirically do not look self-similar; usually, when we look at a histological slide without a scale bar, we can still roughly say at which resolution the sample is imaged because usually cell size is well defined (for a given tissue type) — otherwise, medical students would not pass their pathology exams. For instance, when we look at cross-sections of white matter tracts, the majority of axons are of the order of $\sim 1\,\mu$m in diameter [70–72], and the section does not look the same when magnified by factors of 10, 100, or 0.1, 0.01, etc. A more quantitative statement can be made by studying large-distance scaling behavior of the density-density correlation function of the tissue structure; recent investigation [14] confirms that the structural fluctuations in white matter tracts are short-range (and not diverging at large length scales).

When *can* anomalous diffusion arise? In a broader context, this fundamental question has been extensively studied for the Fokker-Planck equation

$$\partial_t \psi(t,\mathbf{r}) = \partial_{\mathbf{r}} \left[D(\mathbf{r}) \partial_{\mathbf{r}} \psi(t,\mathbf{r}) \right] - \partial_{\mathbf{r}} \left[\mathbf{v}(\mathbf{r}) \psi(t,\mathbf{r}) \right], \quad (1.16)$$

where in addition to the "diffusive" flow $\mathbf{j}(t,\mathbf{r}) = -D(\mathbf{r})\partial_{\mathbf{r}}\psi(t,\mathbf{r})$ (Fick's law), one considers mesoscopic *random flow* because of some stationary local "velocity", or "force" field $\mathbf{v}(\mathbf{r})$ (imagine active streams, such as vortices or currents in an ocean [73]). Equation (1.16) arises as a conservation law $\partial_t \psi = -\partial_{\mathbf{r}} \cdot \mathbf{j}$, where the total flow

$$\mathbf{j} = -D(\mathbf{r})\partial_{\mathbf{r}}\psi(t,\mathbf{r}) + \mathbf{v}(\mathbf{r})\psi(t,\mathbf{r}) \,.$$

It turns out that the presence of the random flow term $\mathbf{v}(\mathbf{r})$ with short-range spatial correlations can drastically change the dynamics in dimensions $d \leq 2$ and drive the system away from the Gaussian diffusion. In dimension $d = 1$, random force field causes sub-diffusive behavior $\langle \delta x^2 \rangle \sim \ln^4 t$, a famous result by Sinai [74]. In $d = 2$ dimensions, super-diffusive behavior occurs when the flow $\mathbf{v}(\mathbf{r})$ is solenoidal, $\mathrm{div}\, \mathbf{v}(\mathbf{r}) = 0$, and sub-diffusive if it is potential, $\mathrm{curl}\, \mathbf{v}(\mathbf{r}) = 0$ [73, 75–77].

In the absence of the random forces, $\mathbf{v} \equiv 0$, small fluctuations in $D(\mathbf{r})$ do not destroy the "trivial" Gaussian fixed point in dimensions $d > 0$ [78, 79]. In other words, for the spatial short-range disorder in $D(\mathbf{r})$ to become relevant (i.e. to increase under the renormalization group flow), and for the anomalous diffusion to take over, the spatial dimension should formally be $d = 0$. What this tells is that it is very difficult, without the flow term, to break the trivial Gaussian fixed point of the finite tortuosity limit, at least starting from the weak disorder in $D(\mathbf{r})$. Extremely strong disorder, which is specially tuned, can induce the *percolation transition* [80] $D_\infty \to 0$; another possibility for destroying finite D_∞ is to create the disorder in the mesoscopic $D(\mathbf{r})$ with anomalously divergent spatial fluctuations [81, 82]. To the best of our knowledge, neuronal microstructure is compatible neither with percolation transition, nor with diverging structural fluctuations [14].

To recap, coarse-graining over an increasing diffusion length $L(t)$ provides a physical picture for time-dependent diffusion in mesoscopically disordered samples. Hence, generally, *diffusion is almost always non-Gaussian, but almost never anomalous*. In the brain, it is not anomalous specifically because the density fluctuations of brain structural units do not diverge at large scales, and because the "active" flow effects (microstreaming, axonal transport) have been recently estimated to be numerically negligible [83].

II. TIME-DEPENDENT DIFFUSION IN NEURONAL TISSUE

> Everything should be made as simple as possible, but not simpler
>
> Albert Einstein

The intuition of Sec. I C suggests that the time-dependence of the diffusion coefficient, e.g. defined as in Eq. (1.2), is a hallmark of the mesoscopic structure, and the associated transient time scale can be translated to the corresponding mesoscopic length scale. Determining and validating the μm-level relevant tissue length scales is the ultimate test of our ability to "quantify microstructure" — after all, how else would we know that we are indeed sensitive to the *micro*structure?

The practical purpose of this Section is to focus on ways to determine such length scales. Fundamentally, observation of the time dependent $D(t)$ is significant because it tells that *diffusion is non-Gaussian in at least one of the tissue compartments*. Indeed, consistent with the overall coare-graining picture, the time-dependent $D(t)$ must necessarily lead to the nonzero kurtosis and the higher-order cumulants [18], arising from the same mesoscopic heterogeneity which has not yet been fully coarse-grained. Conversely, if diffusion is Gaussian in all tissue compartments, the overall diffusion coefficient is time-independent [41].

We begin this Section by reviewing experimental data on the time-dependent diffusion coefficient and kurtosis in brain, and then discuss the two physically distinct regimes of time-dependence, according to the hierarchy of Sec. I E: the short-time regime **(i)** and the long-time regime **(ii)**, leading towards the asymptotically Gaussian diffusion in each non-exchanging tissue compartment, as discussed in the next Section.

Certainly, experimentally we are almost never in a pure limit — rather, we are typically in some cross-over, e.g. in-between the regimes **(i)** and **(ii)**. However, it is important to understand the behavior of the system in certain limits where it can be modeled with more confidence. Performing experiments in such limiting regimes is a great way to validate mod-

els through observing *definitive functional dependencies* on the model and measurement parameters, and identify the relevant degrees of freedom, which can then be incorporated into more complex theories of the cross-over behavior relevant to a broader range of dMRI studies, and for clinical translation.

A. Time dependent diffusion in the brain: To be or not to be?

Empirically, observing time-dependence of diffusion in brain tissue has been challenging because this effect occurs at time scales associated with diffusion across length scales featuring neurites (i.e. axons and dendrites). Typically, their diameters as well as the heterogeneities along them (e.g. spines, beads) are of $\sim 1\,\mu$m size, hence, the corresponding diffusion times are expected to be of the order of a few ms. Such short times are quite difficult to access, especially on human systems. Besides, the time-dependence is generally *slow* — which is theoretically expected due to its power-law character [24], as discussed below in Sec. II D — therefore requiring a sufficiently broad range of times to identify.

Time-dependence of the cumulative $D(t)$, Eq. (1.12), in brain tissue has been demonstrated using pulse gradient spin echo (PGSE) in several *ex vivo studies* for a range of diffusion times encompassing $20 - 250$ ms [34, 84–86]. *In vivo*, time-dependent diffusion in both longitudinal and transverse directions was also observed in rat corpus callosum at t ranging from 9 to 24 ms [87], though another study yielded no change in the mean diffusivity of healthy and ischemic feline brain with respect to t between $20 - 2000$ ms [88].

In human brain, it has been unclear for quite some time whether *in vivo* time-dependent diffusion properties can be observed. While several *in vivo* studies report no observable change over a broad range of diffusion times [89, 90], Horsfield *et al.* [91] reported time-dependent diffusion in several white matter regions at times ranging from 40 to 800 ms. Very recently, *in vivo* pronounced time-dependence in the longitudinal diffusivity and less pronounced time-dependence in the transverse diffusivity has been reported in several WM tracts of healthy human volunteers for relatively long diffusion times, $t = 45 - 600$ ms, on a standard clinical scanner using stimulated echo acquisition mode (STEAM)-DTI [25]. Subsequently, a similar effect in the transverse direction to WM tracts was observed with STEAM-DTI in the range $t = 48 - 195$ ms [92] .

Oscillating gradient spin echo (OGSE) diffusion-weighted sequences are able to probe shorter diffusion times compared to conventional PGSE, and have clearly demonstrated time-dependent diffusion in the brain, including the observation of time-dependent diffusivities *in vivo* in normal and ischemic rat brain cortex [93], as well as *ex vivo* in rat WM tracts [94]. By combining OGSE and PGSE, Pyatigorskaya *et al.* [95] observed time-dependent diffusion coefficient and a non-monotonic time-dependent kurtosis (with a maximum value $K \approx 0.6$ at $t \approx 10$ ms) in healthy rat brain cortex at 17.2 T, and Wu and Zhang [96, 97] recently observed time-dependence in mouse cortex and hippocampus. In humans, Baron and Beaulieu [98] found eight major WM tracts and two deep gray matter areas to exhibit time-dependent diffusion using OGSE and PGSE, and Van *et al.* [99] reported a similar effect with OGSE in human corpus callosum. Furthermore, works using double diffusion encoding (cf. Section IV) indirectly point at the possibly non-Gaussian (time-dependent) nature of diffusion in brain tissue.

Overall, while it is common to assume that diffusivities are approximately diffusion time-independent for $t \gtrsim 10$ ms, the experimental data described above clearly demonstrates time-dependent diffusion both at short and long times. In what follows, we describe the underlying theory for both limits and discuss the corresponding biophysical interpretation and potential for clinical applications.

B. Oscillating vs pulsed gradients

Employing OGSE methods, pioneered by Tanner as early as in 1979 [100], is useful for accessing short diffusion times, since the diffusion weighting accumulates over N oscillation periods, $b = Nb_1$ [93, 101]. In this way, the (short) diffusion time $\sim 2\pi/\omega$ gets decoupled from the (long) duration $T = N \cdot 2\pi/\omega$ of the total gradient train. It can be shown [18, 101], that in the limit of large number $N \gg 1$ of oscillations, OGSE measures the real part $\mathrm{Re}\,\mathcal{D}(\omega)$ of the dispersive diffusivity

$$\mathcal{D}(\omega) = \int_0^\infty \mathrm{d}t\, e^{i\omega t}\, \langle v(t)v(0)\rangle \tag{2.1}$$

defined as a Fourier transform of the retarded velocity autocorrelation function [18, 101]

$$\mathcal{D}(t) \equiv \theta(t)\, \langle v(t)v(0)\rangle, \tag{2.2}$$

where $\theta(t)$ is the unit step function, cf. Sec. I D.

The dispersive diffusivity (2.1), the cumulative (1.12), and the instantaneous (1.2) diffusion coefficients, are related to each other via non-local transformations[8] [12, 18, 101]:

$$D_{\mathrm{inst}}(t) = \frac{\partial}{\partial t}\left[tD(t)\right], \tag{2.3}$$

$$D_{\mathrm{inst}}(t) = \int \frac{\mathrm{d}\omega}{2\pi}\, e^{-i\omega t}\, \frac{\mathcal{D}(\omega)}{-i(\omega + i0)}, \tag{2.4}$$

$$D(t) = \frac{1}{t}\int \frac{\mathrm{d}\omega}{2\pi}\, e^{-i\omega t}\, \frac{\mathcal{D}(\omega)}{[-i(\omega + i0)]^2}, \tag{2.5}$$

$$\mathcal{D}(t) = \frac{\partial}{\partial t} D_{\mathrm{inst}}(t) = \frac{\partial^2}{\partial t^2}\left[tD(t)\right]. \tag{2.6}$$

These quantities carry exactly the same information content. However, the practical feasibility of their measurement may differ greatly. Generally speaking, long times are

[8] Causality is maintained since $\mathcal{D}(\omega)$ has no singularities in the upper half-plane of the complex ω, and $\omega + i0$ symbolizes drawing the integration contour along the real axis just above the $\omega = 0$ singularity. For $t < 0$, the integration contour can be closed in the upper half-plane according to the Jordan's lemma, without encountering singularities, leading to $D_{\mathrm{inst}}(t)|_{t<0} = D(t)|_{t<0} = \mathcal{D}(t)|_{t<0} \equiv 0$, cf. Appendix D of ref. [18].

best accessible using PGSE or STEAM-based methods, while short times are best measured in the frequency domain using OGSE.

In order to compare diffusion acquisition methods, an obvious practical question arises: What is the diffusion time in terms of the OGSE frequency (and vice-versa)? How can we plot results of both types of measurements in the same axes?

Unfortunately, in the view of relations (2.4) – (2.5), there is no universal answer to the above question. The relation between $D(t)$ and $D_{\rm inst}(t)$ on the one hand and $\mathcal{D}(\omega)$ on the other is mediated by the Fourier transformation, which is *non-local* in ω. In other words, the conversion between ω and t depends on the *functional form* of either diffusivity and thus requires *understanding the physics of the system*. Without such understanding, we are limited to relations between macroscopic properties, such as $\mathcal{D}(\omega)|_{\omega\to 0} = D(t)|_{t\to\infty} \equiv D_\infty$.

Below, as we describe different models, we will demonstrate examples of such conversion for different functional forms of $\mathcal{D}(\omega)$ and $D(t)$, e.g. Eqs. (2.9) and (2.24).

C. The short-time limit, regime (i): Net surface area of restrictions

1. *Theory*

Observation of the well-known Mitra *et al.* limit [23],

$$D(t) = D_0\left(1 - \frac{4}{3\sqrt{\pi}\,d}\frac{S}{V}\sqrt{D_0 t} + \mathcal{O}(t)\right), \qquad (2.7)$$

where S/V is the surface-to-volume ratio of the restrictions in d spatial dimensions, practically involves very short diffusion times. Even for a red blood cell suspension, such limit was barely observable in the time domain [102]; for the brain, with structural features even smaller than the red blood cell size, getting to this limit using PGSE is practically impossible due to very low b-values for short t.

Hence, regime **(i)** is best accessed using OGSE. The corresponding functional form of $\mathcal{D}(\omega)$ for Eq. (2.7) was recently derived in the $N\to\infty$ limit [101]

$$\mathcal{D}(\omega) \simeq D_0\left(1 - \frac{1}{d\sqrt{2}}\frac{S}{V}\sqrt{\frac{D_0}{\omega}}\right). \qquad (2.8)$$

For a finite total number N of oscillations, Eq. (2.8) is modified by a correction factor $c(N)$ in front of the $1/\sqrt{\omega}$ term, derived by Sukstanskii [103] for the cos gradient waveform; this factor approaches its ideal limit $c(\infty) = 1$ rather fast, as $\sim N^{-3/2}$, and becomes practically important when $N \lesssim 4$.[9]

From directly comparing Eqs. (2.7) and (2.8), the relation between OGSE frequency $\nu = \omega/2\pi$ and diffusion time $t = \Delta$ (in the narrow-pulse PGSE limit) is as follows [101]:

$$\text{regime (i):}\quad t = \frac{9}{64}\cdot\frac{1}{\nu}\,. \qquad (2.9)$$

We note that Eq. (2.9) differs from the empirical relation (see e.g. ref. [93])

$$\text{wrong yet widely used:}\quad t = \frac{1}{4\nu}\,, \qquad (2.10)$$

which in fact is almost always incorrect. Relation (2.10) originates from matching the b-value between one OGSE period and PGSE of the same duration. Since the whole notion of the b-value stems from Gaussian (i.e. time-independent) diffusion, it is not surprising that matching the diffusion attenuation between PGSE and OGSE for the constant D cannot tell anything about the nontrivial, time-dependent case.[10]

2. *Applications*

Probing the short-time limit either in the time domain (Eq. (2.7)) or the frequency domain (Eq. (2.8)) potentially allows for decoupling the geometric effects of the surface-to-volume ratio S/V and the free diffusivity D_0. Recently this limit has been demonstrated in phantoms using both PGSE [104] as well as OGSE [105]. For *in vivo* brain measurement, OGSE provides the most practically feasible method, with the $1/\sqrt{\omega}$ dependency as the signature functional form (2.8) of this regime. In the healthy brain, this signature has so far never been observed, since presumably the achievable oscillation frequencies are still too low as compared to those needed to identify the effect of the restrictions from neurite walls with typical curvature radius of $\sim 1\,\mu$m, requiring diffusion times much below 1 ms (i.e. frequencies $\nu \gg 1$ kHz).

The search for the $1/\sqrt{\omega}$ regime has prompted using brain tumors with roughly spherical cells of larger size (about $10\,\mu$m), such that the required frequency range can be potentially accessible. Recently, the $1/\sqrt{\omega}$ functional form was observed by Reynaud *et al.* [106] in the mouse glioma model in the frequency range up to $\omega/2\pi = 225$ Hz, which for the first time enabled the separation between the geometric (S/V) and "pure" diffusive (D_0) tumor features. Further combining the OGSE and PGSE methods has lead to the POMACE method for quantifying cell size and extra-cellular water fraction [107].

[9] Gradients that are not purely cos-type involve the low-frequency term $\mathcal{D}(\omega/N)$, corresponding to frequencies $\sim 1/T$. Ref. [103] claims that "the high-frequency regime can be achieved only when the *total* diffusion time is smaller than the characteristic diffusion time"; this then leads to $c(N)$ diverging as $\sqrt{N}$, due to applying Eq. (2.8) for $\omega \to \omega/N$. The factor $c(N)$ that approaches 1 with an increasing N can be calculated for any OGSE wave form when the total train duration T falls out of the Mitra *et al.* limit, and the spurious problem quoted in ref. [103] does not arise.

[10] The often quoted relation $t = \Delta - \delta/3$ for the diffusion time of a finite-width PGSE is a myth for the same reasons. One can only say that the measurement gives $D(t)$ with $t \approx \Delta$ (with the precision of this approximation controlled by δ). More rigorously, the effect of finite pulse width δ creates a low-pass filter [10, 12] on $\mathcal{D}(\omega)$, whose effect is again model-dependent, see e.g. Eq. (24) in ref. [14], as well as refs. [15–17], for examples of this filter effect on the particular models of $\mathcal{D}(\omega)$.

D. Approaching the long time limit, regime (ii): Structural correlations via gradual coarse-graining

1. *Theory*

Over time, the random walkers probe the spatial organization of the sample's microstructure, which makes the time-dependence of the diffusion metrics intricately tied to an increasingly large number of structural characteristics. Technically, finding $D(t)$ or $\mathcal{D}(\omega)$ analytically in a realistic complex sample is nearly impossible as it amounts to including the contributions from the spatial correlations of the local diffusion coefficient $D(\mathbf{r})$ and of the positions of all restrictions up to an infinitely high order.

The intuition based on coarse-graining, Sec. I C, turns out to be crucial in solving this challenging problem in the long time regime [24], when the diffusion coefficient (1.2) gradually approaches its macroscopic (tortuosity) value

$$D_\infty \equiv D_{\rm inst}(t)|_{t\to\infty} = D(t)|_{t\to\infty} = \mathcal{D}(\omega)|_{\omega\to 0}\,. \quad (2.11)$$

As mentioned in Sec. I C, at $t\to\infty$, a sample (consisting of a single non-exchanging compartment or multiple exchanging compartments) effectively looks completely uniform.

Let us step back just a bit from $t\to\infty$ and consider sufficiently long, but not infinitely long t. At this point, the sample looks almost homogeneous from the point of the diffusing molecules, Fig. 2, — no matter how heterogeneous it is in reality (i.e. at the cellular scale). In this limit, the problem of finding the diffusion propagator maps onto a much simpler problem, of finding the diffusion propagator in a *weakly heterogeneous* medium (which is the corresponding effective theory), characterized by the diffusion equation (1.4) with

$$\frac{|\delta D(\mathbf{r})|}{D_\infty} \ll 1\,, \quad \delta D(\mathbf{r}) \equiv D(\mathbf{r}) - D_\infty\,. \quad (2.12)$$

This problem admits a perturbative solution [18, 24], with Eq. (2.12) defining a small parameter, as long as the macroscopic (tortuosity) limit (2.11) exists, $D_\infty > 0$ (i.e. diffusion is not anomalous, which is practically always the case for dMRI in tissues, cf. Sec. II). The lowest order in $\delta D(\mathbf{r})$ vanishes, and the second order in the parameter (2.12) yields

$$D_{\rm inst}(t) \simeq D_\infty + \frac{1}{d}\frac{\langle(\delta D(\mathbf{r}))^2\rangle|_{L(t)}}{D_\infty} \quad (2.13)$$

in d spatial dimensions.

The last term in Eq. (2.13) involves the variance of the slowly-varying $D(\mathbf{r})$ *at a given coarse-graining length scale* defined as the diffusion length $L(t)$. This variance *decreases* as a result of *self-averaging*, i.e. when different diffusing molecules on average begin to experience more and more similar mesoscopic structure with an increasing $L(t)$, such that any sample begins to approximate the ensemble of different disorder realizations of $D(\mathbf{r})$ more and more precisely. The always positive "fluctuation correction" to D_∞ (the last term) elucidates why the diffusion coefficient can only decrease with t; observation of its increase with diffusion time is a red flag for imaging artifacts.

To be more rigorous, Eq. (2.13) can be expressed as [24]

$$D_{\rm inst}(t)|_{t\gtrsim t_0} \simeq D_\infty + \frac{1}{D_\infty\, d}\int\frac{\mathrm{d}^d\mathbf{k}}{(2\pi)^d}\,\Gamma_D(\mathbf{k})\,e^{-D_\infty k^2 t}\,, \quad (2.14)$$

in terms of the power spectrum $\Gamma_D(\mathbf{k}) = \int\mathrm{d}\mathbf{r}\,e^{-i\mathbf{k}\mathbf{r}}\,\Gamma_D(\mathbf{r})$ of the underlying effective $D(\mathbf{r})|_{L(t_0)}$ coarse-grained over the diffusion length $L(t_0)$ corresponding to some sufficiently long time scale t_0, for which the relative deviation (2.12) from D_∞ is sufficiently small. The correlation function

$$\Gamma_D(\mathbf{r}) = \langle\delta D(\mathbf{r}+\mathbf{r}_0)\delta D(\mathbf{r}_0)\rangle_{\mathbf{r}_0} \quad (2.15)$$

embodies the fluctuation correction in Eq. (2.13). We can see that diffusion indeed acts as a Gaussian filter (cf. Fig. 2 in Sec. I C), with a filter width $\sim L(t) \sim \sqrt{D_\infty t}$, over the effective medium defined via the weakly heterogeneous $D(\mathbf{r})$.

Hence, starting at sufficiently long t, Eqs. (2.13) and (2.14) become *asymptotically exact* with $L(t)\to\infty$, no matter how strongly heterogeneous the "true" (microscopic) $D(\mathbf{r})$. From the renormalization group flow standpoint, we can say that the time-dependent corrections to the asymptotically Gaussian propagator (last terms of Eqs. (2.13) and (2.14)) become *irrelevant* while integrating out the fluctuations of the locally varying $D(\mathbf{r})$ over larger and larger scales. Likewise, the kurtosis and higher-order cumulants in this compartment will decay to zero, as governed by similar fluctuation terms.

How to relate the time-dependence (2.13) and (2.14) to the mesoscopic structure? Here one realizes that the coarse-grained $D(\mathbf{r})|_{L(t)}$ depends on the similarly coarse-grained local density $n(\mathbf{r})|_{L(t)}$ of mesoscopic restrictions to diffusion (e.g. the disks in Fig. 2). Hence, the variance of $D(\mathbf{r})|_{L(t)}$ entering Eq. (2.13) is proportional to a typical density fluctuation $\langle(\delta n)^2\rangle|_{L(t)}$ of the restrictions in a volume of size $L^d(t)$ in d dimensions (this becomes valid when the deviations $\delta n(\mathbf{r})|_{L(t)} = n(\mathbf{r})|_{L(t)} - \langle n\rangle$ from the mean sample density $\langle n\rangle$ become small). This proportionality, asymptotically exact at small k (i.e. after coarse-graining over large distances), can be formally expressed as the relation

$$\Gamma_D(k) \propto \Gamma(k) \sim k^p\,, \quad k\to 0 \quad (2.16)$$

between the correlation functions (power spectra) of $D(\mathbf{r})$ and of the underlying structure $n(\mathbf{r})$,

$$\Gamma(\mathbf{r}) = \langle n(\mathbf{r}+\mathbf{r}_0)n(\mathbf{r}_0)\rangle_{\mathbf{r}_0}\,. \quad (2.17)$$

The *structural exponent* p in Eq. (2.16) defines the *structural universality class* to which a sample belongs, according to its large-scale structural fluctuations embodied in its correlation function (2.17). The greater the exponent p, the more suppressed are the structural fluctuations at large distances (low k); conversely, negative p signify strong disorder, where the fluctuations are stronger than Poissonian (for which $p=0$). Hence, p characterizes global structural complexity, taking discrete values robust to local perturbations. This enables the classification of the mesoscopic disorder [24], and its relation to the Brownian dynamics, as we now explain.

From Eq. (2.14) it directly follows that the time-dependent instantaneous diffusion coefficient (1.2) approaches the finite bulk diffusion constant D_∞ as a *power law*

$$D_{\rm inst}(t) \simeq D_\infty + {\rm const}\cdot t^{-\vartheta}\,, \quad \vartheta > 0\,, \tag{2.18}$$

with the *dynamical exponent* [24]:

$$\vartheta = (p+d)/2 \tag{2.19}$$

related to the statistics of large scale structural fluctuations via the structural exponent p, and to the spatial dimensionality d.

To illustrate the above general relations, consider Poissonian disorder (uncorrelated restrictions, e.g. completely randomly placed disks in Fig. 2). Their density fluctuation within the "diffusion volume" L^d scales as the inverse volume, $\langle(\delta n(\mathbf{r}))^2\rangle \sim 1/L^d(t) \sim t^{-d/2}$ according to the central limit theorem. Equivalently, $\Gamma(k) \to {\rm const} \sim k^0$ as $k \to 0$, i.e. exponent $p = 0$. As a result, when restrictions are uncorrelated (or, more generally, *short-range disordered*, i.e. have finite correlation length in their placement), the instantaneous diffusion coefficient approaches its macroscopic limit as

$$D_{\rm inst}(t) \simeq D_\infty + {\rm const}\cdot t^{-d/2} \tag{2.20}$$

in d dimensions. This is the intuitive picture behind the formal results [108, 109].

The approach described in [24] generalizes this picture onto any universality class of structural disorder and enables identifying relevant structural fluctuations by measuring the dynamical exponent (2.19). This exponent manifests itself in the power law tail of the molecular velocity autocorrelation function (2.2)

$$\mathcal{D}(t) \sim t^{-(1+\vartheta)} \tag{2.21}$$

and in the dispersive diffusivity[11]

$$\mathcal{D}(\omega) \simeq D_\infty + {\rm const}\cdot (i\omega)^\vartheta \tag{2.22}$$

whose real part is accessible with OGSE [18].

Relation (2.19) provides a way to determine the exponent p (or the effective dimensionality d) and, thereby, the structural universality class, using any type of macroscopic time-dependent diffusion measurement. Local properties affect the non-universal coefficients, e.g. the values of D_∞ and the prefactor of $t^{-\vartheta}$ in Eq. (2.18), but not the exponent ϑ. The latter exponent is *universal*, i.e. is independent of microscopic details, and is robust with respect to variations between samples of a similar origin. From the point of dMRI in biological tissues, the *exponent (2.19) is robust with respect to biological variability*.

We can also see that the stronger the fluctuations (the smaller the exponent p), the smaller is the dynamical exponent ϑ, i.e. the slower the approach to D_∞. Physically, this happens because it takes longer for the coarse-graining to self-average the sample's structural fluctuations. Conversely, if a sample is regular (a periodic lattice, $p \to \infty$), the approach of D_∞ will happen exponentially fast (i.e. faster than any finite inverse power law) [24].

The above approach exemplifies the power of effective theory way of thinking, where to make fairly general statements about the relation between the diffusive dynamics and the structural disorder, we did not have to solve the full nonperturbative problem (starting from the microscopic restrictions $n(\mathbf{r})$), and ended up solving a relatively simple problem of finding lowest-order corrections [18, 24] to the Gaussian diffusion in a weakly heterogeneous medium.

Finally, we address the question formulated at the end of Sec. II B: What is the relation between PGSE diffusion time and OGSE frequency $\omega = 2\pi\nu$? Application of Eq. (2.5) to Eqs. (2.18) and (2.22), and subsequent contour integration in the complex plane of ω leads to

$$t^{-\vartheta} \longleftrightarrow \frac{\pi}{2}\cdot\frac{1-\vartheta}{\Gamma(\vartheta)\,\sin\frac{\pi\vartheta}{2}}\cdot\omega^{\vartheta}\,, \quad \vartheta < 1 \tag{2.23}$$

(here $\Gamma(\vartheta)$ is Euler's Γ-function), yielding

$$\text{regime \textbf{(ii)}:}\quad t = \left[\frac{2\Gamma(\vartheta)\sin\frac{\pi\vartheta}{2}}{\pi(1-\vartheta)}\right]^{1/\vartheta}\cdot\frac{1}{2\pi\nu}\,, \quad \vartheta < 1 \tag{2.24}$$

(cf. also ref. [24], compare Supplementary Eqs. [S17] and [S18].) The relation (2.24) does not look obvious to us; neither it has anything to do with the empirical Eq. (2.10). For example, for $\vartheta = 1/2$ (random permeable barrier model [29] or short-range disorder in $d = 1$ relevant for the neurites, Sec. II D 2 below), we obtain $t = (4/\pi^2)/\nu$.

Note that the above "conversion" between PGSE and OGSE works only for $\vartheta < 1$, since for $\vartheta \geq 1$, the PGSE $D(t)$ expansion at long t will begin with the $1/t$ term, due to the integral in the relation

$$D(t) = \frac{1}{t}\int_0^t {\rm d}\tau\, D_{\rm inst}(\tau) \tag{2.25}$$

converging at short t for the $t^{-\vartheta}$ term in $D_{\rm inst}(t)$. Therefore, the structure-specific dynamical exponent (2.19) is masked in PGSE if it exceeds unity; to reveal it, one has to use $D_{\rm inst}(t)$ which amounts to differentiating noisy experimental data [24]. The borderline case $\vartheta = 1$ has been considered in detail in ref. [14]; the PGSE diffusion coefficient has a $(\ln t)/t$ tail due to the logarithmically divergent integral in Eq. (2.25),

$$D(t) \simeq D_\infty + A\cdot\frac{\ln(t/\tilde{t}_c)}{t}\,, \quad t \gg \tilde{t}_c \sim \max\{t_c,\,\delta\}\,, \tag{2.26}$$

whereas the OGSE counterpart is given by

$$\mathrm{Re}\,\mathcal{D}(\omega) \simeq D_\infty + A\cdot\frac{\pi}{2}|\omega|\,, \quad |\omega| t_c \ll 1\,. \tag{2.27}$$

Here $t_c \sim l_c^2/D_\infty$ is the time to diffuse across the correlation length of the corresponding disordered environment (e.g.

[11] The dispersive terms reads $i\omega\ln(-i\omega)$ for $\vartheta = 1$, hence $\mathrm{Re}\,\mathcal{D}(\omega)$ will depend on ω as $|\omega|$, cf. ref. [14].

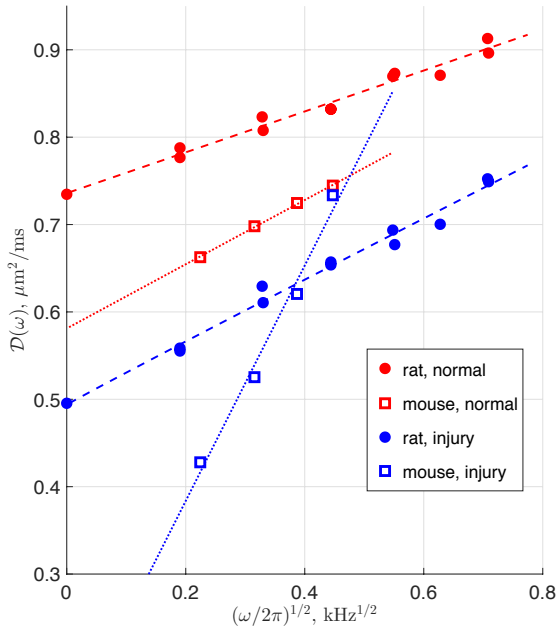

FIG. 6. OGSE measurements in cortical GM: circles are data from average of 5 rats [93] and squares from 6 neonatal mice at 24 hours after unilateral hypoxic ischemic injury [96]. Red: normal rat brain and contralateral side of mouse brain. Blue: globally ischemic rat and ipsilateral side of hypoxia-ischemia injured mouse brain. PGSE data not shown. Dashed lines are fits from Fig. 4 of ref. [24], dotted lines are $\omega^{1/2}$ fits (shown as guide to the eye; power-law exponent fit for mouse data was not robust due to narrow frequency range). Note that while the absolute $\mathcal{D}(\omega)$ values differ between rat and mouse, the general features are similar: data is well described with $\omega^{1/2}$ behavior for normal and ischemic GM (except, possibly, the ischemic mouse, where major structural changes may have occurred in 24h); and the coefficient in front of $\sqrt{\omega}$ (the slope) increases in ischemia, consistent with short-range structural disorder increase along the neurites (e.g. due to beading).

correlation length of the disordered axonal packing [14] in the case $p = 0$ and $d = 2$ considered below in Sec. II D 2). When pulse duration δ exceeds t_c, it starts to play the role of the cutoff time for the power-law tail [14, 15, 17].

2. *Applications*

Probing the diffusivity time-dependence at long times potentially allows for classifying the disorder universality class [24] of the mesoscopic structure, and for extracting the corresponding length scale for the mesoscopic restrictions.

The exponent (2.19) corresponding to the short-time disorder, $p = 0$, has been demonstrated in $d = 2$ dimensions in an anisotropic fiber phantom mimicking the extra-axonal space [14] ($\vartheta = 1$, leading to the $\ln t$ singularity in the PGSE $D(t)$, Eq. (2.26)), as well as recently in a $d = 1$-dimensional phantom [104] for which $\vartheta = 1/2$ for $p = 0$ and $\vartheta = 3/2$ for the hyperuniform placement of permeable membranes ($p = 2$).

Cortical GM was probed with OGSE in rat [93] and mouse [96, 97], Fig. 6. It was suggested [24], that the apparent ω^ϑ behavior with $\vartheta = 1/2$ can be rationalized via the dominance of the effectively $d = 1$-dimensional diffusion along the narrow neurites (dendrites in GM) with the short-range disorder (e.g. spines, beads, varicosities) along them [110–112]. The varicosities are known [113, 114] to become more pronounced in ischemia, which is consistent with the increase in the structural disorder-induced coefficient in front of the ω-dependent term in Eq. (2.22). The power law exponent $\vartheta = 1/2$ also indirectly validates the effectively 1-dimensional diffusion along the so-called "sticks", cf. Sec. III A below.

Human WM was probed *in vivo* in both the longitudinal [25] and transverse directions [25, 92]. The time-dependence of longitudinal diffusivity suggests restrictions are present along axons, which, similar to the GM case above, augments the commonly used "hollow tube" model for diffusion inside and outside neurites (cf. Sec. III A). The "hollow tube" filled with some effective Gaussian medium with diffusion coefficient D_∞ becomes an effective theory technically valid only in the $t \to \infty$ regime **(iii)**; for finite t, the non-Gaussian effects (time-dependent $D(t)$ and the higher-order cumulants) will be present.

Recent quantitative analysis [25] based on Eq. (2.18) for $d = 1$, revealed that this time-dependence is compatible with short-range disorder in placement of restrictions along axons. Intriguingly, the corresponding correlation lengths of about $3-7\,\mu$m are similar to those reported in the literature for varicosities along axons [110–112], suggesting them as potential sources for the reduction of the longitudinal diffusivity with time. Varicosities are often found to be rich in mitochondria and therefore could form obstacles for the diffusion along the fibers, or they could act as temporary traps for the longitudinal diffusion. Additional potential sources for the short range disorder could be axonal undulations [115], or the functional gap junctions unevenly spaced between 20 and 60 μm along the myelin sheath in sciatic nerve [116].

Feasibility of axonal diameter mapping. Previous generation of WM models (CHARMED [35], AxCaliber [36], ActiveAx [37]) neglected coarse-graining in the extra-axonal space and attributed all the observed time dependence to that inside impermeable cylinders mimicking axons. This gave rise to the axonal diameter mapping (ADM) methodology.

Large overestimation of axonal diameters, by factors 3-15, highlighted e.g. in refs. [37, 117], provoked a debate [118, 119] about the feasibility of the method. It has been recognized that the method may fail due to two issues.

The first issue is the smallness of the signal attenuation, which is described in the ADM using the exact solution for the cylinder in the Neuman's regime $\delta \gg r^2/D_0$ [13, 14]

$$-\ln\frac{S}{S_0} \simeq \frac{7}{48}\frac{g^2 r^4 \delta}{D_0} \approx 4.3\cdot 10^{-6} \qquad (2.28)$$

for typical values of Larmor frequency gradient $g = 0.0107\,(\mu\text{m}\cdot\text{ms})^{-1}$ corresponding to 40 mT/m; free axo-

plasmic[12] $D_0 = 2.4\,\mu\mathrm{m}^2/\mathrm{ms}$; pulse duration $\delta = 10\,\mathrm{ms}$, and a typical inner diameter $2r = 1\,\mu\mathrm{m}$ [70–72].[13] Eq. (2.28) is a practical limit of the full $\mathcal{O}(g^2)$ solution [88] of signal attenuation in the Gaussian phase approximation. When $\delta \gg r^2/D_0$, the dependence on Δ drops out, hence the diffusion time is not actually being used to "probe" the cylinder diameter.

The second issue is potentially more significant. Had the above smallness been the only problem, we would just not see any dependencies of intra-axonal signal on experimental parameters. Yet the fits of ADM model to data do show definitive trends in the estimated "apparent diameters" — for instance, with the gradient strength [117] — suggesting some unaccounted physical phenomenon. This has prompted taking into account the coarse-graining *outside* [14] randomly packed axons. The $(\ln t)/t$ term (2.26) from the extra-axonal space appears to completely overwhelm the weak attenuation (2.28) in simulations [14] and in the recent $D(t)$ measurements transverse to human WM fiber tracts [25, 92]. This reveals an exciting unexpected *mesoscopic effect:* The structural disorder in axonal packing within a WM fiber completely changes the interpretation of ADM. Furthermore, recently observed logarithmic dependence on the pulse duration δ in human WM [16], cf. Eq. (2.26), and validated in a fiber phantom [17], adds extra credibility to the mesoscopic extra-axonal origin of the "apparent" ADM effects.

The decreasing apparent diameter trend with increasing gradient strength [117] is consistent with eventual suppression, as $\sim e^{-b(D_\infty + A\ln t/t)}$, of the extra-axonal contribution; however, since $D_\infty \lesssim 0.5\,\mu\mathrm{m}^2/\mathrm{ms}$ (cf. Section III), very large b-values are needed to fully suppress this effect [123].

We note that an even stronger dominance of the extra-axonal contribution occurs in the OGSE domain, since the fully confined water (within an impermeable cylinder transverse to its axis) yields a regular, ω^2 contribution [10, 14, 124, 125] to $\mathrm{Re}\,\mathcal{D}(\omega)$ (observed by Stepisnik *et al.* [126] in porous media), whereas the extra-axonal water would contribute *linearly*, as $|\omega|$, cf. Eq. (2.22) with $\vartheta = 1$. The linear term will dominate at low ω, in agreement with the linear dispersion observed transverse to fibers with OGSE by Portnoy *et al.* [127] and analyzed in ref. [14]. This means, somewhat counterintuitively, that using OGSE is not optimal for probing axonal diameters (but perfect for probing the extra-axonal space geometry!). We warn here that the gradient waveform optimization which does not take into account the mesoscopic effects in the extra-axonal space leads to the opposite conclusion [128].

Overall, the above mesoscopic effects, measured *in vivo* on both animal and human scanners, may enable a novel kind of structural contrast at the micrometer scale (e.g. axonal loss and demyelination), and open up exciting possibilities of monitoring subtle changes of structural arrangements within GM and neuronal tracts in disease, aging, and development.

E. Mesoscopic fluctuations

When ADM is feasible (e.g. spinal cord, due to much larger r), Neuman's r^4 scaling (2.28), together with volume-weighting $\sim r^2$, gives a large weight to a small number of axons with largest diameters, effectively measuring [14]

$$r_{\mathrm{Neuman}} = \left(\overline{r^6}/\overline{r^2}\right)^{1/4}, \tag{2.29}$$

where the averages are taken over the voxel-wise axonal distribution. Hence, when feasible, the metric (2.29) is susceptible to the *mesoscopic fluctuations* governed by the tail of the distribution. This general phenomenon of rare structural configurations determining the measurement outcome has parallels with similar effects found in hopping conduction in disordered semiconductors, kinetics of reaction-diffusion systems, and other phenomena in disordered media [80, 129, 130]. In our case, an accidentally large number of thicker axons, or even a few very thick axons, may significantly skew the intra-axonal attenuation for a particular voxel. This could lead to strongly enhanced variations (relative to those expected based on the measurement noise alone) in the corresponding parametric maps.

The issue of the mesoscopic flucutations is fundamental, and the separation of the effects of biological variabiilty from the random measurement outcomes due to the thermal noise requires model-independent ways of estimating local noise level [131, 132], as well as precisely quantifying the tails of the corresponding distributions of biophysical tissue parameters (e.g. of the axonal diameter distribution [70–72]).

III. THE $t \to \infty$ LIMIT, REGIME (III): MULTIPLE GAUSSIAN COMPARTMENTS

All science is either physics or stamp collecting

Ernest Rutherford

The famously flamboyant century-old quote of a founder of the atomic age could be excusable, as scientific disciplines other than physics in his days were mostly collecting empirical information. Today, Rutherford's quote could as well sound "All science is either physics or fitting". While the purpose of physics remains to identify relevant parameters and to produce an appropriate effective theory (*a model*), the complexity of models and the data abundance has turned *parameter estimation* into a field on its own, if not into a multitude

[12] This value is based on the observation [120] that axoplasmic diffusion coefficient in squid giant axon is 20% below the water diffusion coefficient at the same temperature, and is consistent with the recent estimate of $D_a \approx 2\,\mu\mathrm{m}^2/\mathrm{ms}$ *along* axons in human WM at $t = 50\,\mathrm{ms}$ [121], which sets the lower bound for D_0. Another large axon study in excised lamprey spinal cord [122] reported a similar deviation of about 25% for the longitudinal diffusion coefficient from the free water diffusion coefficient. Alternatively, using NAA as an intracellular reporter molecule, the ratio for the *in vivo* measured parallel diffusion coefficient in the corpus callosum relative to its diffusion coefficient in dilute aqeous solutions, ranges from 0.4 up to 0.46 [38], corresponding to estimates of water $D_a \sim 1.2 - 1.8\,\mu\mathrm{m}^2/\mathrm{ms}$.

[13] Here we consider brain; axons are about factor of 5 thicker in the spinal cord, and the ADM prospects are much better there [94], due to the r^4 scaling in Eq. (2.28).

of fields, with particular ways of thinking and approaches, known under different names and incorporating advanced modern tools (e.g. compressed sensing [133, 134], fingerprinting [135], and numerous sub-fields of machine learning).

As we will illustrate in this Section, while from the physics standpoint, the dMRI models in the $t \to \infty$ regime become trivial (a sum of Gaussians = exponentials in b), their sheer number of parameters together with low SNR has made parameter estimation extremely challenging. Hence, arguably, most intellectual efforts in the regime **(iii)** (as defined in Sec. I E) has been spent on "fitting" rather than on "physics".

Below, after introducing the *stick* compartment in Sec. III A, we formulate the overarching Standard Model of diffusion in neuronal tissue as a sum of anisotropic Gaussian compartments (Sec. III B, Figs. 4 and 7), and then discuss challenges of its parameter estimation, Sec, III C, focussing on its degeneracies. We subsequently review works involving constraints on SM parameters (Sec. III D), followed by the unconstrained, rotationally-invariant methods (Sec. III E), and conclude this Section with a summary of unresolved problems (Sec. III F).

A. Neurites as "sticks"

1. *Theory and assumptions*

In this Section, we assume that the $t \to \infty$ regime **(iii)** has been practically achieved, and neglect the time-dependent power-law "tails" describing the approach of the diffusion coefficient to its tortuosity limit, discussed in Section II.[14]

Full coarse-graining in the intra-neurite space then leads to the most anisotropic Gaussian compartment possible — the so-called "stick" compartment — first introduced by Kroenke *et al.* [38] and Jespersen *et al.* [39] in 2004–2007. Its main features are:

1. A stick is a cylinder whose radius r is negligible compared with the "free" diffusion length $\sim \sqrt{D_0 t}$ at given t. Equivalently, the transverse diffusion coefficient $D_a^\perp \simeq r^2/4t \sim 0.01\,\mu\mathrm{m}^2/\mathrm{ms}$ for typical $t \sim 100\,\mathrm{ms}$ is negligible compared to $D_0 \approx 2.4\,\mu\mathrm{m}^2/\mathrm{ms}$,[15] and hence can be set to zero, $D_a^\perp \to 0$. In other words, the measurement is insensitive to neurite radii (cf. discussion in Sec. II D 2).

2. The longitudinal diffusion inside a neurite becomes Gaussian, with the macroscopic (tortuosity) asymptote D_a. Of course, D_a, being the effective coarse-grained parameter, can be notably reduced relatively to the intrinsic axoplasmic diffusion coefficient D_0, cf. Section II. The parameter D_a takes into account all restrictions, such as varicosities (beads) and undulations, along the (average) neurite direction. Hence, it can have important biophysical and diagnostic value in the cases when the structure along neurites changes, e.g. in acute stroke [113, 114] and in Alzheimer's disease [136].

3. Exchange between intra- and extra-neurite water can be neglected, at least at the time scales t used in clinical dMRI. Measuring exchange times *in vivo* is very difficult, making this assumption hard to validate. The consensus so far has been that this assumption holds for WM tracts, especially with highly myelinated axons. At which t this assumption might break for dendrites in GM is still unclear. Hence, the model of sticks has been mostly applied to WM, where sticks represent axons (and possibly some glial cell processes). Recent study [137] supports the presence of two compartments in the healthy brain with the exchange time of about a second, which is indeed negligible on the clinical $t \sim 100\,\mathrm{ms}$ time scale.

From the modeling standpoint, the stick compartment is the defining feature of dMRI inherent to the neuronal tissue, as compared to all other kinds of soft tissues. It is chiefly responsible for the anisotropy of the diffusion propagator in the brain and in spinal cord.

The diffusion propagator for a stick pointing in the unit direction $\hat{\mathbf{n}}$, measured in unit gradient direction $\hat{\mathbf{g}}$,

$$G_{\hat{\mathbf{n}}}(\hat{\mathbf{g}}, b) = e^{-bD_a(\hat{\mathbf{g}}\cdot\hat{\mathbf{n}})^2} \tag{3.1}$$

is determined by $\cos\theta \equiv \hat{\mathbf{g}}\cdot\hat{\mathbf{n}}$, where θ is the angle between $\hat{\mathbf{g}}$ and $\hat{\mathbf{n}}$. The signal is not suppressed for $\hat{\mathbf{g}} \perp \hat{\mathbf{n}}$ and decays fast with b when $\hat{\mathbf{g}} \parallel \hat{\mathbf{n}}$. Hence, when $bD_a \gg 1$, the stick dMRI response (3.1) becomes a thin "pancake", non-negligible when $|\hat{\mathbf{n}}\cdot\hat{\mathbf{g}}| \lesssim (bD_a)^{-1/2}$ *nearly transverse to* $\hat{\mathbf{g}}$, whose angular thickness scales as $\delta\theta \sim 1/\sqrt{bD_a}$ [121, 138]. The latter estimate follows from setting the argument of the exponential to unity.

2. *Validation of the picture of sticks*

Reviewing validation studies is beyond the scope of this article. However, given the essential role sticks play in dMRI models, we mention the following two kinds of results.

First, metabolites, such as N-Acetylaspartic acid (NAA), intrinsic to the intra-neurite space, can be used to identiy the stick compartment, as reviewed by Ackerman and Neil [139]. The seminal NAA study was performed by Kroenke, Ackerman and Yablonskiy [38], who demonstrated a very good agreement between dMRI signal from large voxels in rat brain averaged over three gradient orientations, at diffusion times $t = 50 - 100\,\mathrm{ms}$, and the isotropically averaged stick signal,

$$\int \mathrm{d}\hat{\mathbf{n}}\, G_{\hat{\mathbf{n}}}(\hat{\mathbf{g}}, b) = \sqrt{\frac{\pi}{4bD_a}}\,\mathrm{erf}\left(\sqrt{bD_a}\right), \tag{3.2}$$

[14] Mathematically speaking, a power-law approach, being scale-invariant, means that the $t \to \infty$ regime is never fully achieved — there is no time scale that tells us where we can neglect the residual non-Gaussian effects in each compartment. However, practically, their detection limit is set by a finite SNR.

[15] See footnote 12 in Section II

where erf is the error function. Taking a large voxel, which presumably has all neurite orientations, and subsequently averaging over 3 directions, maps the signal to that from a completely random stick arrangement, first considered by Callaghan [32] in 1979, and subsequently by Yablonskiy *et al.* [33] in 2002 for ^{3}He diffusion in the lung, resulting in Eq. (3.2) (Fig. 4). The agreement with the theory (3.2) was very good in the whole range $0 < b \lesssim 20\,\mathrm{ms}/\mu\mathrm{m}^2$ [38]. Recent directional NAA imaging by Ronen *et al.* [140], quantifying the dMRI signal anisotropy, agrees well with the structure tensor [141] derived from the axonal histology in the corpus callosum.

Second, identifying a distinct *functional form* inherent to the stick compartment in the water dMRI data at very large b can also validate the pictures of sticks. In this limit, the extra-neurite signal is exponentially suppressed (since the extra-neurite diffusion coefficient is nonzero in any direction), while the intra-neurite signal is only suppressed as a very slowly decaying power-law $\sim b^{-1/2}$, scaling as the width of the pancake-shaped stick response function (3.1), cf. Eq. (3.2) and refs. [121, 138]. The recently observed [121] universal asymptotic power-law proton signal attenuation in human WM *in vivo*, isotropically averaged over multiple gradient directions $\hat{\mathbf{g}}$,

$$\overline{S}|_{bD_a\gg 1} \simeq \beta\cdot b^{-\alpha} + \gamma\,, \tag{3.3}$$

with exponent $\alpha = 1/2$, provides a "direct" signature of axons as sticks for water dMRI. The isotropic average (cf. Sec. III E 1 below) of the signal makes it equivalent to that from the isotropic set of sticks, cf. Eq. (3.2) above, with erf approaching 1 at large b.

Either detectable axonal diameter values, or a notable exchange rate between intra- and extra-axonal water, would destroy the very particular stick-related $b^{-1/2}$ scaling (3.3). In particular, the analysis in ref. [121] shows that, had the axonal diameters been notably higher than their histological estimates of $\sim 1\,\mu$m [70–72], as the ADM results often show (cf. Sec. II D 2), the power law exponent α would differ from $1/2$. Hence, human dMRI measurements are practically insensitive to axonal diameters even with large gradients employed, further confirming the first stick assumption in Sec. III A. The human measurement [121] also revealed that the immobile water fraction γ, not decaying with b for any direction, is below detection limit. The same conclusion was made independently using isotropic diffusion weighting [142].

B. The Standard Model of diffusion in neuronal tissue

1. *Theory*

With the intra-neurite diffusion modeled as a collection of sticks, and the isotropically fully restricted water out of the picture, how should we model the remaining water? The answer depends on the coarse-graining length scale.

If the diffusion time is truly "infinite", i.e. water molecules can sample *all* the extra-neurite space (ENS) within a voxel, then diffusion in this space should become Gaussian and be described by the overall ENS diffusion tensor, $S_{\mathrm{ENS}} \sim \exp(-b_{ij}D^{\mathrm{ENS}}_{ij})$, where the b-matrix $b_{ij} = q_iq_jt \equiv b\,g_ig_j$ depends on the components of the unit diffusion gradient $\hat{\mathbf{g}}$, cf. Eqs. (1.8) and (1.10). The ENS tensor D^{ENS} would then by definition describe all ENS water, including cerebrospinal fluid (CSF) that could e.g. contribute if a voxel contains part of a ventricle.

Practically, the true $t\to\infty$ limit is never realized for a macroscopic voxel. For typical diffusion times $t = 50 - 100\,$ms, the corresponding diffusion length $L(t) \sim 10\,\mu$m defines the coarse-graining window, where the diffusion properties locally become (almost) Gaussian. At this scale, the neuronal tissue, at least in the WM, looks as a highly aligned fiber segment (fascicle)[16], Fig. 7, the leftmost image. Because the fibers are locally coherent at the scale $L(t)$, the local ENS tensor $D^{\mathrm{ENS}}_{ij}(\mathbf{r})$ can differ at the different positions $\mathbf{r}$ within a voxel if they are separated by distance much exceeding $L(t)$ (for instance, if a voxel contains fiber crossings).[17] This local microscopic anisotropy of ENS suggests that, strictly speaking, the ENS diffusion is never Gaussian — but is rather a sum of local anisotropic Gaussian contributions, which are highly aligned with the corresponding local stick arrangements.

These coarse-graining considerations lead to the general picture of anisotropic Gaussian compartments, Fig. 7, with the intra-neurite space represented as sticks, and the extra-neurite space as the (locally) Gaussian compartment described by a diffusion tensor with principle direction in the stick orientation. The signal measured in the unit direction $\hat{\mathbf{g}}$,

$$S_{\hat{\mathbf{g}}}(b) = S(0)\cdot\int_{|\hat{\mathbf{n}}|=1} \mathrm{d}\hat{\mathbf{n}}\,\mathcal{P}(\hat{\mathbf{n}})\,\mathcal{K}(b,\hat{\mathbf{g}}\cdot\hat{\mathbf{n}}) \tag{3.4}$$

is a convolution (on a unit sphere) between the fiber orientation distribution function (ODF) $\mathcal{P}(\hat{\mathbf{n}})$, and the response

$$\begin{aligned}\mathcal{K}(b,\xi) = f e^{-bD_a\xi^2} + (1-f-f_{\mathrm{CSF}})e^{-bD_e^{\perp}-b(D_e^{\parallel}-D_e^{\perp})\xi^2} \\ + f_{\mathrm{CSF}}\,e^{-bD_{\mathrm{CSF}}}\end{aligned} \tag{3.5}$$

from a perfectly aligned fiber segment (fascicle) pointing in the direction $\hat{\mathbf{n}}$. The kernel (3.5) depends on the relative angle θ, $\cos\theta = \hat{\mathbf{g}}\cdot\hat{\mathbf{n}} \equiv \xi$ (cf. Eq. (3.1) in Sec. III A). It is a sum of the exponential (in b) contributions from intra- and extra-neurite spaces, with T_2-weighted water fractions, and the isotropic CSF compartment with $D_{\mathrm{CSF}} \approx 3\,\mu\mathrm{m}^2/\mathrm{ms}$. Because of the ODF normalization $\int\mathrm{d}\hat{\mathbf{n}}\,\mathcal{P}(\hat{\mathbf{n}}) \equiv 1$, the CSF term can be included in the kernel or added separately to signal (3.4); we choose to include it in the kernel (3.5), as it makes the formulation (3.4) more elegant.

---

[16] cf. footnote 14; effectively, we neglect $D(t) - D_\infty$ within each fascicle.

[17] This picture might be not as definite in GM, where the dendrites are more intertwined, and the concept of the overall ENS tensor may be better justified [39, 40]. But then, much less is known about diffusion in GM overall, and in particular, the residence times in dendrites are not yet well known. Therefore, here we mostly discuss SM in the context of WM, leaving figuring out a model for GM to the reader as a homework exercise.

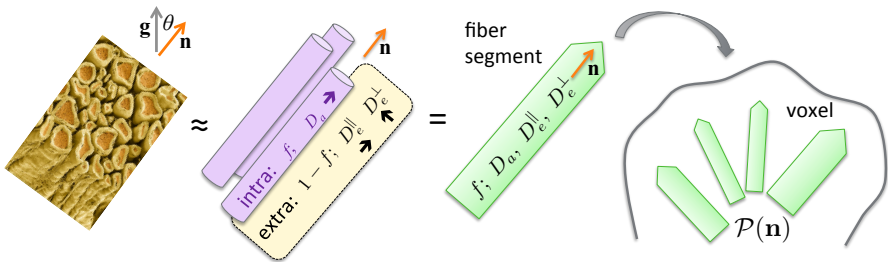

FIG. 7. **The Standard Model of diffusion in neuronal tissue, Eq. (3.4).** In the $t \to \infty$ regime **(iii)**, elementary fiber segments (fascicles), consisting of intra- and extra-neurite compartments, are described by at least 4 independent parameters: f, D_a, $D_e^{\parallel}$ and $D_e^{\perp}$. CSF can be further added as the third compartment, cf. Eq. (3.5). Within a macroscopic voxel, such segments contribute to the directional dMRI signal according to their ODF $\mathcal{P}(\hat{\mathbf{n}})$.

The overarching model (3.4) and (3.5) includes pretty much all previously used models [38–49, 58, 59] (at least in the WM) as particular cases, also described in recent taxonomy studies in refs. [143, 144] where some of the "models" are actually representations, in the sense of Sec. I G. In other words, the numerous abbreviations, corresponding to the right part of Fig. 4 in Section I, *describe the same physics, and hence they are really the same model*.

Because of the overall popularity and inclusiveness of the above picture, here we suggest to call the model (3.4)–(3.5) the Standard Model (SM)[18].

2. *Specificity and relevance of SM parameters*

The first attempt to validate the 2-compartment SM was performed by Jespersen *et al.* [40] using direct fitting to an extensive *ex vivo* data set covering both WM and GM, while parametrizing the ODF using spherical harmonics Y_{lm} up to $l \leq 4$. (The ENS diffusion in this work was described by the overall tensor, whose 6 components were estimated.) Data was acquired on a 16.4 T magnet using 16 shells with $0 \leq b \leq 15\,\mathrm{ms}/\mu\mathrm{m}^2$ and 144 directions, with acquisition taking over 15 hours. The fraction f correlated well with AMG staining for the neurites, and the ODF directionality agreed with the histology. Further quantitative comparison of the predictions to histology was carried out in [145], where the neurite ODF was determined from Golgi stained cortical neurons in immature ferret brains.

Over the past decade, it has become clear that the scalar parameters f, f_{CSF}, D_a, $D_e^{\parallel}$ and $D_e^{\perp}$, and ODF $\mathcal{P}(\hat{\mathbf{n}})$, each carry distinct biophysical significance. Deconvolving the voxel-wise fiber ODF based on the locally estimated kernel (3.5), instead of relying on the empirical directions from the signal (3.4) or on the empirical single-fiber response applied globally [146], provides a more adequate starting point for fiber tractography, an essential tool for mapping structural brain connectivity and for presurgical planning.

[18] The name is suggested by somewhat amusing analogies with the Standard Model in particle physics. In both communities, SM represents the consensus knowledge about the subject, satisfactorily describes almost everything, has been out there for a while, and yet one really hopes that there is exciting physics beyond it — which is far more difficult to access. Our community has a doubtless advantage in that investigations beyond SM are much cheaper (cf. Section II) than building particle accelerators.

Furthermore, as illustrated further in Sec. III D 1, the ability to estimate scalar parameters of the kernel (3.5) would make dMRI measurements *specific* — rather than just sensitive — to μm-level manifestations of disease processes, such as demyelination [147–149] ($D_e^{\perp}$), axonal/dendritic loss [149–152] (f), beading [153], oedema and inflammation (f_{CSF}, D_a and $D_e^{\parallel}$). Combining f with the extra-axonal volume fraction derived either from tortuosity modeling based on $D_e^{\perp}$ [147, 148] or from the myelin volume fraction via relaxometry, would ultimately allow one to determine axonal g-ratio [154]. Since the precise nature and pathological changes in microarchitecture of restrictions leading to the scalar parameter values are unknown, ideally, to become specific to pathology, one needs to estimate f, f_{CSF}, D_a, $D_e^{\parallel}$ and $D_e^{\perp}$ separately.

While "brute-force" fitting of ~ 20 parameters could work for an extensive data set [40], the clinical dMRI data is far noisier, and have much less q-space coverage. Hence, because of high dimensionality of parameter space, parameter estimation for Eqs. (3.4)–(3.5) from realistic noisy data has emerged as an overarching challenge (Sec. III C). SM parameter estimation from clinical acquisitions has until recently reverted to making severe restrictions, as discussed further in Sec. III D, which also explains how previous literature [38–49, 58, 59] differs largely in the ways SM parameters have been constrained.

C. The challenge: SM parameter estimation

1. *SM parameter count*

To quantify the problem's complexity, we find here how many parameters N_p the model (3.4) should have — and, hence, how many we have to estimate from the (noisy) dMRI data.

The answer depends on the maximal power $l_{\max}$ of the diffusion weighting $b^{l_{\max}/2} \sim q^{l_{\max}}$ to which an acquisition is sensitive, at a given SNR. This can be seen either from the cumulant expansion (1.10) of $\ln S_{\hat{\mathbf{g}}}(b)$, or, equivalently [11], from the Taylor expansion of the signal (3.4)

$$\frac{S_{\hat{\mathbf{g}}}(b)}{S(0)} = 1 - bM^{(2)}_{i_1 i_2}\, g_{i_1} g_{i_2} + \frac{b^2}{2!}\, M^{(4)}_{i_1 \ldots i_4}\, g_{i_1} \ldots g_{i_4} - \ldots \tag{3.6}$$

in the fully symmetric moments $M^{(l)}_{i_1 \ldots i_l}$. These moments are proportional to angular averages $\langle n_{i_1} \ldots n_{i_l} \rangle$ over the ODF $\mathcal{P}(\hat{\mathbf{n}})$, as it is evident from expanding the exponential terms

containing $\xi = n_i g_i$ in kernel (3.5), such that subsequent terms have the form $b\langle n_i n_j\rangle g_i g_j$, $b^2\langle n_{i_1}\dots n_{i_4}\rangle g_{i_1}\dots g_{i_4}$, etc. The maximal (even) order l of the product $\langle n_{i_1}\dots n_{i_l}\rangle$ always appears with the corresponding power $b^{l/2}$ of the diffusion weighting [47, 48].

The symmetric tensors $\langle n_{i_1}\dots n_{i_l}\rangle$, after subtracting the reducible parts, can be turned into the corresponding symmetric trace-free tensors (STF) of rank l [68], which are equivalent to the set Y_{lm} of the spherical harmonics (SH) discussed in Sec. I H above. In other words, the ODF averages $\langle n_{i_1}\dots n_{i_l}\rangle$ correspond to the SH coefficients p_{lm} of the ODF,

$$\mathcal{P}(\hat{\mathbf{n}}) \approx 1 + \sum_{l=2,4,\dots}^{l_{\max}} \sum_{m=-l}^{l} p_{lm} Y_{lm}(\hat{\mathbf{n}})\,. \tag{3.7}$$

In particular, the highest-order cumulant $C^{(l_{\max})}$ or the moment $M^{(l_{\max})}$ still practically resolvable from the signal sets the maximal order $l_{\max}$ for the even-order SH expansion (3.7).

Hence, the (minimum) $N_s = 4$ *scalar* parameters from the kernel (3.5) in the absence of CSF (or $N_s = 5$ if the CSF compartment is added), are complemented by the $n_c(l_{\max}) - 1 = l_{\max}(l_{\max}+3)/2$ *tensor* parameters p_{lm}, where $n_c(l)$ is the number of the even-order spherical harmonics coefficients up to the order l given by Eq. (1.14) in Sec. I H, and we subtracted one parameter because $p_{00} \equiv 1$ is set by the ODF normalization. This yields the total SM parameter count [47, 48]

$$N_p(l_{\max}) = N_s + l_{\max}(l_{\max}+3)/2 \tag{3.8}$$

such that $N_p = 9,\ 18,\ 31,\ 48,\ \dots$ for $l_{\max} = 2,\ 4,\ 6,\ 8,\ \dots$ already for the two-compartment kernel (3.5), without including $S(0)$ and f_{CSF} in the count.

Equation (3.8) reveals that the model complexity grows fast, as $l_{\max}^2$, if we are to account for the rich orientational content of the realistic fiber ODFs in the brain. For the achievable $l_{\max} \sim 4-8$, the dMRI signal in principle "contains" a few dozen parameters, none of which are known *a priori*.

We note here that an obvious corollary of the above parameter counting is that oversampling the directions within the low-b shells does not improve angular resolution in estimating $\mathcal{P}(\hat{\mathbf{n}})$ — in other words, optimal q-space coverage should match the sensitivity to the power $b^{l_{\max}/2} \sim q^{l_{\max}}$ of the shell radius with the minimal number $n_c(l_{\max})$ of directions per shell. Naive sampling, say, 256 directions at $b \approx 1\,\mathrm{ms}/\mu\mathrm{m}^2$ would not in principle yield better angular ODF resolution than, say, ~ 10 averages of 25 directions. Indeed, the clinical dMRI signal at this b-value can be fully described using $\mathcal{O}(b)$ (DTI, $l_{\max} = 2$), or, at best, $\mathcal{O}(b^2)$ (DKI, $l_{\max} = 4$) cumulant terms, corresponding to being sensitive to the ODF expansion coefficients p_{lm} up to $l = 2$ or $l = 4$ (containing 5 or 14 parameters). There is no way to determine, say, p_{6m} and beyond, if the diffusion weighting is too weak for the b^3 terms to be discernible at a given SNR.

2. *How many parameters are necessary?*

We can now contrast the SM parameter count (3.8) with the number $N_c(l_{\max})$ [Eq. (1.15) in Sec. I H] of independent parameters "contained" in the cumulant or moment series truncated at $l = l_{\max}$. Since $N_c(l) \sim l^3$ grows faster with l than $N_p(l) \sim l^2$, the moments/cumulants estimated from the signal should, beyond some l, contain more than enough information to determine all the corresponding SM parameters. Direct comparison of Eqs. (1.15) and (3.8) yields that

$$N_c(l_{\max}) > N_p(l_{\max}) \quad \text{for} \quad l_{\max} \geq 4 \tag{3.9}$$

for both 2- and 3-compartmental SM. This naive counting would let one believe that, having mastered sufficiently precise DKI parameter estimation ($l_{\max} = 4$), we would be able to find all the scalar SM parameters, as well as estimate arbitrary fiber ODF up to p_{4m}, Eq. (3.7).

This intuition, however, is deceptive, because it does not account for the nonlinear nature of the mapping between signal and model parameters. It turns out that the minimal order $l_{\max}$ for which the moments/cumulants contain enough information to determine all SM parameters is $l_{\max} = 6$, while at the $l_{\max} = 4$ level, there are at least two continuous "branches", or families, of scalar parameters which *exactly match* the signal's moment tensors $M^{(2)}_{i_1 i_2}$ and $M^{(4)}_{i_1\dots i_4}$ (equivalently, the diffusion and kurtosis tensors) [47, 48]. The two families of solutions ("bi-modality") technically emerge as the two branches of a square root in a solution for a quadratic equation. In what follows, we illustrate this effect with a toy model of parallel fibers [41, 42] and then show that increasing the model complexity does not cure the problem.

3. *A toy model of bi-modality: Parallel fibers*

Let us now see how two branches appear as solutions of a quadratic equation involving directional diffusion and kurtosis values for a very simple ODF of perfectly aligned fibers, for the 2-compartment SM case. Here we follow the cumulant-series DKI approach of Fieremans *et al.* [41, 42]; an equivalent formulation in terms of the moments, cf. Eq. (3.6), can be found in ref. [48]. Similar ideas were subsequently exploited [155] to enable estimation of WMTI metrics with reduced data requirements using axially symmetric DKI [156].

Staying at the $\mathcal{O}(b^2)$ level (DKI), the overall radial and axial components of the diffusion tensor, estimated from an ideally measured signal (the left-hand side), correspond to the following combinations of the scalar parameters (the right-hand side):

$$D^{\perp} = (1-f)D_e^{\perp} \tag{3.10}$$

$$D^{\parallel} = fD_a + (1-f)D_e^{\parallel}\,, \tag{3.11}$$

and for kurtosis components [41, 42]

$$K^{\perp} = \frac{3f}{1-f}\,, \tag{3.12}$$

$$K^{\parallel} = \frac{3f(1-f)(D_a - D_e^{\parallel})^2}{{D^{\parallel}}^2}\,. \tag{3.13}$$

"Transverse" parameters f and $D_e^{\perp}$ are uniquely determined from $K^{\perp}$ and $D^{\perp}$:

$$f = \frac{K^{\perp}}{K^{\perp}+3}\,, \qquad D_e^{\perp} = \left(1 + \frac{K^{\perp}}{3}\right) D^{\perp}\,. \tag{3.14}$$

However, there are *two* possible solutions in the parallel direction. The duality arises from choosing [42, 48] the $\zeta = \pm$ branch of the square root in Eq. (3.13),

$$D_a - D_e^{\parallel} = \zeta \cdot \sqrt{\frac{K^{\parallel}}{3f(1-f)}} \cdot D^{\parallel}\,, \quad \zeta = \pm 1\,. \tag{3.15}$$

Here $\sqrt{K^{\parallel}} \propto |D_a - D_e^{\parallel}| \equiv \eta(D_a - D_e^{\parallel})$, where $\eta = \mathrm{sgn}\,(D_a - D_e^{\parallel})$. Note that, since the ground truth is unknown, our branch choice ζ may differ from the correct sign η.

From Eqs. (3.11) and (3.15), we find that, not surprisingly, the correct choice $\zeta = \eta$ yields the true values D_a and $D_e^{\parallel}$. However, if the sign choice is wrong, $\zeta = -\eta$, then the "apparent" diffusivities do not agree with the true ones:

$$D_a^{\mathrm{app}} = (2f-1)D_a + 2(1-f)D_e^{\parallel}\,, \tag{3.16}$$

$${D_e^{\parallel}}^{\mathrm{app}} = 2fD_a + (1-2f)D_e^{\parallel}\,. \tag{3.17}$$

Note, that in this case, as expected, ${D_e^{\parallel}}^{\mathrm{app}} - {D_a}^{\mathrm{app}} = -(D_e^{\parallel} - D_a)$, i.e. the difference has the same absolute value and the wrong sign. In particular, for $f = 1/2$, the diffusivities are swapped — i.e *we mistake the intra-axonal for the extra-axonal one and vice-versa, which can radically change biophysical and diagnostic implications of the estimated parameters*. Yet the above "apparent" values can seem completely biophysically plausible, especially if $f \approx 0.5$.

From the above derivation it is evident that the bi-modality of the parameter estimation originates from having two tissue compartments, and that the branch choice is certainly not obvious just based on the parameter values estimated at low b.

4. *Bi-modality beyond parallel fibers. Flat directions in the fitting landscape*

The simplest nontrivial model revealing general degeneracies in parameter estimation, NODDIDA [46], is a two-compartment SM variant ($N_s = 4$) that assumes a 1-parameter Watson ODF shape [44] and sets $f_{\mathrm{CSF}} \equiv 0$. In this model, unconstrained nonlinear fitting has revealed two families (trenches) of biophysically plausible solutions to fit optimization already in the relatively small, (4+1)-dimensional, parameter space, and *flat directions* along them [46].

Hence, NODDIDA exemplifies the two-fold nature of the parameter estimation challenge. Beyond the existence of multiple parameter branches (a "discrete" degeneracy, as in the toy model above), each of them represents a shallow "trench" in the nonlinear fitting parameter landscape (a "continous" degeneracy).

The flatness, or continuous degeneracy, can be formulated as having the number of estimated parameters exceeding the number of relations between the parameters obtainable from the data. In its simplest form, this problem exists already for the simplest single-directional fitting with a biexponential function [157]. A normalized biexponential $S = fe^{-bD_1} + (1-f)e^{-bD_2}$ has 3 parameters; however, if b is low enough so that we are practically only sensitive to the terms $\sim b$ and $\sim b^2$ — i.e. when the DKI representation works well — we can only estimate 2 combinations of 3 model parameters, and will have a flat direction in the corresponding 3-dimensional fitting parameter landscape.

The expansion (3.6) of the 2-compartment SM with *any* ODF into moments has been analytically and numerically shown to possess a similar kind of degeneracy. This framework, called LEMONADE (Linearly Estimated Moments provide Orientations of Neurites And their Diffusivities Exactly) [47, 48], exactly relates the moment tensors $M^{(l)}$ to SM parameters. It turns out that, at the $\mathcal{O}(b^2)$ level, there are only 4 independent equations, which relate rotationally invariant combinations of moments $M^{(2)}$ and $M^{(4)}$ to 5 SM parameters — the 4 scalar ones: f, D_a, $D_e^{\parallel}$, $D_e^{\perp}$, and the ODF parameter p_2 (that characterizes its ODF anisotropy, defined in Sec. III E below). Hence, the existence of the flat trenches in nonlinear fitting in NODDIDA is actually completely general; both the discrete bi-modality and the continuous trenches follow from the exact relations [47, 48] between the moments and the SM parameters, and will be present for any fiber ODF. Hence, it is only capturing the moment $M^{(6)}$ that can lift both kinds of degeneracies — as we mentioned briefly after Eq. (3.9) above — which is practically quite difficult to become sensitive to.

As for the "discrete" degeneracy, the works [41, 42, 46–48] have collectively raised the fundamental question: *Which "branch" of parameters should be chosen, out of at least two biophysically plausible ones?* Of course, only one branch corresponds to the truth; other(s) should be discarded. Branch choice is nontrivial, since often times, both parameter sets look equally biophysically plausible [42, 48]. In Sec. III F, we will comment on the branch selection.

D. SM parameter estimation using constrains

Due to the given challenge explained above (Sec. III C) of fitting the SM to noisy dMRI data, especially those acquired in clinical setting, most attempts of SM parameter estimation so far are based on superimposing additional constraints on both the scalar SM parameters, as well as the fiber ODF, in order to improve robustness of the fitted SM parameters.

An overview of employed models used so far is given in Figure 4. In what follows we consider two representative

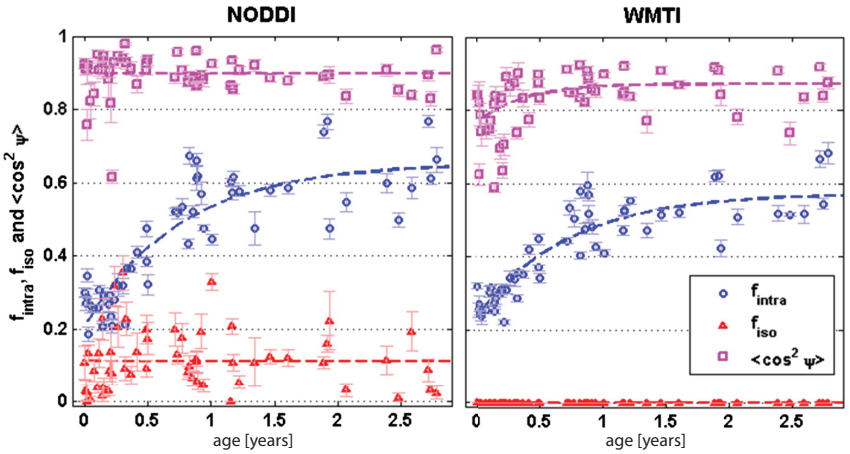

FIG. 8. Comparison of NODDI (Sec. III D 2) and WMTI (Sec. III D 1) parameter evolution with age in human corpus callosum splenium [158]. A qualitatively (but not quantitatively) similar trend of continued increase in the intra-axonal water fraction $f_{\text{intra}} \equiv f$ was observed for both models, consistent with on-going myelination. WMTI displays a trend of increased fiber alignment (expressed by the orientation dispersion $\langle \cos^2 \psi \rangle$), which could be a manifestation of continued pruning in the first year of life, while NODDI does not. The CSF fraction is set, $f_{\text{iso}} \equiv f_{\text{CSF}} = 0$, in WMTI.

modeling approaches that are very popular because of their robustness, which potentially allows for clinical translation, and try to explain the quantitative differences in parameter estimates between them in the light of each model's assumptions and consequent biases.

1. *White Matter Tract Integrity metrics (WMTI)*

WMTI, as proposed by Fieremans *et al.* [41, 42], extracts the 2-compartment SM parameters by relating the DKI components to scalar parameters in the aligned-fiber framework [41], already explained above (Sec. III C 3). Subsequently, the perfectly aligned approximation was somewhat relaxed by allowing for some dispersion within the fiber bundle, and describing the diffusion in the intra-, and extra-axonal space by compartment tensors [42]. While the advantage of using DKI eliminated the need for direct nonlinear fitting to the diffusion signal, two different biophysically plausible solutions still exist in this case, cf. the two branches as described above (Sec. III C 3). In WMTI, the branch was chosen as $D_a < D_e^{\parallel}$ based on the available data [42]. Parameter histograms corresponding to this choice, yielded $f \approx 0.5$, $D_a \approx 1.2\,\mu\text{m}^2/\text{ms}$ and $D_e^{\parallel} \approx 2.5\,\mu\text{m}^2/\text{ms}$ in human corpus callosum.

Since no specific model is assumed for the tortuosity $D_e^{\parallel}/D_e^{\perp}$, as $D_e^{\parallel}$ and $D_e^{\perp}$ are fitted separately, along with D_a and f, it was suggested the WMTI parameters could be used to disentangle between acute damage such as neurite beading, as reflected in D_a [159], and chronic damage including different types of demyelination and axonal loss, reflected in changes in the tortuosity, $D_e^{\perp}$ and f [147, 148]. As an *in vivo* validation, the age-related changes in the WMTI metrics were studied during the first two years of healthy brain development [158] (Figure 8), showing significant nonlinear increases in the f, $D_e^{\perp}$, related to increased myelination and axonal density, while no changes in the longitudinal compartment diffusivities, D_a and $D_e^{\parallel}$, as expected. *Ex vivo* animal validation studies provided reasonably accurate estimates of f in a mouse model of hypomyelination [160] and de-, and remyelination [149, 161]. Furthermore, mouse validation studies of the specificity to different types of neurodegeneration, demonstrated that D_a decreased during acute inflammation, while the axonal water fraction f decreased during the chronic phase of cuprizone intoxication [162], whereby $D_e^{\perp}$ and f were found to be respectively more sensitive to global and patchy demyelination [149].

These validation studies suggest increased *specificity* of the WMTI parameters to microstructural changes as compared to empirical diffusion metrics. However, while recent work showed that WMTI metrics correlate as expected with the concentration of (purely intra-axonal) NAA under the assumption $D_a < D_e^{\parallel}$ [163], the branch selection potentially may be the opposite one ($D_a > D_e^{\parallel}$, cf. Sec. III F below). This would affect the estimates of D_a and $D_e^{\parallel}$ (but not of f or $D_e^{\perp}$). This prompts both for improved SM parameter estimation methods (disucssed next in Sec. III E), as well as for "orthogonal" and more comprehensive validation methods to gain better understanding of the relevant tissue features of modeling (discussed in Sec. III F).

2. *Neurite Orientation Dispersion and Density Imaging (NODDI)*

NODDI, proposed by Zhang *et al.* [44], is a 3-compartment SM that assumes a Gaussian-like (Watson) ODF shape characterized by one [44] or two [164] parameters. In addition, the three diffusivities are effectively fixed, in the following way:

1. $D_a = D_e^{\parallel}$
2. $D_a = 1.7\,\mu\text{m}^2/\text{ms}$
3. Mean-field tortuosity model [165], $D_e^{\perp}/D_e^{\parallel} = 1 - f$.

The estimated parameters are f and f_{CSF}, as well as the ODF parameters (one or two parameters, depending on the Watson or Bingham distribution used). Using high resolution *ex vivo* imaging, it was recently showed that Bingham-NODDI is able to capture the cortical fibres known to exhibit fanning/bending in human neocortex [166]. However, recent extensive human measurement up to $b \leq 10\,\text{ms}/\mu\text{m}^2$ [48] also suggests that the above parameter constraints generally do not

hold, and therefore may bias the estimates of the fractions and fiber dispersion.

While both NODDI and WMTI rely on the same overarching SM, they differ in how they deal with the compartment diffusivities (fixed in NODDI, fitted in WMTI), the ODF (Watson in NODDI, single bundle in WMTI), and number of compartments (3 in NODDI, 2 in WMTI). The effect of these different constraints have been recently evaluated by studying changes in the model parameters through normal human early development [158] (Figure 8). In this work, qualitatively similar trends were observed in f, in full agreement with expected on-going myelination, fiber classification and asynchrony of development. The quantitative estimates, however, are model-dependent, exhibiting biases and limitations related to the models' assumptions. Similarly, changes during the first two years in fiber dispersion in the splenium corpus callosum were qualitatively different between NODDI and WMTl. This illustration clearly calls for extreme caution when interpreting modeling studies based on limited clinical dMRI data, where accuracy is typically sacrificed in favor of precision.

E. ODF factorization and rotational invariants

Let us now introduce the recently proposed family of approaches to SM parameter estimation that do not rely on specifying the ODF shape, by factoring it out in a rotationally invariant way. This will enable separation of estimating the scalar and the tensor (ODF) parameters. Of course, all the degeneracies of the parameter estimation will persist — and in fact, factoriztion has been used as a tool to prove that the above discussed degeneracies are completely general [47, 48].

Much like convolutions become products in the Fourier domain, the convolution (3.4) between the individual fiber response $\mathcal{K}$ and the ODF $\mathcal{P}$ becomes a product in the "spherical Fourier" domain (i.e. the SH basis):

$$S_{lm}(b) = p_{lm}\, K_l(b) \tag{3.18}$$

where $K_l(b)$ is the projection of the kernel $\mathcal{K}(b,\xi)$ onto the Legendre polynomial $(-)^{l/2}P_l(\xi)$ [39, 48, 49].

Since any rotation transforms SH components S_{lm} and p_{lm} according to a unitary transformation belonging to the $(2l+1)-$dimensional irreducible representation of SO(3) group labeled by "angular momentum" l, the 2-norms $\|p_{lm}\| \equiv \sqrt{\sum_{m=-l}^{l}|p_{lm}|^2}$ and $\|S_{lm}\|$ (defined likewise) are conserved under rotations, i.e. are rotational invariants. It is thus convenient to introduce[19] *rotational invariants* $p_l \equiv \|p_{lm}\|/\mathcal{N}_l$ and $S_l \equiv \|S_{lm}\|/\mathcal{N}_l$, where normalization $\mathcal{N}_l = \sqrt{4\pi(2l+1)}$ is chosen so that $0 \le p_l \le 1$. Hence, equations (3.18) for the (l,m) SH components gives rise to the corresponding equations for the rotational invariants [48, 49],

$$S_l(b,x) = p_l\, K_l(b,x)\,, \quad l = 0,\ 2,\ \dots\,, \tag{3.19}$$

where we denoted by x the dependence on the kernel's scalar parameters $x = \{f, D_a, D_e^{\parallel}, \dots\}$ to be estimated. The invariant $p_0 \equiv 1$ is trivial (ODF normalization); the remaining ODF invariants p_l, one for each l, characterize its anisotropy irrespective of the chosen basis.

1. *Isotropic $l = 0$ invariant $K_0(b)$*

The $l = 0$ invariant for Eq. (3.19) has been independently introduced under the names "powder averaging" and "spherical mean" [168–172]. The ODF factorization in this case is particularly simple to see, as it follows from swapping the order of integrations over $\hat{\mathbf{g}}$ and $\hat{\mathbf{n}}$:

$$\begin{aligned} S_0 &\propto \int \mathrm{d}\hat{\mathbf{g}} \int \mathrm{d}\hat{\mathbf{n}}\, \mathcal{P}(\hat{\mathbf{n}})\, \mathcal{K}(b, \hat{\mathbf{g}}\cdot\hat{\mathbf{n}}) \\ &= \int \mathrm{d}\hat{\mathbf{n}}\, \mathcal{P}(\hat{\mathbf{n}}) \int \mathrm{d}\hat{\mathbf{g}}\, \mathcal{K}(b, \hat{\mathbf{g}}\cdot\hat{\mathbf{n}}) \equiv \int_0^1 \mathrm{d}\cos\theta\, \mathcal{K}(b,\cos\theta)\,, \end{aligned}$$

since $\int \mathrm{d}\hat{\mathbf{g}}\, \mathcal{K}(b, \hat{\mathbf{g}}\cdot\hat{\mathbf{n}})$ is independent of fiber direction $\hat{\mathbf{n}}$ due to the "translational invariance" on a unit sphere, and the ODF is normalized to $\int \mathrm{d}\hat{\mathbf{n}}\, \mathcal{P}(\hat{\mathbf{n}}) \equiv 1$. The last identity above gives the projection of kernel (3.5) onto the $l = 0$ Legendre polynomial $P_0(\xi) \equiv 1$, where $\xi = \cos\theta$ in our case; for a stick compartment, this projection yields Eq. (3.2) above.

2. *Rotational invariants $K_l(b)$ for $l = 2, 4, \dots$*

Equation (3.19) formally yields an infinite family of rotational invariants $K_l(b)$ [48, 49], one for every $l = 2, 4, \dots$. However, it turns out that by far the most useful is the next-order, $l = 2$ invariant, since the projections of $e^{-bD\xi^2}$ onto the Legendre polynomials with $l > 2$, giving the compartment contributions to $K_l(b,x)$, are too slowly varying [39], adversely affecting the sensitivity to the estimated parameters x.

We also note that including the $l > 0$ invariants in system (3.19) is only possible for anisotropic ODFs, with $p_l > 0$. Physically, it is expected since the less symmetric the system, the more inequivalent ways it enables for probing it.[20] In the brain, the ODF is at least somewhat anisotropic; its lowest-order invariant p_2 is generally nonzero even in GM.

Parameter estimation based on the ODF factorization via the rotational invariants amounts to inverting the nonlinear relations (3.19) with respect to model parameters x and p_l.

[19] The idea to operate with a single "energy" L_2 norm per each "frequency" band l of SH has been previously applied e.g. to the problem of shape matching in computer graphics [167].

[20] This intuition underlies theory of quantum-mechanical excitations of non-spherical nuclei [173], where analogs of our rotational invariants are the corresponding irreducible tensor operators underpinning the Wigner-Eckart theorem.

Such inversion has so far been technically implemented in three distinct ways:

a. Analytically inverting relations between their Taylor expansions — i.e. expressing model parameters in terms of the moments of the signal (LEMONADE) [47];

b. Using the LEMONADE output as initialization for the RotInv solution of Eqs. (3.19) via nonlinear fitting using the gradient-descent optimization [48] to increase precision and accuracy;

c. Using the Bayesian RotInv framework, by generating the distributions of the invariants based on the prior distributions of x, and numerically inverting these relations based on the training set [49].

Overall, our (limited) experience tells that, no matter the implementation, the sensitivity to different scalar parameters varies dramatically (e.g. f is obtained reasonably well while the sensitivity to $D_e^{\parallel}$ and $D_e^{\perp}$ is quite lousy) [48, 49]; with decreasing SNR, methods (a) and (b) yield noisier parameter maps while method (c) yields "too clean" maps completely dominated by the mean values of parameter priors; multimodality manifests itself in the explicit need for the branch selection in all three approaches.

The lack of precision (due to the "continuous" degeneracy of shallow trenches) generally exists due to the multicompartmental nature of the kernel (3.5) [48]. One can say that any standard (directional) dMRI measurement effectively under-samples the scalar part of the model (3.4), not providing enough relations between the scalar parameters (cf. Sec. III C 4 above), and over-samples the tensor (ODF) part. In other words, the system's true complexity lies within the kernel's parameters hidden in functions $K_l(b,x)$, Eq. (3.19) — while the ODF is in some sense "lying on the surface".

This prompts the need for "orthogonal" measurement schemes [142, 172, 174, 175] which go beyond single (directional) pulsed-gradient encoding, and instead probe the scalar parameters in different combinations than entering the kernel projections $K_l(b,x)$, as we are now going to discuss.

F. Open questions: Precision and branch selection

We illustrated in Sec. III C 4 above that the dMRI signal as measured with typical single diffusion encoding in brain can be explained in terms of several distinctly different, though biophysical plausible SM parameter sets, which is in line with the previous description of it being "remarkably unremarkable" [176]. Orthogonal dMRI methods may help to increase the information content in the dMRI signal.

In particular, several methods have been proposed recently to resolve the branch choice, which has been generally formulated for any ODF [48] as a relation on the ratio $\beta = (D_a - D_e^{\parallel})/D_e^{\perp}$ involving the ground truth values of the three diffusivities (rather than the sign choice involving only the two of them, $D_a - D_e^{\parallel}$, as in the toy model in Sec. III C 3 above). However, practically speaking, the choice is numerically similar to choosing which out of the two "parallel" diffusivities, inside or outside axons, is greater, or is it rather degenerate, i.e. both diffusivities are almost the same inside and outside.

Based on high-quality human dMRI data with $0 \leq b \leq 10\,\mathrm{ms}/\mu\mathrm{m}^2$, it was conjectured [48] that branch selection may be opposite in WM and in GM, with $D_a \approx 2\,\mu\mathrm{m}^2/\mathrm{ms}$, while $D_e^{\parallel} \approx 1\,\mu\mathrm{m}^2/\mathrm{ms}$, so $D_a > D_e^{\parallel}$ in WM. This range of values for D_a is also consistent with the estimate following from the directional high-b measurement [121] which suppresses the extra-axonal contribution. Recent kurtosis measurements involving triple diffusion encoding (isotropic diffusion weighting), yielding for a 2-compartment SM

$$\frac{S(b)}{S(0)} = f e^{-bD_a} + (1-f) e^{-b(D_e^{\parallel}+2D_e^{\perp})}\,, \tag{3.20}$$

found relatively small kurtosis values [142] matching closer to the branch of $D_a \approx D_e^{\parallel} + 2D_e^{\perp} > D_e^{\parallel}$.

The branch choice has yet to be definitively validated in animal and human measurements, applying very strong diffusion gradients (e.g. employing unique *Human Connectom* scanners with gradients up to 300 mT/m), as well as "orthogonal" acquisitions such as extra-neurite water suppression by strong gradients [175] and isotropic weighting or spherical tensor encoding [142, 172, 174], cf. Eq. (3.20). It is also interesting to further investigate the branch-merging case of $D_a \approx D_e^{\parallel}$, as measured in rat spinal cord [175].

Finally, the orthogonal measurement — isotropic diffusion weighting, or spherical tensor encoding (STE) [172, 174], yielding the signal (3.20) — seems to be a great candidate for radically increasing the precision of the SM parameter estimation, as it depends on the scalar parameters x sufficiently differently from the dependence contained in the functions $K_l(b,x)$ in Eq. (3.19) above.

IV. MULTIPLE DIFFUSION ENCODINGS

The whole is greater than the sum of its parts

Aristotle

A. MDE basics

Multiple diffusion encoding (MDE) generalizes the Stejskal-Tanner (Sec. I D) pulse sequence design by adding one or more extra diffusion weighting blocks, as illustrated in Fig. 9 for the case of double diffusion encoding (DDE) [177–180]. Figure 9 also defines the main pulse sequence parameters for DDE, which in addition to the familiar Stejskal-Tanner parameters of each block, includes a mixing time τ.

In the following, we will restrict our attention to the narrow pulse limit. Generally, each diffusion weighting block is characterized by an independent diffusion wave vector $\mathbf{q}_n$ and diffusion time[21] t_n, and the mixing times define delays between blocks. Thus, a rich set of experimentally controllable parameters can in principle enable qualitatively different ways of probing the microstructure, as compared with the conventional, single diffusion encoded (SDE) sequences.

The fundamental question of the information content of MDE signal S_N relative to a set of independently acquired SDEs S_1 can be formulated using an example of the DDE signal S_2 (here we ignore the trivial $e^{-R_2 t}$ factors, assuming the unweighted signal to be normalized to unity):

$$S_2(\mathbf{q}_1,\mathbf{q}_2,t_1,t_2,\tau) \equiv \left\langle e^{i\mathbf{q}_1\cdot[\mathbf{r}(0)-\mathbf{r}(t_1)]+i\mathbf{q}_2\cdot[\mathbf{r}(t_2+\tau)-\mathbf{r}(t_1+t_2+\tau)]}\right\rangle$$
$$= \int \frac{\mathbf{dr}_{1a}\mathbf{dr}_{1b}\mathbf{dr}_{2a}\mathbf{dr}_{2b}}{V} e^{i\mathbf{q}_1\cdot(\mathbf{r}_{1a}-\mathbf{r}_{1b})+i\mathbf{q}_2\cdot(\mathbf{r}_{2a}-\mathbf{r}_{2b})}\,\mathcal{G}_{t_2;\mathbf{r}_{2b},\mathbf{r}_{2a}}\mathcal{G}_{\tau;\mathbf{r}_{2a},\mathbf{r}_{1b}}\mathcal{G}_{t_1;\mathbf{r}_{1b},\mathbf{r}_{1a}} \stackrel{?}{=} G_{t_2;\mathbf{q}_2}G_{t_1;\mathbf{q}_1}\,. \quad (4.1)$$

Technically, the above question is as follows: When does the convolution of the local propagators (1.5) defined in Sec. I D contain more information than the product of the voxel-averaged translation-invariant SDE propagators (1.7)?

Let us first outline the three cases when Eq. (4.1) holds, i.e. there is *no* extra information in MDE relative to SDE.

a. *Microscopic translation invariance:* If $\mathcal{G}_{t;\mathbf{r}_b,\mathbf{r}_a} \equiv G_{t,\mathbf{r}_b-\mathbf{r}_a}$ depends only on the relative displacement, the above equality holds for *any* $G_{t,\mathbf{r}}$. Of course, this is true for the Gaussian diffusion, when $G_{t,\mathbf{q}}$ is described by Eq. (1.8), but the statement is much broader, since its proof (by change of integration variables $\mathbf{r}_1 = \mathbf{r}_{1b}-\mathbf{r}_{1a}$ and $\mathbf{r}_2 = \mathbf{r}_{2b}-\mathbf{r}_{2a}$) involves only the translation invariance requirement. Practically, this means that the time scales involved in Eq. (4.1) exceed the time needed for the coarse-graining to restore sample's translation invariance, whether this implies the Gaussian fixed point (1.8) or its anomalous counterpart, cf. Sec. I I.

b. *Long mixing time limit of a single pore:* If all spins are confined in the same pore of volume V, and τ exceeds the time to diffuse across the pore size, the "mixing" propagator $\mathcal{G}_{\tau;\mathbf{r}_{2a},\mathbf{r}_{1b}} \to 1/V$ approaches a constant, and Eq. (4.1) again factorizes, irrespective of the (non-translation-invariant) functional form of $\mathcal{G}_{t;\mathbf{r}_b,\mathbf{r}_a}$.

c. *Weak diffusion weighting:* Equality (4.1) holds for any $\mathcal{G}$ at the level of $\mathcal{O}(q^2)$ [181], cf. Sec. IV B below. For this statement to hold, it is only required that the cumulant expansion (1.10) is regular around $q = 0$.

Generally, the above requirements do not hold — tissues are microscopically *not* translation-invariant, a voxel can contain multiple pores of various shapes (cf. Sec. IV C below), and diffusion weighting can be strong, so that the $\mathcal{O}(q^4)$ terms are relevant. This justifies using MDE to obtain extra information.

To get a feel for the difference between DDE and SDE, it is

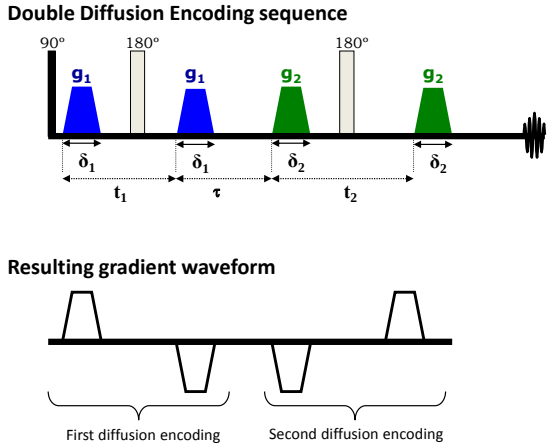

FIG. 9. (a) Example of a DDE sequence within the framework of a double spin echo. (b) The resulting gradient waveform. In text, we assume narrow-pulse approximation, such that $\delta_i \to 0$, with the Larmor frequency gradients g_i sufficiently large to yield finite $q_i = g_i\delta_i$ (no summation over i).

[21] Set by the corresponding interval Δ_n between the fronts of the gradient pulses, Fig. 9. For finite pulse width δ_n, see footnote 10 in Section II.

instructive to consider the long mixing time limit $\tau \to \infty$ in a system of disconnected pores. The average over Brownian paths splits into two parts: an average $\langle \dots \rangle$ over paths within a single pore, followed by an average (denoted by an overbar) over pores $\alpha = 1, \dots,$ with volume fractions $w_\alpha = V_\alpha/V$ adding to unity. For example, for the SDE signal (1.6):

$$S_1(\mathbf{q}_1, t) = \overline{\left\langle e^{i\mathbf{q}_1\cdot(\mathbf{r}(0)-\mathbf{r}(t))}\right\rangle_{\text{paths in pores}}} \equiv \sum_{\text{pores: }\alpha} w_\alpha \left\langle e^{i\mathbf{q}_1\cdot(\mathbf{r}(0)-\mathbf{r}(t))}\right\rangle_{\text{paths in }\alpha} .$$

For DDE, spin displacements in each of the diffusion-weighting blocks become independent of one another within each pore in the limit $\tau \to \infty$, $\mathcal{G}_{\tau;\mathbf{r}_{2a},\mathbf{r}_{1b}} \to 1/V_\alpha$ if $\mathbf{r}_{2a}$ and $\mathbf{r}_{1b}$ in Eq. (4.1) are from the same pore α with volume V_α, while the probability to hop between pores is zero: $\mathcal{G}_{\tau;\mathbf{r}_{2a},\mathbf{r}_{1b}} \equiv 0$ if $\mathbf{r}_{2a}$ and $\mathbf{r}_{1b}$ belong to different pores $\alpha \neq \beta$. This effective Kroeneker $\delta_{\alpha\beta}$ eliminates the cross-terms between different pores that are present in the right-hand side of Eq. (4.1):

$$S_2(\mathbf{q}_1, \mathbf{q}_2, t_1, t_2, \tau) = \overline{\left\langle e^{i\mathbf{q}_1\cdot(\mathbf{r}(0)-\mathbf{r}(t_1))+i\mathbf{q}_2\cdot[\mathbf{r}(t_2+\tau)-\mathbf{r}(t_1+t_2+\tau)]}\right\rangle} = \sum_\alpha w_\alpha \left\langle e^{i\mathbf{q}_1\cdot(\mathbf{r}(0)-\mathbf{r}(t_1))}\right\rangle_\alpha \left\langle e^{i\mathbf{q}_2\cdot(\mathbf{r}(t_2+\tau)-\mathbf{r}(t_1+t_2+\tau))}\right\rangle_\alpha . \quad (4.2)$$

Here the subscript "paths in α" was replaced with α for brevity. On the other hand, for the product of two SDE's we have

$$\begin{aligned} S_1(\mathbf{q}_1, t_1)\, S_1(\mathbf{q}_2, t_2) &= \overline{\left\langle e^{i\mathbf{q}_1\cdot(\mathbf{r}(0)-\mathbf{r}(t_1))}\right\rangle} \cdot \overline{\left\langle e^{i\mathbf{q}_2\cdot(\mathbf{r}(t_2+\tau)-\mathbf{r}(t_1+t_2+\tau))}\right\rangle} \\ &= \sum_\alpha w_\alpha w_\beta \left\langle e^{i\mathbf{q}_1\cdot(\mathbf{r}(0)-\mathbf{r}(t_1))}\right\rangle_\alpha \left\langle e^{i\mathbf{q}_2\cdot(\mathbf{r}(t_2+\tau)-\mathbf{r}(t_1+t_2+\tau))}\right\rangle_\beta \neq S_2(\mathbf{q}_1, \mathbf{q}_2, t_1, t_2, \tau) . \end{aligned} \quad (4.3)$$

The physical meaning of the above equations is as follows: it is not possible in general to split the coherent averaging of the product (4.2) over pores into the product of the averages (4.3).

The coherent disorder averaging of the propagators in equation (4.1) is also the reason that the effective medium theory [18, 24] for the disorder-averaged SDE propagator (1.6) has to be further augmented to incorporate the coarse-graining effects for MDE, relevant at finite τ.

B. Equivalence between MDE and SDE at $\mathcal{O}(q^2)$

Historically, DDE was noted to provide a method for determination of compartment dimensions [179] at low diffusion weighting in the limit of zero mixing time and long diffusion times. Taylor-expanding Eq. (4.2) in this limit, Mitra *et al.* [179] showed that in a system of identical pores

$$S_2(q\hat{\mathbf{n}}_1, q\hat{\mathbf{n}}_2, t, t, 0) \underset{t\to\infty}{\longrightarrow} 1 - \frac{1}{3}q^2\langle r^2\rangle \left[1 + 2\cos^2\frac{\theta}{2}\right], \quad (4.4)$$

where θ is the angle between the directions $\hat{\mathbf{n}}_1$ and $\hat{\mathbf{n}}_2$ of the diffusion wave vectors, and $\langle r^2\rangle = \int \mathrm{d}\mathbf{r}\mathrm{d}\mathbf{r}'\,(\mathbf{r}-\mathbf{r}')^2/2V^2 \equiv \int \mathrm{d}\mathbf{r}\,(\mathbf{r}-\mathbf{r}_{\mathrm{cm}})^2/V$ is the pore mean squared radius of gyration ($\mathbf{r}_{\mathrm{cm}}$ is pore center-of-mass), a measure of pore size.

Hence, a measure of the pore size can be determined from the signal dependence on diffusion wave vector angle in isotropic systems, or more simply from the signal difference between parallel and antiparallel diffusion wave vectors.

Equation (4.4) has since been generalized to take into account e.g. partial volume, multiple concatenations, pulse sequence timings (e.g. finite gradient width) for various geometries [182–188]. This has later been demonstrated by several groups in model systems and biological samples *ex vivo* [189–195], and *in vivo* in humans [196–199].

However, it was recently realized [181] that this property is the sensitivity (4.4) to pore gyration radius is a general feature of any diffusion-weighted signal at the $\mathcal{O}(q^2)$ level, and hence it does not rely on information beyond that already contained in the SDE signal, which in the same regime behaves as [200]:

$$\begin{aligned} S_1(\mathbf{q}, t) &\underset{t\to\infty}{\longrightarrow} 1 - \frac{1}{2}q_i q_j \langle (x_i(t) - x_i(0))(x_j(t) - x_j(0))\rangle \\ &= 1 - q^2\langle r^2\rangle . \end{aligned} \quad (4.5)$$

More generally, it was shown [181] that up to order $\mathcal{O}(q^2)$,

$$\begin{aligned} \ln S_2(\mathbf{q}_1, \mathbf{q}_2, t_1, t_2, \tau) = &-q_{1i}q_{1j}D_{ij}(t_1)t_1 + q_{2i}q_{2j}D_{ij}(t_2)t_2 \\ &+ q_{1i}q_{2j}\left[D_{ij}(t_1+t_2+\tau)(t_1+t_2+\tau) + D_{ij}(\tau)\tau - D_{ij}(t_1+\tau)(t_1+\tau) - D_{ij}(t_2+\tau)(t_2+\tau)\right] \\ &+ \mathcal{O}(q^4) , \end{aligned} \quad (4.6)$$

where $D_{ij}(t)$ is the cumulative diffusion tensor, Eq. (1.13). This explicitly demonstrates that the signal is fully character-

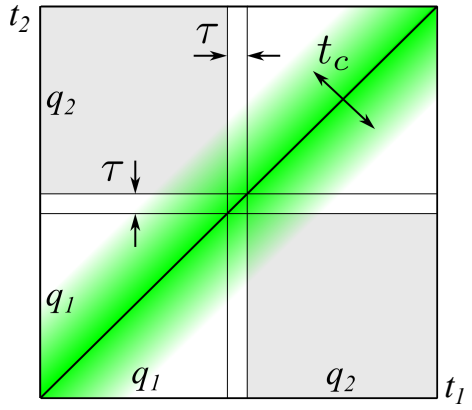

FIG. 10. Two-dimensional temporal integration involved in the second-order cumulant, Eq. (4.7) leading to Eq. (4.6) for the DDE measurement. Labels q_1 and q_2 indicate the time interval in which $\mathbf{q}(t)$ equals to $\mathbf{q}_1$ and $\mathbf{q}_2$, respectively; the vector indices are not shown for simplicity. The green shaded area along the diagonal symbolizes $\mathcal{D}_{ij}(|t_1-t_2|)$, Eq. (4.8), where it significantly deviates from 0, with the width of this region set by the correlation time t_c. The nontrivial cross-term $q_{1i}q_{2j}$ in Eq. (4.6) arises from the off-diagonal quadrants. As this contribution is weighted with the velocity autocorrelation function, it tends to zero when the mixing time, τ (indicated by the thin lines along each dimension) becomes larger than the correlation time, $\tau \gg t_c$. In particular, no non-trivial cross-term is present for Gaussian diffusion, for which $t_c \to 0$.

ized by the time-dependent diffusion tensor, a quantity which is obtainable from the SDE acquired at a few diffusion times. This statement is valid for *any* diffusion sequence up to second order in the diffusion wave vector [181, 201], and is a consequence of the existence of the cumulant series, whose lowest order can be completely reproduced by knowing the diffusion tensor for all t or, equivalently, for all ω [11, 101],

$$\ln S = -\frac{1}{2}\int \langle v_i(t_1)v_j(t_2)\rangle\, q_i(t_1)q_j(t_2)\,\mathrm{d}t_1\mathrm{d}t_2, \qquad (4.7)$$

where $\mathbf{q}(t)$ is the time integral of the arbitrary-shaped applied gradient, $\mathbf{v}$ is the molecular velocity, $\mathbf{v} = \partial_t\mathbf{r}$, and no bulk flow is assumed as usual. The (symmetric) autocorrelation function $\langle v_i(t_1)v_j(t_2)\rangle \equiv \mathcal{D}_{ij}(|t_1-t_2|)$ is constructed out of its retarded counterpart

$$\mathcal{D}_{ij}(t) \equiv \theta(t)\,\langle v_i(t)v_j(0)\rangle = \frac{\partial^2}{\partial t^2}\,[tD_{ij}(t)] \qquad (4.8)$$

defined by generalizing Eqs. (2.2) and (2.6) to the anisotropic case.

The function (4.8) is generally *nonlocal* in t [11, 12, 18, 24, 93, 101, 202, 203]. Figure 10 illustrates how this nonlocality, integrated in Eq. (4.7), gives rise to the cross-term $\sim q_{1i}q_{2j}$ (second line of Eq. (4.6)); this term disappears in the Gaussian diffusion limit, when $\langle v_i(t_1)v_j(t_2)\rangle = 2D_{ij}\delta(t_1-t_2)$ is infinitely narrow, and the function (4.8) is concentrated along the diagonal. Hence, the cross-term $\sim q_{1i}q_{2j}$ directly probes the time-dependence of the diffusion coefficient in Eq. (4.6), cf. Section II.

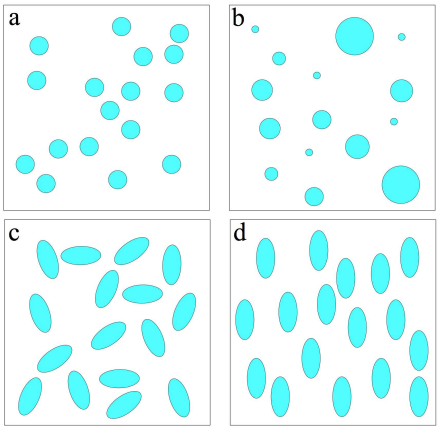

FIG. 11. Examples of model systems considered in the text. In (a), a system of identical spherical pores is shown, whereas, in (b), the pores have a distribution of sizes. In (c), an approximately isotropic distribution of ellipsoidal pores is sketched and, in (d), the pores are coherently oriented. Systems (a)–(c) are macroscopically isotropic, system (d) is not. Systems (c) and (d) are *microscopically anisotropic*. Ensemble heterogeneity is only seen in systems (b) (size) and (c) (orientation). Here, spins contributing to the signal are assumed to only reside within the pores.

C. Extra information relative to SDE at $\mathcal{O}(q^4)$ and beyond. Microscopic anisotropy

At larger values of the diffusion weighting, double diffusion encoding was shown from the beginning to have the ability to characterize microscopic anisotropy (μA) in systems which are macroscopically isotropic, Fig. 11, see panel (c). Thus, in an early application of the sequence by Cory *et al.* [178], DDE was used to quantitatively measure the eccentricity of yeast cells, which was shown to be directly related to the difference in signals acquired with parallel and perpendicular diffusion wave vectors. This has since been explored by many authors, e.g. in phantoms [204, 205], *ex vivo* tissues [206, 207], and *in vivo* [198, 208].

The basic sensitivity to anisotropic pores can be understood already from Eq. (4.2) in the long diffusion time and long mixing time limit

$$S_2(\mathbf{q}_1,\mathbf{q}_2,t_1,t_2,\tau) = \overline{|\chi_\alpha(\mathbf{q}_1)|^2|\chi_\alpha(\mathbf{q}_2)|^2} \qquad (4.9)$$

where $\chi_\alpha(\mathbf{q})$ is the Fourier transform of the pore structure function, defined as $\chi_\alpha(\mathbf{r}) \equiv 1/V_\alpha$ inside a pore and 0 otherwise [209].

For spherical pores, the structure function is isotropic, hence $\chi_\alpha(\mathbf{q})$ does not depend on the direction of $\mathbf{q}$. For anisotropic pores, say ellipsoids, the anisotropic structure functions $\chi_\alpha(\mathbf{q})$ in Eq. (4.9) ensure that the result depends on the directions of $\mathbf{q}_1$ and $\mathbf{q}_2$. This is because diffusion in the two directions is generally correlated when pores are non-spherical.

If the overall system is macroscopically isotropic, i.e. the orientations of the individual pores are randomly distributed (Fig. 11c), the signal will be unaffected by rotations

of the sample or of the laboratory system of reference, but the dependence on the relative angles between $\mathbf{q}_1$ and $\mathbf{q}_2$ will survive the pore averaging in Eq. (4.9). Mathematically speaking, this is because the two terms in the product $|\chi_\alpha(\mathbf{q}_1)|^2|\chi_\alpha(\mathbf{q}_2)|^2$ are not independent for a given pore, and hence the average of the product is different from the product of averages.

A convenient measure of the eccentricity of the pore space (microscopic anisotropy) can therefore be found from the difference of DDE signals acquired with parallel and perpendicular wave vectors $\mathbf{q}_1$ and $\mathbf{q}_2$. In the presence of macroscopic and microscopic anisotropy, the signal will depend on the orientations of *both* $\mathbf{q}_1$ and $\mathbf{q}_2$, and microscopic diffusion anisotropy can no longer be extracted simply from the difference between parallel and perpendicular diffusion wave vectors. The rotationally invariant way to circumvent this (cf. Sec. III E above) is to *powder average* the signal, analogously to how the K_0 invariant was introduced in Sec. III E 1 (although, technically, the averaging here is over the SO(3) group instead of a 2-sphere), and practical recipes for doing this were proposed in refs. [206, 210, 211]. Microscopic diffusion anisotropy can then be defined as the difference between (log of) the powder averaged signals acquired with parallel and perpendicular diffusion wave vectors [206].

Mitra's original results were since generalized to arbitrary diffusion and pulse timings by several authors [206, 210, 212]. Specifically, it was shown that in the long mixing time regime and for arbitrary diffusion times, the signal can be written as

$$\begin{aligned}\ln S_2(\mathbf{q}_1,\mathbf{q}_2) = &-(q_{1i}q_{1j}+q_{2i}q_{2j})D_{ij}(t)t\\ &+\frac{\overline{D}^2}{6}(q_{1i}q_{1j}q_{1k}q_{1l}+q_{2i}q_{2j}q_{2k}q_{2l})W_{ijkl}(t)\\ &+\frac{1}{4}q_{1i}q_{1j}q_{2k}q_{2l}Z_{ijkl}(t)\end{aligned} \tag{4.10}$$

where W is the kurtosis tensor as defined in [51] from the cumulant expansion (1.10) of the SDE propagator, whereas Z is a rank-4 tensor, unique to DDE, defined as

$$Z_{ijkl} = 4t^2\left(\overline{D^\alpha_{ij}D^\alpha_{kl}} - \overline{D^\alpha_{ij}}\,\overline{D^\alpha_{kl}}\right). \tag{4.11}$$

The tensors $D^\alpha_{ij}(t)$ refer to the microscopic t-dependent diffusion tensors characterizing diffusion within the pores, and the SDE-measured overall diffusion tensor $D_{ij}(t)$ entering the first line of Eq. (4.10) is an average over all pores, $D_{ij}(t) = \overline{D^\alpha_{ij}(t)} \equiv \sum_\alpha w_\alpha D^\alpha_{ij}(t)$.

The new tensor Z, Eq. (4.11), accessible with DDE (and inaccessible with SDE), is proportional to the covariance tensor of microscopic diffusion tensors. Microscopic diffusion anisotropy, *defined* as the difference between log of the powder averaged signals acquired with parallel and perpendicular diffusion wave vectors, can then be expressed as (see [206])

$$\begin{aligned}\varepsilon &= \frac{1}{60}\left[3Z_{ijij} - Z_{iijj} + 2t^2(3D_{ij}D_{ij} - D_{ii}D_{jj})\right]\\ &= \frac{t^2}{15}\left(3\overline{D^\alpha_{ij}D^\alpha_{ij}} - \overline{D^\alpha_{ii}D^\alpha_{jj}}\right) = \frac{3}{5}t^2\,\overline{\mathrm{var}\,\{\sigma_\alpha\}}.\end{aligned} \tag{4.12}$$

In the last equality, the set $\sigma_\alpha \equiv \{\sigma_{\alpha,i}\}_{i=1}^3$ denote the eigenvalues of D^α, and

$$\mathrm{var}\,\{\sigma_\alpha\} \equiv \frac{1}{3}\sum_{i=1}^3 \sigma^2_{\alpha,i} - \left[\frac{1}{3}\sum_{i=1}^3 \sigma_{\alpha,i}\right]^2. \tag{4.13}$$

With the above definition, $3\,\mathrm{tr}\,(D^\alpha)^2 - (\mathrm{tr}\,D^\alpha)^2 = 9\,\mathrm{var}\,\{\sigma_\alpha\}$ in Eq. (4.12). The anisotropy metric ε has dimensions of [length]^4. These somewhat awkward dimensions have a historical root in DDE eccentricity measurements [178]. While $\varepsilon \geq 0$, in practice it is often estimated from the difference of signals, which can become negative due to noise.

As an example, for randomly oriented (and identical) axially symmetric domains, such as fibers with (time-dependent) diffusivities $D_\parallel(t)$ and $D_\perp(t)$, microscopic diffusion anisotropy becomes

$$\varepsilon = \frac{2}{15}t^2\left[D_\perp(t) - D_\parallel(t)\right]^2. \tag{4.14}$$

If the domains are different, the corresponding Eq. (4.14) should be further averaged over them, cf. the $\overline{\mathrm{var}\,\{\sigma_\alpha\}}$ term in Eq. (4.12). Microscopic diffusion anisotropy hence depends explicitly on diffusion time, but tends to the geometric measures of pore shape anisotropy as the diffusion time increases, since for any confined region of size a, $D(t) \sim a^2/t$, and t asymptotically drops out from Eq. (4.14). From the time dependence of the microscopic diffusion anisotropy, non-Gaussian effects of the individual compartments can be revealed by the time dependence of the compartmental (microscopic) diffusion tensors.

Practically, the anisotropy metric (4.12) can be estimated from knowledge of the full Z tensor, or by the difference of the powder averaged log signals with parallel and perpendicular diffusion wave vectors. It has an advantage of being additive (cf. the pore average in Eq. (4.12)): if several distinct types of pore populations are present in the sample (e.g. a distribution of $D_\perp$ and $D_\parallel$ in Eq. 4.14), ε simply becomes the volume-weighted mean over the corresponding ε from each of the populations. This is an advantage since it eases the interpretation; however, the disadvantage is the dependence on size of the pore in addition to its anisotropy. This has the additional consequence that ε is strongly biased by the larger pores: Since $w_\alpha \sim a^3$ and $\varepsilon_\alpha \sim a^4$ for a pore of size a, the population averaged eccentricity scales as $\varepsilon \sim \overline{a^7}/\overline{a^3}$, heavily preferring the tail of the pore size distribution, — and hence susceptible to the mesoscopic fluctuations introduced in Sec. II E above, cf. Eq. (2.29).

To factor out the pore sizes, normalized dimensionless measures of microscopic diffusion anisotropy were introduced [206, 210, 213, 214], such as the microscopic fractional anisotropy, μFA:

$$\begin{aligned}\mu\mathrm{FA} &\equiv \sqrt{\frac{3}{2}\frac{(\sigma_1-\bar\sigma)^2+(\sigma_2-\bar\sigma)^2+(\sigma_3-\bar\sigma)^2}{\sigma_1^2+\sigma_2^2+\sigma_3^2}}\\ &= \sqrt{\frac{\varepsilon}{\varepsilon + \frac{3}{5}t^2\left(\frac{1}{3}\mathrm{tr}\,D\right)^2}}.\end{aligned} \tag{4.15}$$

In the previous example with axially symmetric domains, microscopic fractional anisotropy

$$\mu\mathrm{FA} = \sqrt{\frac{2}{3}}\frac{|D_\parallel - D_\perp|}{\sqrt{{D_\parallel}^2 + 2{D_\perp}^2}}\,, \tag{4.16}$$

whereas fractional anisotropy FA is modulated also by the fiber orientation distribution function [206, 215], and only recovers μFA when the fibers are all coherently aligned.

D. Concluding remarks on MDE

As we can see, MDE can potentially provide unique extra information relative to SDE. However, this information content only starts at the level of $\mathcal{O}(q^4)$, Eq. (4.10) (in addition to the standard SDE $\mathcal{O}(q^4)$ terms), and hence in order to claim the true novelty of the information, it has to be properly identified relative to the SDE measurements with similar scan parameters (timings and gradients). Clarifying the advantages of MDE is practically essential in the view of much reduced SNR due to a notable increase of the echo time needed for the multiple gradients to play out.

Overall, the main advantage of MDE so far seems to lie in its ability to detect and quantify microscopic diffusion anisotropy. In particular, the advantage of the DDE metrics of microscopic diffusion anisotropy (e.g. Eq. (4.12)) is that they do not rely on concrete assumptions regarding pore shapes.

Of course, if a detailed model of microstructure is available, e.g. of the Standard Model form (Section III), microscopic diffusion anisotropy is directly accessible in terms of model parameters (which can in principle be determined using SDE). However, even in this case, MDE adds value by providing an "orthogonal" way of being sensitive to model parameters — and, like in the SM case above, Sec. III F, it can provide rotationally invariant independent relations between parameters, which can help lift the parameter estimation degeneracies.

So far, the existing MDE models have been calculated in the limit of either Gaussian diffusion in all compartments, or in the $t_i \to \infty$ limit (e.g. closed pores). Importantly, the *transient* effects, cf. Section II, have not yet been properly accounted for in the MDE framework. In particular, the structural disorder-induced power-law tails in $D_{\mathrm{inst}}(t)$, or, equivalently, in $\mathcal{D}(\omega)$, such as the ones originating due to disordered axonal packing in the extra-axonal space [14, 25], will contribute to the "irreducible" MDE effects (that go beyond the product of a few SDE signals). Taking such transient processes into account seems *a priori* as crucial for the interpretation of MDE measurements, as it has been for the SDE — e.g. in the context of recent re-interpretation of the axonal diameter mapping results (cf. Sec. II D 2 above). The relevant coarse-graining formalism of the effective medium theory [14, 18, 24] seems perfectly suitable for the task — but has not yet been developed.

V. OUTLOOK AND OPEN QUESTIONS

There is nothing more practical than a good theory

L. Boltzmann

A. To model or not to model?

We are writing this Review at a transformational moment, when our field of quantitative dMRI is experiencing a revolution due to unprecedented quality of hardware and novel acquisition methods, enabling us to observe very subtle physical effects, even in human subjects and potentially in patients.

Interpreting these effects in terms of the mesoscopic tissue complexity is highly nontrivial; it is safe to say that the theoretical challenge has been so far greatly underappreciated. This, however, may swing the pendulum the other way, towards an "anti-modeling" point of view: Since, according to a widespread refrain, "biology is so much more complicated that anything physicists have ever studied", there is little hope for the quantitative understanding of such effects, and the best we can do is to stay at the level of "representations" (cf. Sec. I G) and to draw empirical correlations between parameters of such representations (e.g. mean diffusivity or fractional anisotropy) and the clinical disease scores.

One of the messages of our Review is that the whole history of Physics in the 20$^{\mathrm{th}}$ century offers the case for optimism. The quote from a nuclear physicist (before Section I) has been a universal refrain for our sustained ability to understand nature's complexity, from the origin of elementary particles to the vast scopes of the Universe. The essence of the effective theory way of thinking is that one certainly does *not* need to understand everything about the world in order to understand some corner of its parameter space really well. We certainly *can* quantify tissue architecture without uncovering the origins of the human conscience or mapping full details of the brain's biochemical machinery. Too often, "biology is way more complex than all your models" has been merely an excuse not to develop better models.

We reject this excuse. We believe that having appropriate theoretical description of diffusion in tissues at the mesoscopic scale is not a luxury at this point — rather, this is an indispensable scientific *method of investigation* into pathological processes 2-3 orders of magnitude below nominally achievable resolution of MRI in any foreseeable future — or, in fact, ever, since the MRI resolution is stringently bounded by physical and physiological limitations that have been largely reached by now. The parallels with super-resolution microscopy [216] are quite obvious; that discipline took a century to develop, based on employing models and prior information. Our task is harder but, arguably, can lead to even more impactful advances.

With that in mind, let us outline 10 exciting unresolved problems, focussing on which, to the best of our understanding, will propel our field forward.

B. Ten problems for mesoscopic dMRI

1. **Apparent vs. real diffusion metrics:** What are the confounding effects of mesoscopically varying $R_1(\mathbf{r})$, $R_2(\mathbf{r})$, and $\Omega(\mathbf{r})$ in the mesoscopic Bloch-Torrey equation (1.1) on the observed diffusion metrics, in the spirit of refs. [8, 9]? Can we develop a multi-modal mesoscopic imaging framework able to self-consistently quantify all these mesoscopic quantities and disentangle their effects in the apparent diffusion coefficients and higher-order metrics in each tissue compartment?

2. **Relation between time-dependent $D_\perp(t)$ and its tortuosity limit D_∞, and the geometric parameters of realistic axonal packings:** As the time dependence of the diffusion transverse to fiber tracts is dominated by the extra-axonal water (Section II), the natural question is what structural changes (e.g. demyelination, axonal loss) can affect this time dependence, as well as D_∞. This is a difficult yet clinically impactful inverse problem [147], whose approximate solution, relying on the ideas of coarse-graining and renormalization, has so far only been obtained in the $t \to \infty$ limit [148].

3. **Origin of structural disorder along the neurites:** What causes the time dependence along the fibers or in the gray matter? Is it varicosities, beads, synaptic boutons, undulations, or something else? Which of these structural units' changes in pathology can be detectable?

4. **Parameter estimation challenge for the Standard Model:** How many Gaussian compartments do we have to include? For increasing the precision, it looks like we need orthogonal measurements, such as isotropic diffusion weighting and MDE. What is an optimal clinically feasible measurement protocol?

5. **Time-dependent rotationally-invariant framework:** Combining the ideas of Sections II and III can lead to describing each fiber fascile in terms of the non-Gaussian propagators (inside and outside the neurites) with the corresponding time-dependent diffusion, kurtosis, etc, cumulant tensors; such fascicles then naturally combine into the SM-like signal based on the fiber ODF in a voxel. This difficult parameter estimation problem may offer the all-encompassing description of diffusion process measurable with dMRI in the brain.

6. **Permeability/exchange time for the neurites:** How well we can approximate compartments as non-exchanging? At which time scales this assumption breaks? The answer most likely will be different for gray and white matter, and maybe even for different brain regions.

7. **Standard Model for GM:** Can we apply SM as introduced in Section III to gray matter *in vivo* at clinical diffusion times, or should we modify the compartments? Do we have to include exchange, and if yes, at which level?

8. **EMT for MDE:** Development of the effective medium theory framework [18] for the "disorder-averaging" involved in the multiple diffusion encoding signal (Section IV). Which physical effects, from the EMT standpoint, are best captured using MDE, or are completely absent in the SDE?

9. **Signal vs. noise:** As the saying goes, "noise is signal". The fundamental question is to separate the thermal noise, imaging artifacts, as well as the genuine differences between parameters in voxels belonging to the same region of interest. Recently developed random matrix theory-based approaches [131, 132] offer an exciting prospect.

10. **Mesoscopic fluctuations and biological variability:** How different are the mesoscopic tissue parameters within a given region of interest? Their differences provide the "natural" minimal width for the parameter distributions within an ROI, in the limit of infinite SNR. Sometimes, relatively small differences in the mesoscopic parameters can translate into large differences of the dMRI metrics; heavy sensitivity of the signal from the inside axons to the tail of the axonal diameter distribution [14] (Secs. II E, IV C) is an example of an effect of so-called "mesoscopic fluctuations" pioneered within condensed matter physics [7]. Studying these fluctuations can provide fundamental insights on the optimality and robustness of the organization of neuronal tissue microarchitecture, as well as offer practical limits on our detection capabilities.

ACKNOWLEDGMENTS

It is a pleasure to thank our numerous colleagues and members of our research groups for stimulating discussions and collaborations which are reflected in our Review. In particular, we thank Christian Beaulieu and Gene Kim for discussions on experimental issues, and Dan Wu and Jiangyang Zhang for sharing their OGSE data displayed in Fig. 6. Photo credit to Tom Deerinck and Mark Ellisman (National Center for Microscopy and Imaging Research) for the histology image illustrating a fiber fascicle in Figs. 1 and 7.

E.F. and D.S.N. were supported by the Fellowship from Raymond and Beverly Sackler Laboratories for Convergence of Physical, Engineering and Biomedical Sciences, by the Litwin Foundation for Alzheimer's Research, and by the National Institute of Neurological Disorders and Stroke of the NIH under award number R01NS088040. SNJ was supported by the Danish Ministry of Science, Technology and Innovations University Investment Grant (MINDLab, Grant no. 0601-01354B), and the Lundbeck Foundation R83-A7548.

[1] Howard Georgi, "Effective field theory," Annual review of nuclear and particle science **43**, 209–252 (1993).

[2] Philip W Anderson, "More is different," Science **177**, 393–396 (1972).

[3] Kenneth G Wilson, "The renormalization group and critical phenomena," Reviews of Modern Physics **55**, 583 (1983).

[4] John Cardy, *Scaling and renormalization in statistical physics*, Vol. 5 (Cambridge university press, 1996).

[5] N. Bloembergen, E. M. Purcell, and R. V. Pound, "Relaxation effects in nuclear magnetic resonance absorption," Physical Review **73**, 679–712 (1948).

[6] A Abragam, *Principles of Nuclear Magnetism* (Oxford University Press, New York, 1961).

[7] Yoseph Imry, *Introduction to mesoscopic physics* (Oxford University Press, New York, 1997).

[8] Jianhui Zhong, Richard P Kennan, and John C Gore, "Effects of susceptibility variations on {NMR} measurements of diffusion," Journal of Magnetic Resonance (1969) **95**, 267 – 280 (1991).

[9] V G Kiselev, "Effect of magnetic field gradients induced by microvasculature on nmr measurements of molecular self-diffusion in biological tissues," J Magn Reson **170**, 228–35 (2004).

[10] P T Callaghan, *Principles of Nuclear Magnetic Resonance Microscopy* (Clarendon, Oxford, 1991).

[11] Valerij G Kiselev, "Diffusion MRI: Theory, methods and applications," (Ed. Jones, D. K., Oxford University Press, New York, 2010) Chap. 10. The cumulant expansion: An overarching mathematical framework for understanding diffusion NMR.

[12] Valerij G. Kiselev, "Fundamentals of diffusion MRI physics," NMR In Biomedicine **DOI:10.1002/nbm.3602** (2016).

[13] C. H. Neuman, "Spin echo of spins diffusing in a bounded medium," Journal of Chemical Physics **60**, 4508–4511 (1974).

[14] Lauren M Burcaw, Els Fieremans, and Dmitry S Novikov, "Mesoscopic structure of neuronal tracts from time-dependent diffusion," NeuroImage **114**, 18–37 (2015).

[15] Hong-Hsi Lee, Lauren M. Burcaw, Jelle Veraart, Els Fieremans, and Dmitry S. Novikov, "Low-pass filter effect of finite gradient duration on time-dependent diffusion in the human brain," Proceedings of the International Society of Magnetic Resonance in Medicine 23, p. 2777 (2015).

[16] Hong-Hsi Lee, Jelle Veraart, Dmitry S. Novikov, and Els Fieremans, "What dominates the diffusivity time dependence transverse to axons: Intra- or extra-axonal water?" Proceedings of the International Society of Magnetic Resonance in Medicine 24, p. 0656 (2016).

[17] Hong-Hsi Lee, Gregory Lemberskiy, Els Fieremans, and Dmitry S. Novikov, "Estimation of fiber packing correlation length by varying diffusion gradient pulse duration," Proceedings of the International Society of Magnetic Resonance in Medicine 24, p. 2021 (2016).

[18] Dmitry S Novikov and Valerij G Kiselev, "Effective medium theory of a diffusion-weighted signal," NMR Biomed **23**, 682–97 (2010).

[19] P.T. Callaghan, C.D. Eccles, and Y. Xia, "Nmr microscopy of dynamic displacements: k-space and q-space imaging," Journal of Physics E: Scientific Instruments **21**, 820–822 (1988).

[20] D G Cory and A N Garroway, "Measurement of translational displacement probabilities by nmr: an indicator of compartmentation," Magn Reson Med **14**, 435–44 (1990).

[21] Denis Le Bihan, Eric Breton, Denis Lallemand, Philippe Grenier, Emmanuel Cabanis, and Maurice Laval-Jeantet, "MR imaging of intravoxel incoherent motions: application to diffusion and perfusion in neurologic disorders." Radiology **161**, 401–407 (1986).

[22] Pj Basser, J Mattiello, and D LeBihan, "Estimation of the effective self-diffusion tensor from the NMR spin-echo," Journal of Magnetic Resonance Series B **103**, 247–254 (1994).

[23] P P Mitra, P N Sen, L M Schwartz, and P Le Doussal, "Diffusion propagator as a probe of the structure of porous media," Physical Review Letters **68**, 3555–3558 (1992).

[24] Dmitry S Novikov, Jens H Jensen, Joseph A Helpern, and Els Fieremans, "Revealing mesoscopic structural universality with diffusion," Proc Natl Acad Sci U S A **111**, 5088–93 (2014).

[25] Els Fieremans, Lauren M Burcaw, Hong-Hsi Lee, Gregory Lemberskiy, Jelle Veraart, and Dmitry S Novikov, "In vivo observation and biophysical interpretation of time-dependent diffusion in human white matter," NeuroImage (2016).

[26] JE Tanner, "Transient diffusion in a system partitioned by permeable barriers. application to nmr measurements with a pulsed field gradient," The Journal of Chemical Physics **69**, 1748–1754 (1978).

[27] J. G. Powles, M. J. D. Mallett, G. Rickayzen, and W. A. B. Evans, "Exact analytic solutions for diffusion impeded by an infinite array of partially permeable barriers," Proceedings of the Royal Society of London. Series A: Mathematical and Physical Sciences **436**, 391–403 (1992).

[28] A L Sukstanskii, D A Yablonskiy, and J J H Ackerman, "Effects of permeable boundaries on the diffusion-attenuated MR signal: insights from a one-dimensional model," Journal of Magnetic Resonance **170**, 56–66 (2004).

[29] Dmitry S. Novikov, Els Fieremans, Jens H. Jensen, and Joseph A. Helpern, "Random walks with barriers," Nature Physics **7**, 508–514 (2011).

[30] Eric E Sigmund, Dmitry S Novikov, Dabang Sui, Obehi Ukpebor, Steven Baete, James S Babb, Kecheng Liu, Thorsten Feiweier, Jane Kwon, KellyAnne McGorty, *et al.*, "Time-dependent diffusion in skeletal muscle with the random permeable barrier model (RPBM): application to normal controls and chronic exertional compartment syndrome patients," NMR in Biomedicine **27**, 519–528 (2014).

[31] Els Fieremans, Gregory Lemberskiy, Jelle Veraart, Eric E Sigmund, Soterios Gyftopoulos, and Dmitry S Novikov, "In vivo measurement of membrane permeability and myofiber size in human muscle using time-dependent diffusion tensor imaging and the random permeable barrier model," NMR Biomed (2016), 10.1002/nbm.3612.

[32] PT Callaghan, KW Jolley, and J Lelievre, "Diffusion of water in the endosperm tissue of wheat grains as studied by pulsed field gradient nuclear magnetic resonance," Biophysical journal **28**, 133–141 (1979).

[33] Dmitriy A Yablonskiy, Alexander L Sukstanskii, Jason C Leawoods, David S Gierada, G Larry Bretthorst, Stephen S Lefrak, Joel D Cooper, and Mark S Conradi, "Quantitative in vivo assessment of lung microstructure at the alveolar level with hyperpolarized 3he diffusion mri," Proceedings of the National Academy of Sciences **99**, 3111–3116 (2002).

[34] G.J. Stanisz, A. Szafer, G.A. Wright, and R.M. Henkelman, "An analyitical model of restricted diffusion in bovine optic

nerve," Magnetic Resonance in Medicine **37**, 103–111 (1997).
[35] Y Assaf, R Z Freidlin, G K Rohde, and P J Basser, "New modeling and experimental framework to characterize hindered and restricted water diffusion in brain white matter," Magnetic Resonance In Medicine **52**, 965–978 (2004).
[36] Y. Assaf, T. Blumenfeld-Katzir, Y. Yovel, and P.J. Basser, "Axcaliber: A method for measuring axon diameter distribution from diffusion mri," Magnetic Resonance In Medicine **59**, 1347–1354 (2008).
[37] D.C. Alexander, P.L. Hubbard, M.G. Hall, E.A. Moore, M. Ptito, G.J.M. Parker, and T.B. Dyrby, "Orientationally invariant indices of axon diameter and density from diffusion mri," Neuroimage **52**, 1374–1389 (2010).
[38] Christopher D Kroenke, Joseph J H Ackerman, and Dmitriy A Yablonskiy, "On the nature of the NAA diffusion attenuated MR signal in the central nervous system," Magn Reson Med **52**, 1052–9 (2004).
[39] Sune N. Jespersen, Christopher D. Kroenke, Leif Ostergaard, Joseph J. H. Ackerman, and Dmitriy A. Yablonskiy, "Modeling dendrite density from magnetic resonance diffusion measurements," Neuroimage **34**, 1473–1486 (2007).
[40] Sune N. Jespersen, Carsten R. Bjarkam, Jens R. Nyengaard, M. Mallar Chakravarty, Brian Hansen, Thomas Vosegaard, Leif Ostergaard, Dmitriy Yablonskiy, Niels Chr. Nielsen, and Peter Vestergaard-Poulsen, "Neurite density from magnetic resonance diffusion measurements at ultrahigh field: Comparison with light microscopy and electron microscopy," Neuroimage **49**, 205–216 (2010).
[41] Els Fieremans, Dmitry S. Novikov, Jens H. Jensen, and Joseph A. Helpern, "Monte Carlo study of a two-compartment exchange model of diffusion," NMR in Biomedicine **23**, 711–724 (2010).
[42] Els Fieremans, Jens H Jensen, and Joseph A Helpern, "White matter characterization with diffusional kurtosis imaging," Neuroimage **58**, 177–88 (2011).
[43] Stamatios N Sotiropoulos, Timothy EJ Behrens, and Saad Jbabdi, "Ball and rackets: inferring fiber fanning from diffusion-weighted mri," NeuroImage **60**, 1412–1425 (2012).
[44] Hui Zhang, Torben Schneider, Claudia A Wheeler-Kingshott, and Daniel C Alexander, "NODDI: practical in vivo neurite orientation dispersion and density imaging of the human brain," Neuroimage **61**, 1000–16 (2012).
[45] Marco Reisert, Valerij G Kiselev, Bibek Dihtal, Elias Kellner, and DS Novikov, "Mesoft: unifying diffusion modelling and fiber tracking," in *Medical Image Computing and Computer-Assisted Intervention–MICCAI 2014* (Springer, 2014) pp. 201–208.
[46] Ileana O Jelescu, Jelle Veraart, Els Fieremans, and Dmitry S Novikov, "Degeneracy in model parameter estimation for multi-compartmental diffusion in neuronal tissue," NMR in Biomedicine **29**, 33–47 (2016).
[47] Dmitry S. Novikov, Ileana O. Jelescu, and Els Fieremans, "From diffusion signal moments to neurite diffusivities, volume fraction and orientation distribution: An exact solution," Proceedings of the International Society of Magnetic Resonance in Medicine 23, p. 469 (2015).
[48] Dmitry S. Novikov, Jelle Veraart, Ileana O. Jelescu, and Els Fieremans, "Mapping orientational and microstructural metrics of neuronal integrity with *in vivo* diffusion MRI," preprint arXiv:1609.09144 **https://arxiv.org/abs/1609.09144** (2016).
[49] Marco Reisert, Elias Kellner, Bibek Dhital, JÃrgen Hennig, and Valerij G. Kiselev, "Disentangling micro from mesostructure by diffusion mri: A bayesian approach," NeuroImage **http://www.sciencedirect.com/science/article/pii/S1053811916305353** – (2016).
[50] D Le Bihan, C T Moonen, P C van Zijl, J Pekar, and D DesPres, "Measuring random microscopic motion of water in tissues with mr imaging: a cat brain study," J Comput Assist Tomogr **15**, 19–25 (1991).
[51] Jens H Jensen, Joseph A Helpern, Anita Ramani, Hanzhang Lu, and Kyle Kaczynski, "Diffusional kurtosis imaging: the quantification of non-gaussian water diffusion by means of magnetic resonance imaging," Magn Reson Med **53**, 1432–40 (2005).
[52] D S Novikov and V G Kiselev, "Transverse NMR relaxation in magnetically heterogeneous media," J Magn Reson **195**, 33–9 (2008).
[53] Evren Özarslan, Cheng Guan Koay, Timothy M Shepherd, Michal E Komlosh, M Okan İrfanoğlu, Carlo Pierpaoli, and Peter J Basser, "Mean apparent propagator (map) mri: a novel diffusion imaging method for mapping tissue microstructure," Neuroimage **78**, 16–32 (2013).
[54] Dmitriy A Yablonskiy, G Larry Bretthorst, and Joseph J H Ackerman, "Statistical model for diffusion attenuated mr signal," Magn Reson Med **50**, 664–9 (2003).
[55] Yong Wang, Qing Wang, Justin P Haldar, Fang-Cheng Yeh, Mingqiang Xie, Peng Sun, Tsang-Wei Tu, Kathryn Trinkaus, Robyn S Klein, Anne H Cross, *et al.*, "Quantification of increased cellularity during inflammatory demyelination," Brain **134**, 3590–3601 (2011).
[56] Nathan S White, Trygve B Leergaard, Helen D'Arceuil, Jan G Bjaalie, and Anders M Dale, "Probing tissue microstructure with restriction spectrum imaging: histological and theoretical validation," Human brain mapping **34**, 327–346 (2013).
[57] Benoit Scherrer, Armin Schwartzman, Maxime Taquet, Mustafa Sahin, Sanjay P Prabhu, and Simon K Warfield, "Characterizing brain tissue by assessment of the distribution of anisotropic microstructural environments in diffusion-compartment imaging (diamond)," Magn Reson Med **76**, 963–77 (2016).
[58] T E J Behrens, M W Woolrich, M Jenkinson, H Johansen-Berg, R G Nunes, S Clare, P M Matthews, J M Brady, and S M Smith, "Characterization and propagation of uncertainty in diffusion-weighted MR imaging," Magn Reson Med **50**, 1077–88 (2003).
[59] TEJ Behrens, H Johansen-Berg, MW Woolrich, SM Smith, CAM Wheeler-Kingshott, PA Boulby, GJ Barker, EL Sillery, K Sheehan, O Ciccarelli, *et al.*, "Non-invasive mapping of connections between human thalamus and cortex using diffusion imaging," Nature Neuroscience **6**, 750–757 (2003).
[60] Paul T Callaghan, Andrew Coy, David MacGowan, Ken J Packer, and Fernando O Zelaya, "Diffraction-like effects in NMR diffusion studies of fluids in porous solids," Nature **351**, 467–469 (1991).
[61] Jens H Jensen, Joseph A Helpern, Anita Ramani, Hanzhang Lu, and Kyle Kaczynski, "Diffusional kurtosis imaging: the quantification of non-gaussian water diffusion by means of magnetic resonance imaging," Magn Reson Med **53**, 1432–1440 (2005).
[62] R. A. Fisher and J. Wishart, "The derivation of the pattern formulae of two-way partitions from those of simpler patterns," Proc. London Math. Soc. (1) **s2-33**, 195–208 (1932).
[63] N G van Kampen, *Stochastic Processes in Physics and Chemistry*, 1st ed. (Elsevier, Oxford, 1981).
[64] A. F. Frøhlich, L. Ostergaard, and V. G. Kiselev, "Effect of impermeable boundaries on diffusion-attenuated MR signal," J. Magn. Reson. **179**, 223–233 (2006).
[65] Valerij G Kiselev and Kamil A Il'yasov, "Is the "biexponen-

tial diffusion" biexponential?" Magn Reson Med **57**, 464–9 (2007).

[66] Jens H Jensen and Joseph A Helpern, "Mri quantification of non-gaussian water diffusion by kurtosis analysis," NMR Biomed **23**, 698–710 (2010).

[67] Jelle Veraart, Jeny Rajan, Ronald R Peeters, Alexander Leemans, Stefan Sunaert, and Jan Sijbers, "Comprehensive framework for accurate diffusion mri parameter estimation," Magn Reson Med **70**, 972–84 (2013).

[68] Kip S Thorne, "Multipole expansions of gravitational radiation," Reviews of Modern Physics **52**, 299–339 (1980).

[69] J-P Bouchaud and A Georges, "Anomalous diffusion in disordered media - statistical mechanisms, models and physical applications," Physics Reports - Review Section of Physics Letters **195**, 127–293 (1990).

[70] AS Lamantia and P Rakic, "Cytological and quantitative characteristics of 4 cerebral commissures in the rhesus-monkey," Journal of Comparative Neurology **291**, 520–537 (1990).

[71] F. Aboitiz, A.B. Scheibel, R.S. Fisher, and E. Zaidel, "Fiber composition of the human corpus callosum," Brain Research **598**, 143–153 (1992).

[72] Roberto Caminiti, Hassan Ghaziri, Ralf Galuske, Patrick R Hof, and Giorgio M Innocenti, "Evolution amplified processing with temporally dispersed slow neuronal connectivity in primates," Proceedings of the National Academy of Sciences **106**, 19551–19556 (2009).

[73] VE Kravtsov, IV Lerner, and VI Yudson, "Random walks in media with constrained disorder," Journal of Physics A: Mathematical and General **18**, L703 (1985).

[74] Sinai Y. G., "The limiting behavior of a one-dimensional random walk in a random medium," Theory Probab. Appl. **27**, 256–268 (1982).

[75] Daniel S Fisher, "Random walks in random environments," Physical Review A **30**, 960 (1984).

[76] JA Aronovitz and David R Nelson, "Anomalous diffusion in steady fluid flow through a porous medium," Physical Review A **30**, 1948 (1984).

[77] Daniel S Fisher, Daniel Friedan, Zongan Qiu, Scott J Shenker, and Stephen H Shenker, "Random walks in two-dimensional random environments with constrained drift forces," Physical Review A **31**, 3841 (1985).

[78] Yan-Chr Tsai and Yonathan Shapir, "On the scale-invariant distribution of the diffusion coefficient for classical particles diffusing in disordered media," Journal of Physics A: Mathematical and General **26**, 39 (1993).

[79] Igor V Lerner, "Distributions of the diffusion coefficient for the quantum and classical diffusion in disordered media," Nuclear Physics A **560**, 274–292 (1993).

[80] B I Shklovskii and A L Efros, *Electronic properties of doped semiconductors* (Springer, Heidelberg, 1984).

[81] S Havlin, M Schwartz, R B Selinger, A Bunde, and H E Stanley, "Universality classes for diffusion in the presence of correlated spatial disorder," Physical Review A **40**, 1717–1719 (1989).

[82] S Havlin and D Ben-Avraham, "Diffusion in disordered media," Advances In Physics **51**, 187–292 (2002).

[83] Matan Mussel, Lilah Inzelberg, and Uri Nevo, "Insignificance of active flow for neural diffusion weighted imaging: A negative result," Magnetic Resonance in Medicine , DOI:10.1002/mrm.26375 (2016).

[84] Christian Beaulieu and Peter S Allen, "An in vitro evaluation of the effects of local magnetic-susceptibility-induced gradients on anisotropic water diffusion in nerve," Magnetic resonance in medicine **36**, 39–44 (1996).

[85] Yaniv Assaf and Yoram Cohen, "Assignment of the water slow-diffusing component in the central nervous system using q-space diffusion mrs: Implications for fiber tract imaging," Magnetic resonance in medicine **43**, 191–199 (2000).

[86] A. Bar-Shir, L. Avram, E. Özarslan, P.J. Basser, and Y. Cohen, "The effect of the diffusion time and pulse gradient duration ratio on the diffraction pattern and the structural information estimated from q-space diffusion mr: Experiments and simulations," Journal of Magnetic Resonance **194**, 230–236 (2008).

[87] Nicolas Kunz, Stéphane V Sizonenko, Petra S Hüppi, Rolf Gruetter, and Yohan Looij, "Investigation of field and diffusion time dependence of the diffusion-weighted signal at ultrahigh magnetic fields," NMR in biomedicine **26**, 1251–1257 (2013).

[88] Peter van Gelderen, Marloes HM de Vleeschouwer, Daryl DesPres, James Pekar, Peter van Zijl, and Chrit TW Moonen, "Water diffusion and acute stroke," Magnetic resonance in medicine **31**, 154–163 (1994).

[89] Chris A Clark, Maj Hedehus, and Michael E Moseley, "Diffusion time dependence of the apparent diffusion tensor in healthy human brain and white matter disease," Magnetic resonance in medicine **45**, 1126–1129 (2001).

[90] Markus Nilsson, Jimmy Lätt, Emil Nordh, Ronnie Wirestam, Freddy Strahlberg, and Sara Brockstedt, "On the effects of a varied diffusion time in vivo: is the diffusion in white matter restricted?" Magnetic resonance imaging **27**, 176–187 (2009).

[91] Mark A Horsfield, Gareth J Barker, and W Ian McDonald, "Self-diffusion in cns tissue by volume-selective proton nmr," Magnetic resonance in medicine **31**, 637–644 (1994).

[92] Silvia De Santis, Derek K Jones, and Alard Roebroeck, "Including diffusion time dependence in the extra-axonal space improves in vivo estimates of axonal diameter and density in human white matter," NeuroImage **130**, 91–103 (2016).

[93] M.D. Does, E.C. Parsons, and J.C. Gore, "Oscillating gradient measurements of water diffusion in normal and globally ischemic rat brain," Magnetic Resonance In Medicine **49**, 206–215 (2003).

[94] Junzhong Xu, Hua Li, Kevin D Harkins, Xiaoyu Jiang, Jingping Xie, Hakmook Kang, Mark D Does, and John C Gore, "Mapping mean axon diameter and axonal volume fraction by MRI using temporal diffusion spectroscopy," NeuroImage **103**, 10–19 (2014).

[95] Nadya Pyatigorskaya, Denis Bihan, Olivier Reynaud, and Luisa Ciobanu, "Relationship between the diffusion time and the diffusion mri signal observed at 17.2 tesla in the healthy rat brain cortex," Magnetic resonance in medicine **72**, 492–500 (2014).

[96] Dan Wu, Lee J Martin, Frances J Northington, and Jiangyang Zhang, "Oscillating gradient diffusion mri reveals unique microstructural information in normal and hypoxia-ischemia injured mouse brains," Magnetic resonance in medicine **72**, 1366–1374 (2014).

[97] Dan Wu and Jiangyang Zhang, "The effect of microcirculatory flow on oscillating gradient diffusion MRI and diffusion encoding with dual-frequency orthogonal gradients (DEFOG)," Magnetic Resonance in Medicine , n/a–n/a (2016).

[98] Corey A Baron and Christian Beaulieu, "Oscillating gradient spin-echo (ogse) diffusion tensor imaging of the human brain," Magnetic resonance in medicine **72**, 726–736 (2014).

[99] Anh T Van, Samantha J Holdsworth, and Roland Bammer, "In vivo investigation of restricted diffusion in the human brain with optimized oscillating diffusion gradient encoding," Magnetic resonance in medicine **71**, 83–94 (2014).

[100] JE Tanner, "Self diffusion of water in frog muscle." Biophysical journal **28**, 107 (1979).

[101] Dmitry S. Novikov and Valerij G. Kiselev, "Surface-to-volume ratio with oscillating gradients," Journal of Magnetic Resonance **210**, 141–145 (2011).

[102] L L Latour, K Svoboda, P P Mitra, and C H Sotak, "Time-dependent diffusion of water in a biological model system," Proceedings of the National Academy of Sciences of the United States of America **91**, 1229–1233 (1994).

[103] Alexander L Sukstanskii, "Exact analytical results for ADC with oscillating diffusion sensitizing gradients," Journal of Magnetic Resonance **234**, 135–140 (2013).

[104] Antonios Papaioannou, Dmitry S. Novikov, Els Fieremans, and Gregory S. Boutis, "Diffusion distinguishes between structural universality classes of disordered media," preprint arXiv:1607.08639 **https://arxiv.org/abs/1607.08639** (2016).

[105] Gregory Lemberskiy, Steven H. Baete, Martijn A. Cloos, Dmitry S. Novikov, and Els Fieremans, "Validation of surface-to-volume ratio derived from oscillating gradient spin echo on a clinical scanner using anisotropic fiber phantoms," Proceedings of the International Society of Magnetic Resonance in Medicine 24, p. 0013 (2016).

[106] Olivier Reynaud, Kerryanne Veronica Winters, Dung Minh Hoang, Youssef Zaim Wadghiri, Dmitry S Novikov, and Sungheon Gene Kim, "Surface-to-volume ratio mapping of tumor microstructure using oscillating gradient diffusion weighted imaging," Magn Reson Med **76**, 237–47 (2016).

[107] Olivier Reynaud, Kerryanne Veronica Winters, Dung Minh Hoang, Youssef Zaim Wadghiri, Dmitry S. Novikov, and Sungheon Gene Kim, "Pulsed and oscillating gradient MRI for assessment of cell size and extracellular space (POMACE) in mouse gliomas," NMR in Biomedicine (2016), 10.1002/nbm.3577.

[108] M H Ernst, J Machta, J R Dorfman, and H van Beijeren, "Long-time tails in stationary random media. 1. Theory," Journal of Statistical Physics **34**, 477–495 (1984).

[109] P B Visscher, "Universality in disordered diffusive systems - exact fixed-points in 1,2, and 3 dimensions," Physical Review B **29**, 5472–5485 (1984).

[110] Gordon M. G. Shepherd, Morten Raastad, and Per Andersen, "General and variable features of varicosity spacing along unmyelinated axons in the hippocampus and cerebellum," Proceedings of the National Academy of Sciences **99**, 6340–6345 (2002), http://www.pnas.org/content/99/9/6340.full.pdf.

[111] Gordon M. G. Shepherd and Morten Raastad, "Axonal varicosity distributions along parallel fibers: a new angle on a cerebellar circuit," The Cerebellum **2**, 110–113 (2003).

[112] Dominique Debanne, Emilie Campanac, Andrzej Bialowas, Edmond Carlier, and Gisèle Alcaraz, "Axon physiology," Physiological Reviews **91**, 555–602 (2011), http://physrev.physiology.org/content/91/2/555.full.pdf.

[113] Shengxiang Zhang, Jamie Boyd, Kerry Delaney, and Timothy H Murphy, "Rapid reversible changes in dendritic spine structure in vivo gated by the degree of ischemia," J Neurosci **25**, 5333–8 (2005).

[114] Ping Li and Timothy H Murphy, "Two-photon imaging during prolonged middle cerebral artery occlusion in mice reveals recovery of dendritic structure after reperfusion," J Neurosci **28**, 11970–9 (2008).

[115] Markus Nilsson, Jimmy Lätt, Freddy Stahlberg, Danielle van Westen, and Hakan Hagslätt, "The importance of axonal undulation in diffusion MR measurements: a monte carlo simulation study," NMR in Biomedicine **25**, 795–805 (2012).

[116] Aaron J Schain, Robert A Hill, and Jaime Grutzendler, "Label-free in vivo imaging of myelinated axons in health and disease with spectral confocal reflectance microscopy," Nat Med **20**, 443–449 (2014).

[117] Susie Y Huang, Aapo Nummenmaa, Thomas Witzel, Tanguy Duval, Julien Cohen-Adad, Lawrence L Wald, and Jennifer A McNab, "The impact of gradient strength on in vivo diffusion mri estimates of axon diameter," Neuroimage **106**, 464–72 (2015).

[118] Assaf Horowitz, Daniel Barazany, Ido Tavor, Moran Bernstein, Galit Yovel, and Yaniv Assaf, "In vivo correlation between axon diameter and conduction velocity in the human brain," Brain Structure and Function **220**, 1777–1788 (2015).

[119] GM Innocenti, R Caminiti, and F Aboitiz, "Comments on the paper by Horowitz et al.(2014)," Brain structure and function **220**, 1789–1790 (2015).

[120] C. Beaulieu, "The basis of anisotropic water diffusion in the nervous system - a technical review," NMR in Biomedicine **15**, 435–455 (2002).

[121] Jelle Veraart, Els Fieremans, and Dmitry S. Novikov, "Universal power-law scaling of water diffusion in human brain defines what we see with MRI," preprint arXiv:1609.09145 **https://arxiv.org/abs/1609.09145** (2016).

[122] Masaya Takahashi, David B. Hackney, Guixin Zhang, Suzanne L. Wehrli, Alex C. Wright, William T. O'Brien, Hidemasa Uematsu, Felix W. Wehrli, and Michael E. Selzer, "Magnetic resonance microimaging of intraaxonal water diffusion in live excised lamprey spinal cord," Proceedings of the National Academy of Sciences of the United States of America **99**, 16192–16196 (2002).

[123] Farshid Sepehrband, Daniel C Alexander, Nyoman D Kurniawan, David C Reutens, and Zhengyi Yang, "Towards higher sensitivity and stability of axon diameter estimation with diffusion-weighted mri," NMR Biomed **29**, 293–308 (2016).

[124] Keh-Jim Dunn and David J. Bergman, "Self diffusion of nuclear spins in a porous medium with a periodic microstructure," The Journal of Chemical Physics **102**, 3041–3054 (1995).

[125] Denis S. Grebenkov, "Nmr survey of reflected brownian motion," Rev. Mod. Phys. **79**, 1077–1137 (2007).

[126] Janez Stepisnik, Samo Lasic, Ales Mohoric, Igor Sersa, and Ana Sepe, "Velocity autocorrelation spectra of fluid in porous media measured by the cpmg sequence and constant magnetic field gradient," Magnetic Resonance Imaging **25**, 517–520 (2007).

[127] S. Portnoy, J.J. Flint, S.J. Blackband, and G.J. Stanisz, "Oscillating and pulsed gradient diffusion magnetic resonance microscopy over an extended b-value range: Implications for the characterization of tissue microstructure," Magnetic Resonance in Medicine **69**, 1131–1145 (2013).

[128] Ivana Drobnjak, Bernard Siow, and Daniel C Alexander, "Optimizing gradient waveforms for microstructure sensitivity in diffusion-weighted mr," Journal of Magnetic Resonance **206**, 41–51 (2010).

[129] I.M. Lifshitz, "Energy spectrum of disordered systems," Advances In Physics **13**, 483–536 (1964).

[130] Nevill F Mott and Edward A Davies, *Electronic processes in non-crystalline materials* (Oxford University Press, New York, 1971).

[131] Jelle Veraart, Els Fieremans, and Dmitry S Novikov, "Diffusion MRI noise mapping using random matrix theory," Magnetic resonance in medicine **DOI: 10.1002/mrm.26059** (2016).

[132] Jelle Veraart, Dmitry S Novikov, Daan Christiaens, Benjamin Ades-aron, Jan Sijbers, and Els Fieremans, "Denoising

of diffusion MRI using random matrix theory," NeuroImage **http://dx.doi.org/10.1016/j.neuroimage.2016.08.016** (2016).

[133] Emmanuel J. Candes, Justin K. Romberg, and Terence Tao, "Stable signal recovery from incomplete and inaccurate measurements," Communications on Pure and Applied Mathematics **59**, 1207–1223 (2006).

[134] Michael Lustig, David Donoho, and John M. Pauly, "Sparse mri: The application of compressed sensing for rapid mr imaging," Magnetic Resonance in Medicine **58**, 1182–1195 (2007).

[135] Dan Ma, Vikas Gulani, Nicole Seiberlich, Kecheng Liu, Jeffrey L. Sunshine, Jeffrey L. Duerk, and Mark A. Griswold, "Magnetic resonance fingerprinting," Nature **495**, 187–192 (2013).

[136] Milos D Ikonomovic, Eric E Abrahamson, Barbara A Isanski, Joanne Wuu, Elliott J Mufson, and Steven T DeKosky, "Superior frontal cortex cholinergic axon density in mild cognitive impairment and early alzheimer disease," Arch Neurol **64**, 1312–7 (2007).

[137] Björn Lampinen, Filip Szczepankiewicz, Danielle van Westen, Elisabet Englund, Pia C Sundgren, Jimmy Lätt, Freddy Strahlberg, and Markus Nilsson, "Optimal experimental design for filter exchange imaging: Apparent exchange rate measurements in the healthy brain and in intracranial tumors," Magn Reson Med (2016), 10.1002/mrm.26195.

[138] Jens H Jensen, G Russell Glenn, and Joseph A Helpern, "Fiber ball imaging," NeuroImage **124**, 824–833 (2016).

[139] Joseph J H Ackerman and Jeffrey J Neil, "The use of mr-detectable reporter molecules and ions to evaluate diffusion in normal and ischemic brain," NMR Biomed **23**, 725–33 (2010).

[140] Itamar Ronen, Matthew Budde, Ece Ercan, Jacopo Annese, Aranee Techawiboonwong, and Andrew Webb, "Microstructural organization of axons in the human corpus callosum quantified by diffusion-weighted magnetic resonance spectroscopy of n-acetylaspartate and post-mortem histology," Brain Struct Funct **219**, 1773–85 (2014).

[141] Matthew D. Budde and Joseph A. Frank, "Examining brain microstructure using structure tensor analysis of histological sections," NeuroImage **63**, 1 – 10 (2012).

[142] Bibek Dhital, Elias Kellner, Marco Reisert, and Valerij G Kiselev, "Isotropic diffusion weighting provides insight on diffusion compartments in human brain white matter in vivo," Proceedings of the International Society of Magnetic Resonance in Medicine 23, p. 2788. (2015).

[143] Eleftheria Panagiotaki, Torben Schneider, Bernard Siow, Matt G Hall, Mark F Lythgoe, and Daniel C Alexander, "Compartment models of the diffusion mr signal in brain white matter: a taxonomy and comparison," Neuroimage **59**, 2241–54 (2012).

[144] Uran Ferizi, Torben Schneider, Thomas Witzel, Lawrence L Wald, Hui Zhang, Claudia A M Wheeler-Kingshott, and Daniel C Alexander, "White matter compartment models for in vivo diffusion mri at 300mt/m," Neuroimage **118**, 468–83 (2015).

[145] Sune Nørhøj Jespersen, "Equivalence of double and single wave vector diffusion contrast at low diffusion weighting," NMR Biomed **25**, 813–8 (2012).

[146] J-Donald Tournier, Fernando Calamante, and Alan Connelly, "Robust determination of the fibre orientation distribution in diffusion MRI: non-negativity constrained super-resolved spherical deconvolution," Neuroimage **35**, 1459–72 (2007).

[147] Els Fieremans, Jens H. Jensen, Joseph A. Helpern, Sungheon Kim, Robert I. Grossman, Matilde Inglese, and Dmitry S. Novikov, "Diffusion distinguishes between axonal loss and demyelination in brain white matter," Proceedings of the International Society of Magnetic Resonance in Medicine 20, p.714 (2012).

[148] Dmitry S. Novikov and Els Fieremans, "Relating extracellular diffusivity to cell size distribution and packing density as applied to white matter," Proceedings of the International Society of Magnetic Resonance in Medicine 20, p.1829 (2012).

[149] Ileana O Jelescu, Magdalena Zurek, Kerryanne V Winters, Jelle Veraart, Anjali Rajaratnam, Nathanael S Kim, James S Babb, Timothy M Shepherd, Dmitry S Novikov, Sungheon G Kim, and Els Fieremans, "In vivo quantification of demyelination and recovery using compartment-specific diffusion mri metrics validated by electron microscopy," Neuroimage **132**, 104–14 (2016).

[150] Ahmad Raza Khan, Andrey Chuhutin, Ove Wiborg, Christopher D. Kroenke, Jens R. Nyengaard, Brian Hansen, and Sune Nørhøj Jespersen, "Biophysical modeling of high field diffusion mri demonstrates micro-structural aberration in chronic mild stress rat brain," NeuroImage (2016), 10.1016/j.neuroimage.2016.07.001.

[151] Ahmad Raza Khan, Andrey Chuhutin, Ove Wiborg, Christopher D. Kroenke, Jens R. Nyengaard, Brian Hansen, and Sune Nørhøj Jespersen, "Summary of high field diffusion mri and microscopy data demonstrate microstructural aberration in chronic mild stress rat brain," Data in brief **8**, 934 (2016).

[152] Peter Vestergaard-Poulsen, Gregers Wegener, Brian Hansen, Carsten R. Bjarkam, Stephen J. Blackband, Niels Christian Nielsen, and Sune N. Jespersen, "Diffusion-weighted mri and quantitative biophysical modeling of hippocampal neurite loss in chronic stress," P L o S One **6**, e20653 (2011).

[153] Matthew D. Budde and Joseph A. Frank, "Neurite beading is sufficient to decrease the apparent diffusion coefficient after ischemic stroke," Proceedings of the National Academy of Sciences of the United States of America **107**, 14472–14477 (2010).

[154] Nikola Stikov, Jennifer S W Campbell, Thomas Stroh, Mariette Lavelée, Stephen Frey, Jennifer Novek, Stephen Nuara, Ming-Kai Ho, Barry J Bedell, Robert F Dougherty, Ilana R Leppert, Mathieu Boudreau, Sridar Narayanan, Tanguy Duval, Julien Cohen-Adad, Paul-Alexandre Picard, Alicja Gasecka, Daniel Côté, and G Bruce Pike, "In vivo histology of the myelin g-ratio with magnetic resonance imaging," Neuroimage **118**, 397–405 (2015).

[155] B. Hansen, A. R. Khan, N. Shemesh, T. E. Lund, R. Sangill, L. Ostergaard, and S. N. Jespersen, "White matter biomarkers from fast protocols using axially symmetric diffusion kurtosis imaging," preprint arXiv:1610.02783 **https://arxiv.org/abs/1610.02783** (2016).

[156] Brian Hansen, Noam Shemesh, and Sune Nørhøj Jespersen, "Fast imaging of mean, axial and radial diffusion kurtosis," NeuroImage **http://dx.doi.org/10.1016/j.neuroimage.2016.08.022** (2016).

[157] Valerij G Kiselev and Kamil A Il'yasov, "Is the "biexponential diffusion" biexponential?" Magn Reson Med **57**, 464–9 (2007).

[158] Ileana O. Jelescu, Jelle Veraart, Vitria Adisetiyo, Sarah S. Milla, Dmitry S. Novikov, and Els Fieremans, "One diffusion acquisition and different white matter models: How does microstructure change in human early development based on {WMTI} and noddi?" NeuroImage **107**, 242 – 256 (2015).

[159] Edward S Hui, Els Fieremans, Jens H Jensen, Ali Tabesh,

Wuwei Feng, Leonardo Bonilha, Maria V Spampinato, Robert Adams, and Joseph A Helpern, "Stroke assessment with diffusional kurtosis imaging," Stroke **43**, 2968–73 (2012).

[160] Nathaniel D. Kelm, Kathryn L. West, Robert P. Carson, Daniel F. Gochberg, Kevin C. Ess, and Mark D. Does, "Evaluation of diffusion kurtosis imaging in ex vivo hypomyelinated mouse brains," NeuroImage **124, Part A**, 612 – 626 (2016).

[161] Maria F. Falangola, David N. Guilfoyle, Ali Tabesh, Edward S. Hui, Xingju Nie, Jens H. Jensen, Scott V. Gerum, Caixia Hu, John LaFrancois, Heather R. Collins, and Joseph A. Helpern, "Histological correlation of diffusional kurtosis and white matter modeling metrics in cuprizone-induced corpus callosum demyelination," NMR in Biomedicine **27**, 948–957 (2014), nBM-13-0171.R2.

[162] C. Guglielmetti, J. Veraart, E. Roelant, Z. Mai, J. Daans, J. Van Audekerke, M. Naeyaert, G. Vanhoutte, R. Delgado y Palacios, J. Praet, E. Fieremans, P. Ponsaerts, J. Sijbers, A. Van der Linden, and M. Verhoye, "Diffusion kurtosis imaging probes cortical alterations and white matter pathology following cuprizone induced demyelination and spontaneous remyelination," NeuroImage **125**, 363 – 377 (2016).

[163] Elan J. Grossman, Ivan I. Kirov, Oded Gonen, Dmitry S. Novikov, Matthew S. Davitz, Yvonne W. Lui, Robert I. Grossman, Matilde Inglese, and Els Fieremans, "N-acetyl-aspartate levels correlate with intra-axonal compartment parameters from diffusion {MRI}," NeuroImage **118**, 334 – 343 (2015).

[164] Maira Tariq, Torben Schneider, Daniel C Alexander, Claudia A Gandini Wheeler-Kingshott, and Hui Zhang, "Bingham–noddi: Mapping anisotropic orientation dispersion of neurites using diffusion mri," NeuroImage (2016).

[165] A Szafer, J Zhong, and J C Gore, "Theoretical model for water diffusion in tissues," Magn Reson Med **33**, 697–712 (1995).

[166] Maria Tariq, Michiel Kleinnijenhuis, Anne-Marie van Cappellen van Walsum, and Hui Zhang, "Validation of noddi estimation of dispersion anisotropy in v1 of the human neocortex," Proceedings of the International Society of Magnetic Resonance in Medicine 23, p. 0477 (2015).

[167] Michael Kazhdan, Thomas Funkhouser, and Szymon Rusinkiewicz, "Rotation invariant spherical harmonic representation of 3 d shape descriptors," in *Symposium on geometry processing*, Vol. 6 (2003) pp. 156–164.

[168] Sune Nørhøj Jespersen, Henrik Lundell, Casper Kaae Sønderby, and Tim B Dyrby, "Orientationally invariant metrics of apparent compartment eccentricity from double pulsed field gradient diffusion experiments," NMR Biomed **26**, 1647–62 (2013).

[169] Samo Lasi**v**c, Filip Szczepankiewicz, Stefanie Eriksson, Markus Nilsson, and Daniel Topgaard, "Microanisotropy imaging: quantification of microscopic diffusion anisotropy and orientational order parameter by diffusion mri with magic-angle spinning of the q-vector," Frontiers in Physics **2**, 11 (2014).

[170] Enrico Kaden, Frithjof Kruggel, and Daniel C Alexander, "Quantitative mapping of the per-axon diffusion coefficients in brain white matter," Magnetic resonance in medicine (2015).

[171] Enrico Kaden, Nathaniel D. Kelm, Robert P. Carson, Mark D. Does, and Daniel C. Alexander, "Multi-compartment microscopic diffusion imaging," NeuroImage **139**, 346 – 359 (2016).

[172] Filip Szczepankiewicz, Danielle van Westen, Elisabet Englund, Carl-Fredrik Westin, Freddy St**r**ahlberg, Jimmy Lätt, Pia C. Sundgren, and Markus Nilsson, "The link between diffusion {MRI} and tumor heterogeneity: Mapping cell eccentricity and density by diffusional variance decomposition (divide)," NeuroImage , – (2016).

[173] A Bohr and Ben R Mottelson, *Nuclear Structure, Vol. II: Nuclear Deformations* (World Scientific, 1998).

[174] Filip Szczepankiewicz, Samo Lasi**v**c, Danielle van Westen, Pia C Sundgren, Elisabet Englund, Carl-Fredrik Westin, Freddy St**r**ahlberg, Jimmy Lätt, Daniel Topgaard, and Markus Nilsson, "Quantification of microscopic diffusion anisotropy disentangles effects of orientation dispersion from microstructure: applications in healthy volunteers and in brain tumors," NeuroImage **104**, 241–252 (2015).

[175] Nathan P. Skinner, Shekar N. Kurpad, Brian D. Schmit, L. Tugan Muftuler, and Matthew D. Budde, "Rapid in vivo detection of rat spinal cord injury with double-diffusion-encoded magnetic resonance spectroscopy," Magnetic Resonance in Medicine **DOI:10.1002/mrm.26243**, n/a–n/a (2016).

[176] Dmitriy A. Yablonskiy and Alexander L. Sukstanskii, "Theoretical models of the diffusion weighted mr signal," NMR in Biomedicine **23**, 661–681 (2010).

[177] Y. Cheng and D. G. Cory, "Multiple scattering by nmr," J. Am. Chem. Soc. **121**, 7935–7936 (1999).

[178] D. G. Cory, A. N. Garroway, and J. B. Miller, "Applications of spin transport as a probe of local geometry," Polym. Prep. Am. Chem. Soc. Div. Polym. Chem. **31**, 149 (1990).

[179] P. P. Mitra, L. L. Latour, R. L. Kleinberg, and C. H. Sotak, "Pulsed-field-gradient nmr measurements of restricted diffusion and the return-to-the-origin probability," J. Magn. Reson. Series A **114**, 47–58 (1995).

[180] N. Shemesh, S. N. Jespersen, D. C. Alexander, Y. Cohen, I. Drobnjak, T. B. Dyrby, J. Finsterbusch, M. A. Koch, T. Kuder, F. Laun, M. Lawrenz, H. Lundell, P. P. Mitra, M. Nilsson, E. Ozarslan, D. Topgaard, and C. F. Westin, "Conventions and nomenclature for double diffusion encoding nmr and mri," Magn Reson Med **75**, 82–7 (2016).

[181] Sune Nørhøj Jespersen, "Equivalence of double and single wave vector diffusion contrast at low diffusion weighting," NMR Biomed **25**, 813–8 (2012).

[182] J. Finsterbusch, "Extension of the double-wave-vector diffusion-weighting experiment to multiple concatenations," J. Magn. Reson. **198**, 174–182 (2009).

[183] J. Finsterbusch, "Numerical simulations of short-mixing-time double-wave-vector diffusion-weighting experiments with multiple concatenations on whole-body mr systems," Journal of Magnetic Resonance **207**, 274–282 (2010).

[184] S. N. Jespersen and N. Buhl, "The displacement correlation tensor from double wave vector diffusion experiments encodes information about pore microstructure and ensemble properties," in *Proc. Int. Soc. Magn. Reson. Med.*, Vol. 19.

[185] M. A. Koch and J. Finsterbusch, "Numerical simulation of double-wave vector experiments investigating diffusion in randomly oriented ellipsoidal pores," Magn. Reson. Med. **62**, 247–254 (2009).

[186] E. Ozarslan and P. J. Basser, "Microscopic anisotropy revealed by nmr double pulsed field gradient experiments with arbitrary timing parameters," J Chem Phys **128**, 154511 (2008).

[187] E. Ozarslan, N. Shemesh, and P. J. Basser, "A general framework to quantify the effect of restricted diffusion on the nmr signal with applications to double pulsed field gradient nmr experiments," J Chem Phys **130**, 104702 (2009).

[188] N. Shemesh, E. Ozarslan, P.J. Basser, and Y. Cohen, "Mea-

suring small compartmental dimensions with low-q angular double-pgse nmr: The effect of experimental parameters on signal decay," Journal of Magnetic Resonance **198**, 15–23 (2009).

[189] M. A. Koch and J. Finsterbusch, "Compartment size estimation with double wave vector diffusion-weighted imaging," Magn. Reson. Med. **60**, 90–101 (2008).

[190] M. E. Komlosh, E. zarslan, M. J. Lizak, F. Horkay, V. Schram, N. Shemesh, Y. Cohen, and P. J. Basser, "Pore diameter mapping using double pulsed-field gradient mri and its validation using a novel glass capillary array phantom," J Magn Reson **208**, 128–35 (2011).

[191] E. Ozarslan, M. E. Komlosh, M. J. Lizak, F. Horkay, and P. J. Basser, "Double pulsed field gradient (double-pfg) mr imaging (mri) as a means to measure the size of plant cells," Magn Reson Chem **49 Suppl 1**, S79–84 (2011).

[192] N. Shemesh, E. Ozarslan, P. J. Basser, and Y. Cohen, "Accurate noninvasive measurement of cell size and compartment shape anisotropy in yeast cells using double-pulsed field gradient mr," NMR Biomed **25**, 236–46 (2012).

[193] N. Shemesh, E. zarslan, A. Bar-Shir, P. J. Basser, and Y. Cohen, "Observation of restricted diffusion in the presence of a free diffusion compartment: single- and double-pfg experiments," J. Magn. Reson. **200**, 214–225 (2009).

[194] N. Shemesh, E. zarslan, P. J. Basser, and Y. Cohen, "Measuring small compartmental dimensions with low-q angular double-pgse nmr: The effect of experimental parameters on signal decay," J. Magn. Reson. **198**, 15–23 (2009).

[195] T. Weber, C. H. Ziener, T. Kampf, V. Herold, W. R. Bauer, and P. M. Jakob, "Measurement of apparent cell radii using a multiple wave vector diffusion experiment," Magn. Reson. Med. **61**, 1001–1006 (2009).

[196] A. V. Avram, E. Ozarslan, J. E. Sarlls, and P. J. Basser, "In vivo detection of microscopic anisotropy using quadruple pulsed-field gradient (qpfg) diffusion mri on a clinical scanner," Neuroimage **64**, 229–39 (2013).

[197] M. A. Koch and J. Finsterbusch, "Towards compartment size estimation in vivo based on double wave vector diffusion weighting," NMR Biomed **24**, 1422–32 (2011).

[198] M. Lawrenz and J. Finsterbusch, "Double-wave-vector diffusion-weighted imaging reveals microscopic diffusion anisotropy in the living human brain," Magn Reson Med **69**, 1072–82 (2013).

[199] M. Lawrenz and J. Finsterbusch, "Mapping measures of microscopic diffusion anisotropy in human brain white matter in vivo with double-wave-vector diffusion-weighted imaging," Magn Reson Med **73**, 773–83 (2015).

[200] S. N. Jespersen, "Comment on "measuring small compartments with relatively weak gradients by angular double-pulsed-field-gradient nmr" by morozov bar, sochen, and cohen," Magn Reson Imaging **31**, 1643–4 (2013).

[201] J. H. Jensen, "Sufficiency of diffusion tensor in characterizing the diffusion mri signal to leading order in diffusion weighting," NMR Biomed **27**, 1005–7 (2014).

[202] F. Frøhlich, A., L. Ostergaard, and G. Kiselev, V., "Effect of impermeable interfaces on apparent diffusion coefficient in heterogeneous media," App. Magn. Reson. **29**, 123–137 (2005).

[203] Astrid F. Frøhlich, Sune N. Jespersen, Leif Ostergaard, and Valerij G. Kiselev, "The effect of impermeable boundaries of arbitrary geometry on the apparent diffusion coefficient," Journal of Magnetic Resonance **194**, 128–135 (2008).

[204] N. Shemesh, E. Ozarslan, T. Adiri, P. J. Basser, and Y. Cohen, "Noninvasive bipolar double-pulsed-field-gradient nmr reveals signatures for pore size and shape in polydisperse, randomly oriented, inhomogeneous porous media," J Chem Phys **133**, 044705 (2010).

[205] Noam Shemesh, Tal Adiri, and Yoram Cohen, "Probing microscopic architecture of opaque heterogeneous systems using double-pulsed-field-gradient nmr," Journal of the American Chemical Society **133**, 6028–6035 (2011).

[206] S. N. Jespersen, H. Lundell, C. K. Sonderby, and T. B. Dyrby, "Orientationally invariant metrics of apparent compartment eccentricity from double pulsed field gradient diffusion experiments," NMR Biomed **26**, 1647–62 (2013).

[207] Noam Shemesh and Yoram Cohen, "Microscopic and compartment shape anisotropies in gray and white matter revealed by angular bipolar double-pfg mr," Magnetic resonance in medicine **65**, 1216–1227 (2011).

[208] N. Shemesh, D. Barazany, O. Sadan, L. Bar, Y. Zur, Y. Barhum, N. Sochen, D. Offen, Y. Assaf, and Y. Cohen, "Mapping apparent eccentricity and residual ensemble anisotropy in the gray matter using angular double-pulsed-field-gradient mri," Magn Reson Med **68**, 794–806 (2012).

[209] P. P. Mitra, "Multiple wave-vector extensions of the nmr pulsed-field-gradient spin-echo diffusion measurement," Phys. Rev. B **51**, 15074–15078 (1995).

[210] M. Lawrenz, M. A. Koch, and J. Finsterbusch, "A tensor model and measures of microscopic anisotropy for double-wave-vector diffusion-weighting experiments with long mixing times," J Magn Reson **202**, 43–56 (2010).

[211] H. Lundell, T. B. Dyrby, P. L. Hubbard, Feng-Lei Zhou, G. J. Parker, and S.N. Jespersen, "Validation of double diffusion schemes of microscopic fractional anisotropy," in *Proc. Int. Soc. Magn. Reson. Med.*, Vol. 23, p. 155.

[212] E. zarslan, "Compartment shape anisotropy (csa) revealed by double pulsed field gradient mr," J. Magn. Reson. **199**, 56–67 (2009).

[213] Sune Nrhj Jespersen, Henrik Lundell, Casper Kaae Snderby, and Tim B. Dyrby, "Commentary on microanisotropy imaging: quantification of microscopic diffusion anisotropy and orientation of order parameter by diffusion mri with magic-angle spinning of the q-vector," Frontiers in Physics **2** (2014), 10.3389/fphy.2014.00028.

[214] S. Lasic, F. Szczepankiewicz, S. Eriksson, M. Nilsson, and D. Topgaard, "Microanisotropy imaging: quantification of microscopic diffusion anisotropy and orientational order parameter by diffusion mri with magic-angle spinning of the q-vector," Frontiers in Physics (2014).

[215] S. N. Jespersen, L. A. Leigland, A. Cornea, and C. D. Kroenke, "Determination of axonal and dendritic orientation distributions within the developing cerebral cortex by diffusion tensor imaging," Ieee Transactions on Medical Imaging **31**, 16–32 (2012).

[216] Eric Betzig, "Nobel lecture: Single molecules, cells, and super-resolution optics," Reviews of Modern Physics **87**, 1153 (2015).